

Investigating the Spectroscopic Binary Population of Omega Centauri with MUSE

by

Florence Wragg

A thesis submitted in partial fulfillment for the
degree of Doctor of Philosophy

November 2024

Declaration

The work presented in this thesis was carried out at the Astrophysics Research Institute, Liverpool John Moores University. Unless otherwise stated, it is the original work of the author.

While registered as a candidate for the degree of Doctor of Philosophy, for which submission is now made, the author has not been registered as a candidate for any other award. This thesis has not been submitted in whole, or in part, for any other degree.

Florence Wragg
Astrophysics Research Institute
Liverpool John Moores University
IC2, Liverpool Science Park
146 Brownlow Hill
Liverpool
L3 5RF
UK

NOVEMBER 2024

Abstract

Globular clusters are a crucial component of their host galaxies. They are ubiquitous in both distant and local galaxies, including our own Milky Way. Despite their importance, however, some fundamental questions about globular cluster formation and evolution are still unanswered: how many black holes are retained in clusters, and could more massive clusters host an illusive intermediate mass black hole (IMBH)? How do multiple populations form, creating populations of stars each with distinct chemistry? Can any links be made between young and ancient star clusters? And can galactic archaeology identify the population of accreted globular clusters, including bright, massive nuclear star clusters (NSCs) that form in the centres of their host galaxies, and track the merger history of the galaxy? A key topic to understanding globular clusters is binary stars. Binary systems are present at the birth of the cluster and act to delay the later stages of cluster evolution. They can also provide insights on the properties of the cluster, namely the number and masses of black holes within the cluster centre, and the formation conditions and evolution of multiple populations. And yet, for many of the most complex and unusual clusters in the Milky Way, the binary fraction, and the demographics of binary stars, are still unknown.

NGC 5139 (ω Cen), is the closest candidate of a NSC that has been stripped of its host galaxy in the Milky Way. Despite extensive studies through the last decades, many open questions about the cluster remain, including the properties of the binary population. In this study we use multi-epoch spectroscopy from the Multi Unit Spectroscopic Explorer (MUSE) to identify binary systems in ω Cen. The observations span 8 years, with a total of 312 248 radial velocity measurements for 37 225 stars.

Following the removal of known photometric variables, and using dedicated simulations, we identify 275 stars that show radial velocity variations, corresponding to a discovery

fraction of $1.4 \pm 0.1\%$, and show that our data is sensitive to $70 \pm 10\%$ of the binaries expected in the sample. By combining these results, we calculate a completeness-corrected binary fraction of $2.1 \pm 0.4\%$ in the central region of ω Cen. We find similar binary fractions for all stellar evolutionary stages covered by our data, the only notable exception being the blue straggler stars, which show an enhanced binary fraction. We also find no distinct correlation with distance from the cluster centre, indicating a limited amount of mass segregation within the half-light radius of ω Cen.

By using a combination of spectroscopy and photometry, we then investigate the binary fraction across the various stellar populations of ω Cen. By separating our sample into populations grouped by metallicity and light element abundance respectively, we separate the red giant branch of ω Cen into 9 chemically distinct populations. Overall, we find no statistically significant trend in binary fraction across the different populations. This result may be due to the effect of cluster relaxation, which will erase the distributions of populations over time.

Acknowledgements

The first person that I would like to thank is my supervisor, Sebastian Kamann. I appreciate that I can't have been an easy PhD student at times, but it has been a privilege to work with you, and I know that this wouldn't have been possible without your seemingly limitless expertise, patience, kindness and encouragement. I hope I haven't put you off supervising PhD students! I would also like to thank my supervisory team, Marie Martig and Nate Bastian. Your guidance and support over the years have been invaluable both from a science standpoint and also guiding me through expectations and admin of academia. I'd also like to thank Sara Saracino for always having the time to chat to me and answer any of the random questions that popped into my head. The ideas and conversations that I have been able to engage with from the remaining members of the globular cluster research group, Elena Balakina and Renuka Pechetti, and the Local Group group have also been a pleasure.

I would also like to express how lucky and grateful I am to have been able to meet the other incredible students at the ARI. Jemima, you have done amazingly at not only being able to cope with my nonsense in the office, but also at home. You've become the sister I never had, one of my dearest friends, my grammar checker, my rubber duck, and my stylist all in one and I don't think I could've done this without you. I have always said that one of the best parts about my PhD has been the privilege of getting to know all of the wonderful people in office 3.18 (both past and present): Jemima (again!), Andrew, Tutku, Phoebe, Ryan, Elena, Sarah, Bethan, Kyle and Adrian. You guys have been the greatest friends, the best cheer squad and occasionally a delft crisis management team. Em, you can be an honorary member of 3.18 as well, as we all manage to share the same brain. You're all truly extraordinary people and I can safely say that I'm a better person for having met you all. There are so many more wonderful people I have been

fortunate enough to meet along the way who haven't gotten a mention, but otherwise these acknowledgements would be almost as long as my thesis.

I think, most importantly, I would like to thank my family for their love and support. To my mum, Kate, and brother, Matthew, you've put up with the ups and downs of my time in academia for 21 years now and you've both always celebrated me at my highest and been there for me at my lowest. To Matt, my love, thank you so much for all the unconditional love you have given me through the years. You've been my best friend, my biggest advocate and my therapist rolled into one and I just think you're amazing. I'd also like to thank all the friends that have been with me throughout my undergraduate and PhD, Emma, Sam and Niam to name just a few. I also can't forget to thank and Mouse and Bean for taking the essential role of emotional support cats.

The final acknowledgement I would like to make is to my father, David Wragg. My dad was diagnosed with terminal cancer in 2020 and passed away in early 2021. One of his biggest wishes was for me and my brother to continue to follow our passions and complete our studies, and the thought of both of his children studying for PhDs filled him with great pride. My father was the smartest man I ever met, and always seemed to have something to add, or some new perspective on any topic that was being discussed. I still have vivid memories of my dad holding my hand while taking me to primary school, where I would first fall in love with science. While he won't be able to see me graduate, I hope that somehow he's watching over me and is proud of everything I have been able to achieve.

Declaration of Authorship

I, Florence Wragg, declare that this thesis titled, ‘Investigating the Spectroscopic Binary Population of Omega Centauri with MUSE’ and the work presented in it are my own. I confirm that:

- This work was done wholly or mainly while in candidature for a research degree at this University.
- Where any part of this thesis has previously been submitted for a degree or any other qualification at this University or any other institution, this has been clearly stated.
- Where I have consulted the published work of others, this is always clearly attributed.
- Where I have quoted from the work of others, the source is always given. With the exception of such quotations, this thesis is entirely my own work.
- I have acknowledged all main sources of help.
- Where the thesis is based on work done by myself jointly with others, I have made clear exactly what was done by others and what I have contributed myself.

Signed: Florence Wragg

Date: 17th November 2024

“Seize the time... Live now! Make now always the most precious time. Now will never come again”

Captain Jean-Luc Picard - *Star Trek: The Next Generation*

Contents

Declaration	ii
Abstract	iii
Acknowledgements	v
Declaration of Authorship	vii
List of Figures	xii
List of Tables	xiv
Abbreviations	xv
Physical Constants	xvii
1 Introduction	1
1.1 Globular clusters	2
1.1.1 Cluster formation	3
1.1.1.1 Formation of massive star clusters	3
1.1.1.2 Formation of globular cluster populations	4
1.1.1.3 Globular cluster population in the Milky Way	5
1.1.1.4 Links to young star clusters	5
1.1.2 Cluster evolution	6
1.1.3 Black holes	10
1.1.3.1 Black hole classification	11
1.1.3.2 Black holes in globular clusters	13
1.1.4 Binary stars	15
1.1.4.1 Blue straggler stars	20
1.1.4.2 Other exotic objects	21
1.1.5 Multiple populations	23
1.1.5.1 Multiple populations in binaries	28
1.2 Nuclear Star Clusters	29
1.3 Omega Centauri	31
1.4 Observational techniques	36
1.4.1 Photometry vs. spectroscopy	36

1.4.2	Using velocity variations to identify binary systems	39
1.5	MUSE	44
1.6	Aims of this work	46
2	Detecting Variability	48
2.1	MUSE data	49
2.1.1	Observations	49
2.1.2	Data reduction	49
2.2	Spectral analysis	50
2.2.1	Spectral extraction	50
2.2.2	Spectral analysis	51
2.2.3	Separating CMD regions	52
2.2.4	Final sample	53
2.3	Removing photometric variables	54
2.3.1	MUSE identified photometric variables	55
2.4	Calculating the probability of variability	56
2.5	Summary	58
3	Determining the Sample Completeness	60
3.1	Physical principles	61
3.1.1	Binary hardness	61
3.1.2	Roche lobe filling	62
3.2	Generating the mock sample	63
3.3	Binary recovery as a function of probability	65
3.4	Binary recovery as a function of orbital parameter	69
3.5	Summary	71
4	Calculating the Binary Fraction	74
4.1	Calculating the discovery fraction	75
4.2	Corrected binary fraction	76
4.2.1	Radial distribution of binaries	77
4.3	Summary	79
5	Characterising Identified Binaries	80
5.1	Binary stars across multiple populations	81
5.1.1	Binarity as a function of [Fe/H]	81
5.1.2	Binarity as a function of abundances	86
5.1.3	Separation into populations	90
5.2	Summary	93
6	Conclusions and Future Outlook	95
6.1	Conclusions	96
6.2	Future work	97
6.2.1	Studies of ω Cen	97
6.2.2	Applications to other clusters	98
6.2.3	Future observations	98

Bibliography

100

List of Figures

1.1	Comparison of the open cluster NGC 6475 (Messier 7) and the globular cluster NGC 104 (47 Tuc)	3
1.2	Globular clusters in the Milky Way colour coded to show the predicted origin based on previous galaxy mergers	6
1.3	A comparison of age and metallicity for Milky Way and LMC/SMC star clusters	7
1.4	The half mass relaxation time for globular clusters as a function of cluster mass	8
1.5	Distribution of stellar mass in NGC 6293	9
1.6	Examples of surface brightness as a function of cluster radius for core collapsed and non-core collapsed globular clusters	10
1.7	Detection of a stellar mass black hole in NGC 3201 with a minimum mass of $4.36 \pm 0.41 M_{\odot}$	14
1.8	Comparisons of surface density and velocity dispersion profiles to a range of IMBH mass models	16
1.9	The correlation between binary hardness and orbital period for a range of companion stellar masses	17
1.10	The radial distribution of binary stars in NGC 3201	19
1.11	Blue straggler stars in M30, with markers representing theorised the collisional and mass transfer formation scenarios	22
1.12	Spectroscopic analysis of the chemical abundances of multiple populations in NGC 6752	25
1.13	The chromosome map of NGC 6723 which shows the clusters distinct 1P and 2P populations	26
1.14	The CMD of the globular cluster NGC 2808 which shows a split main sequence caused by multiple populations	27
1.15	A comparison of chromosome maps between Type I and Type II clusters	27
1.16	A comparison of the brightness and spatial distributions of NSCs and typical globular clusters	29
1.17	The surface brightness profile of ω Cen	32
1.18	The stellar mass function of ω Cen at different projected distances	33
1.19	Comparison between observations of ω Cen and a variety of black hole models	34
1.20	The distribution of stellar velocities in ω Cen compared to IMBH models	35
1.21	The chromosome map of ω Cen	36
1.22	The multiple populations of ω Cen as separately identified branches of the main sequence	37
1.23	The binary main sequence of NGC 1718	38

1.24	The radial velocity curve fitted for a star in ω Cen	40
1.25	The effect of orbital period on the radial velocity curve of a star in a binary system	42
1.26	The effect of mass ratio on the radial velocity curve of a star in a binary system	42
1.27	The effect of eccentricity on the radial velocity curve of a star in a binary system	43
1.28	The effect of inclination angle on the radial velocity curve of a star in a binary system	44
2.1	A mosaic of ω Cen which shows the $1'$ pointings of MUSE WFM	50
2.2	Distribution of the number of epochs and the cumulative distribution of stars with at least a given number of epochs	55
2.3	Two CMDs of ω Cen, the left panel with identified and removed photometric variables and the right panel, which shows the distribution of probability variability	58
2.4	Distribution of probability variability within the MUSE sample	59
3.1	A flow chart highlighting the key steps in generating the mock data sample	66
3.2	The distribution of orbital parameters in the mock sample both before and after removing soft and interacting binaries	67
3.3	A comparison of the false positive and true positive detection rates for a variety of minimum epoch numbers and probability cut values	68
3.4	The mean probability of variability for binary systems as a function of orbital parameters	70
3.5	Recovery fraction of binaries in the mock data for different orbital parameters and different regions of the CMD	72
4.1	The binary fraction of ω Cen as a function of cluster radius	78
5.1	CMD of ω Cen highlighting metallicity distribution	82
5.2	Histogram showing global metallicity distribution	83
5.3	Normalised metallicity distribution with a fitted Gaussian for each of the sub populations	84
5.4	Global relation between binary fraction and metallicity	85
5.5	Binary fraction of each metallicity population	86
5.6	Chromosome map of ω Cen	87
5.7	Histogram showing the global distribution of ΔC	87
5.8	Normalised ΔC distribution with fitted Gaussians for each of the sub populations	89
5.9	Global relation between ΔC variation and binarity	90
5.10	Binary fraction for each ΔC population	91
5.11	Chromosome map of ω Cen showing the 9 detected populations in the cluster	92
5.12	Normalised and cumulative radial distribution of the separated populations for metallicity and ΔC variation	93

List of Tables

3.1	The completeness of the ω Cen sample across different regions of the CMD	71
4.1	The discovery fraction across the CMD of ω Cen	75
4.2	The binary fraction of ω Cen, along with the discovery fraction, completeness and the number of stars and binary systems in the sample both for the global population and different regions of the CMD	76
5.1	The binary fraction and number of stars for each of the three metallicity sub populations	85
5.2	The binary fraction and number of stars for each of the three considered ΔC sub populations	89
5.3	The binary fraction and number of stars for each of the 9 sub populations that have been defined for ω Cen through this study	92

Abbreviations

ω Cen	Omega Centauri
LMC	Large Magellanic Cloud
SMC	Small Magellanic Cloud
NSC	Nuclear Star Cluster
UCD	Ultra Compact Dwarf
BH	Black Hole
IMBH	Intermediate Mass Black Hole
SMBH	Super Massive Black Hole
CMD	Colour Magnitude Diagram
MS	Main Sequence
TO	Turn Off
SGB	Sub Giant Branch
RGB	Red Giant Branch
HB	Horizontal Branch
AGB	Asymptotic Giant Branch
BSS	Blue Straggler Star
SFH	Star Formation History
GMM	Gaussian Mixing Model
SNR	Signal to Noise Ratio
MUSE	Multi Unit Spectroscopic Explorer
BlueMUSE	Blue Multi Unit Spectroscopic Explorer
HARMONI	High Angular Resolution Monolithic Optical and Near-infrared Integral field spectrograph
VLT	Very Large Telescope
ELT	Extremely Large Telescope

ESO	E uropean S outhern O bservatory
IFS	I ntegral F ield S pectrograph
IFU	I ntegral F ield U nit
WFM	W ide F ield M ode
NFM	N arrow F ield M ode
NIR	N ear I nfra R ed
DR3	D ata R elease 3
DR4	D ata R elease 4
ΔC	$\Delta C_{F275W-2 \cdot F336W+F438W}$
ΔG	$\Delta G_{F275W-F814W}$

Physical Constants

Speed of Light	c	$=$	$2.997\,924\,58 \times 10^8 \text{ ms}^{-1}$
Solar Mass	M_{\odot}	$=$	$1.98840987 \times 10^{30} \text{ kg}$
Solar Radius	R_{\odot}	$=$	$6.957 \times 10^8 \text{ m}$
Solar Luminosity	L_{\odot}	$=$	$3.828 \times 10^{26} \text{ W}$
Gravitational constant	G	$=$	$6.6743 \times 10^{-11} \text{ m}^3/(\text{kg}\cdot\text{s}^2)$

In loving memory of my father, David Wragg . . .

Chapter 1

Introduction

“You are about to move into areas of the galaxy containing wonders more incredible than you can possibly imagine”

Q - Star Trek: The Next Generation

1.1 Globular clusters

The history of globular cluster observations is fraught with mistaken identity. In 1665, it was the German amateur astronomer Abraham Ihle who observed a strange object while observing Saturn in the constellation of Sagittarius (Lynn, 1886). Ihle observed that this object was less of a point source like the stars around it, but was diffuse and nebulous. Approximately 100 years later, the French born astronomer Charles Messier was reportedly annoyed by finding the same stationary objects while hunting for comets. Comet hunting was a popular pass time for astronomers of the time, however, comets appear diffuse when observed through a telescope and so stationary objects similar to those observed by Ihle often led to false discoveries. These false detections led Messier to catalogue a list of 103 stationary, diffuse objects visible in the northern hemisphere between 1758 and 1784 (Carroll & Ostlie, 2017). It is Messier who is credited to have first resolved individual stars in the cluster M4. We now know that that first observation by Ihle is a globular cluster known as M22. It was then in 1789 that William Herschel presented a second catalogue of ‘nebulae’ (Herschel, 1789), a large number of objects that could be resolved into structures of thousands of stars. It was also Herschel that first coined the name ‘globular cluster’.

In broad terms, star clusters in the Milky Way field are split into two categories: open and globular. Open clusters are typically described as groups of hundreds up to tens of thousands of stars. These systems are normally younger than 10^9 years, as they have a weaker gravitational potential, which prevents retaining cluster members for long periods of time. Open clusters are observed to host younger, bluer and more massive stars due to their age.

Globular clusters are typically described as groups of tens of thousands up to millions of stars. These systems are exceptionally old, with some globular clusters in the Milky Way estimated to be almost as old as the Universe itself due to the deep gravitational potential, which allows the cluster to retain members and survive the environment of the host galaxy. Globular clusters are observed to host an older (~ 10 Gyr), redder and less massive populations of stars, as only the least massive stars (typically F, G, K and M type stars) can live long enough to be observed today. For comparison, an example of both an open and globular star cluster is shown in Fig. 1.1.

The old age of globular clusters and their ability to survive within their hosts make them particularly useful objects to study in astronomy. They can provide minimum age limits for the Universe in simulations, act as markers and test particles in distant galaxies and may possibly provide insights into the conditions the cluster was formed under.

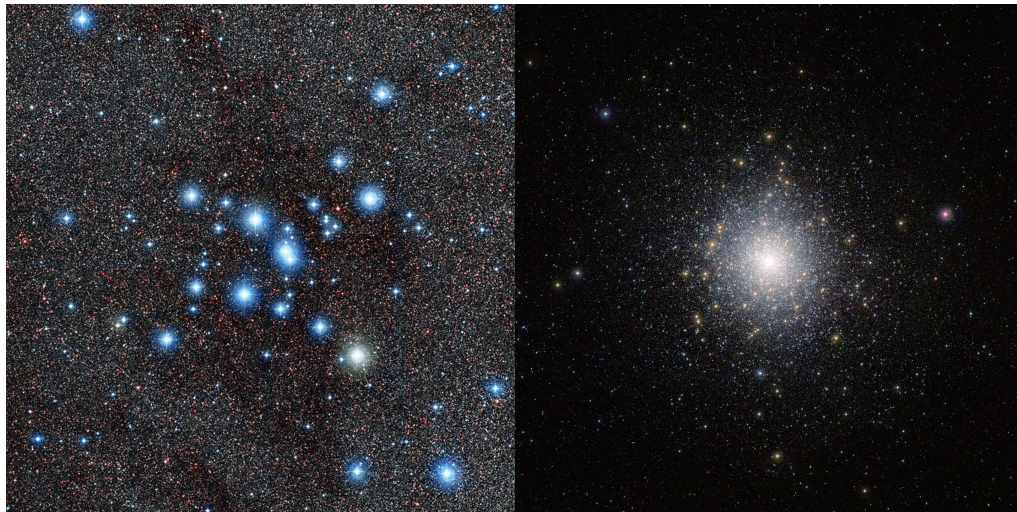


FIGURE 1.1: An example of both an open and globular cluster. On the left hand side we show Messier 7, NGC 6475, an open cluster ~ 200 Myr old (Villanova et al., 2009) within the tail of Scorpius. We see a looser cluster of stars that is populated with bluer and more massive stars. On the right hand side, we show 47 Tucanae (47 Tuc), NGC 104, a globular cluster ~ 13 Gyr old (Forbes & Bridges, 2010). The stars within the globular cluster are more tightly bound to the cluster and are redder and less massive. Messier 7 image credit (left): ESO, 47 Tuc image credit (right): ESO/M.-R. Cioni/VISTA Magellanic Cloud survey (acknowledgment: Cambridge Astronomical Survey Unit).

1.1.1 Cluster formation

1.1.1.1 Formation of massive star clusters

In modern astrophysics, there is a generally accepted view of what a globular cluster is. Although there is some debate when calculating the exact ages of globular clusters, globular clusters are typically $t \sim 10^{10}$ years old. They are also massive objects, with most clusters within the mass range $M \approx 10^4 - 10^6 M_{\odot}$. Despite having this view of globular clusters today, however, the topic of globular cluster formation has been hotly debated.

The most widely accepted model of in-situ cluster formation is via hierarchical mergers. This begins with “proto-clusters”, which form in high pressure, gas rich discs of young, “normal”, star forming galaxies at redshifts $z > 2$. Within the scale of a few Myr, the globular clusters slowly forms through the hierarchical merging of the smaller proto-clusters (Elmegreen & Falgarone, 1996; Hopkins, 2013). Typically, cluster formation efficiency and the maximum mass of a globular cluster increases with star formation efficiency, as galaxies with higher star formation rates are more likely to form a higher fraction of stars within clusters compared to “normal” galaxies (Adamo et al., 2011).

Other models of cluster formation suggest a connection between globular clusters and special conditions in low mass dark matter halos, during or before reionisation. There have been various suggestions which possibly link dark matter halos and cluster formation, such as H₂ cooling (Padoan et al., 1997), shocks induced by a hydrogen ionisation front (Cen, 2001), and the mergers of gas rich, star free mini halos (Trenti et al., 2015), however there is no overarching theory to consolidate these ideas to date.

1.1.1.2 Formation of globular cluster populations

The formation of globular cluster populations within galaxies is heavily reliant on both the survival of clusters that have formed in situ, and ex situ globular clusters that are accreted during galaxy mergers. After their initial formation, clusters then stay within the gas rich, high pressure disc environment of their host galaxy, in which frequent tidal shocks due to high density gas rapidly disrupt formed clusters (Lamers & Gieles, 2006). The disruption of newly formed clusters in the galactic disc continues until the cluster is forced into the galactic halo, typically due to galaxy mergers (Renaud & Gieles, 2013; Rieder et al., 2013). In merger processes, along with the in situ clusters migrating to the halo, the ex situ clusters from the merging galaxy are accreted into the halo of their new host.

The disruption of newly formed clusters is dependent on their environment within their host galaxy. This begins on formation, as the disruption of young globular clusters is strongly linked to gas density. This means that clusters in galaxies with higher mass get disrupted much faster and, therefore, their clusters have a much lower survival rate compared to clusters in less massive galaxies (Lamers et al., 2017). The higher rate of disruption of clusters in high mass galaxies continues during galaxy mergers, as galaxy mergers with mass ratios closer to unity allow for the most efficient migration of clusters into the halo. As the merger rate for equally or more massive galaxies decreases with higher galaxy mass (e.g Renaud & Gieles, 2013), clusters in massive galaxies experience a longer period of rapid disruption as they spend longer in the disc, which further lowers the survival rate of massive clusters. Galaxies that experience frequent galaxy mergers also have lower disruption rates of their clusters than galaxies in more quiescent environments that experience fewer mergers (Rieder et al., 2013).

When a cluster has reached the halo, the survival rate of clusters is far higher, with clusters now only being slowly disrupted through evaporation and a scarce few tidal perturbations (Spitzer, 1987; Gnedin et al., 1999; Fall & Zhang, 2001). As there are very few disruptive, external processes acting on the globular clusters that are securely

in the halo, very little evolution of cluster mass is seen. Instead, clusters are now able to structurally evolve freely.

1.1.1.3 Globular cluster population in the Milky Way

It was [Searle & Zinn \(1978\)](#) that first argued that some Milky Way globular clusters may have originated outside of our Galaxy and that, perchance, galaxy mergers and accretion could play an important role in the globular cluster population seen today. Indeed, in observations today, it is clear that both in situ and ex situ clusters make up a considerable fraction of the globular cluster population. Multiple studies have confirmed that the Milky Way has undergone a number of mergers and that a large population of globular clusters in the Milky Way, predominantly in the halo, formed outside of our galaxy. Furthermore, a number of studies (e.g. [Massari et al., 2019a](#); [Pfeffer et al., 2021](#)) have then traced a number of individual clusters back to previous merger events. A summary of these results is illustrated in Fig. 1.2 from [Massari et al. \(2019a\)](#), which shows a sample of Milky Way globular clusters. This shows some key differences between in situ and accreted clusters: in-situ clusters are characterised by low energies (tightly bound) and prograde rotation, while accreted clusters have higher energies and little or even retrograde rotation. It is thus clear that a considerable fraction of galactic globular clusters originate from other galaxies which have subsequently merged.

1.1.1.4 Links to young star clusters

The formation processes of globular clusters has historically been viewed as a phenomenon of the early universe ([Peebles & Dicke, 1968](#); [Fall & Rees, 1985](#)), however there are some potential links to younger clusters seen within the Large and Small Magellanic Clouds (LMC and SMC respectively). The young and intermediate age clusters within both the LMC and SMC have similar structural parameters compared to Milky Way globular clusters (for comparison, see [Song et al., 2021](#); [Baumgardt & Hilker, 2018](#)) and also show some chemical inhomogeneity ([Mucciarelli et al., 2009](#)), which is typically only seen within globular clusters (see Sec. 1.1.5 for further discussion). The links between these young and intermediate clusters and ancient globular clusters could be due to the star formation history (SFH) of their host galaxies. While the majority of star formation in the Milky Way, and therefore globular cluster formation, happened relatively early due to an early starburst (~ 12 Gyr), the LMC and SMC have a much broader SFH with more recent periods of star formation ([Harris & Zaritsky, 2009](#)). A comparison of the ages of globular clusters for the Milky Way and LMC/SMC is shown in Fig. 1.3, from which the extended SFH and globular cluster production of the LMC

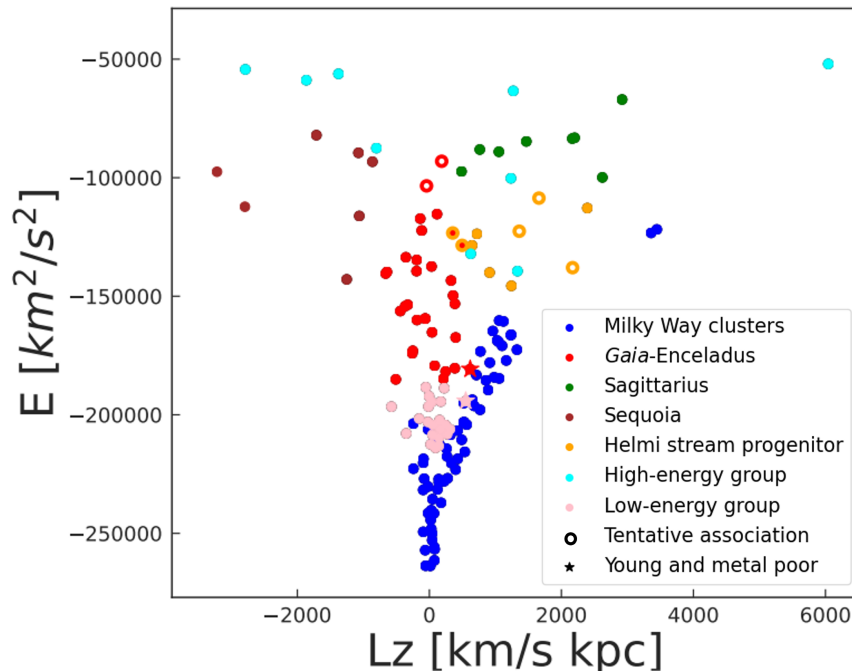


FIGURE 1.2: The globular clusters of the Milky Way colour coded to show the predicted origins of the cluster taken from [Massari et al. \(2019a\)](#). Each of the colours represents a separate source of globular clusters, which are shown in the legend. The y axis represents the energy of the cluster, which is a measure of how bound the system is to the galaxy, while the x axis represents the angular momentum of the cluster, which is used to show whether the cluster is in prograde or retrograde motion. Many of the clusters transferred to the Milky Way through mergers, namely the *Gaia*-Enceladus (red), Sagittarius (green) and Sequoia (brown), have higher energies and little or even retrograde motion, while the majority of the globular clusters formed in-situ are tightly bound and have prograde motion.

and SMC compared to the Milky Way can be seen. Direct comparisons between young massive LMC/SMC clusters and Milky Way clusters of a similar age is not possible due to the lack of young massive clusters within the Milky Way, and so further study is required to confirm this link between younger and older star clusters.

1.1.2 Cluster evolution

As discussed in Sec. 1.1.1.2, it is important to consider globular cluster evolution separately to cluster formation as, while the conditions that the cluster forms in may impact the evolution, many of the processes important to evolution are relatively internal and isolated from its host galaxy. There are a number of particularly important concepts when discussing the dynamic evolution of a cluster: relaxation time, mass segregation and core collapse. The extent to which a cluster has undergone dynamical evolution is described as the cluster’s “dynamical age”.

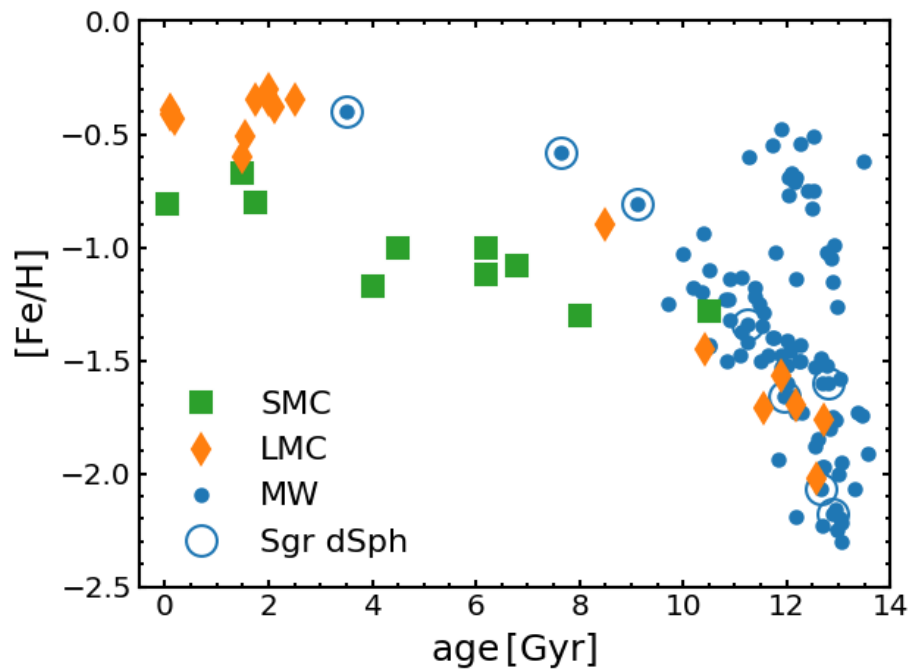


FIGURE 1.3: The age of clusters within the Milky Way, LMC and SMC using data provided by Kamann (priv. comm.), which shows the timeline for cluster formation. The majority of Milky Way clusters formed are older than ~ 8 Gyr, which suggests that the majority of star formation also happened within this time. The LMC and SMC have a more extended star formation, with a large fraction of clusters formed within the last ~ 2 Gyr.

Globular clusters are examples of “collisional stellar systems” in the universe. The densities of globular clusters makes it inevitable for cluster members to experience multiple gravitational interactions during their lifetimes, resulting in the regular exchanges of kinetic energy. An important factor is the relaxation time, which is defined as the timescale after which the energy of a particle changes by the order of itself. As seen in Eqn. 1.1 (Binney & Tremaine, 2008), the relaxation time of an average cluster member is dependent not only on the size of the cluster and the velocity of the cluster member, but also the total number of stars within the cluster:

$$t_{\text{relax}} \approx \frac{N}{8 \ln N} \frac{R}{v} \quad (1.1)$$

Where t_{relax} is the relaxation time, v is the average velocity of a cluster member, and N and R are the number of stars in the cluster and the distance from the cluster centre respectively. For stars in the centre of globular clusters, this relaxation time is shorter than the clusters age (Harris, 1996), suggesting that most clusters ‘forget’ their initial dynamical configuration and become relaxed. This happens through interactions and energy transfers between stars. We show the distribution of relaxation time as a function

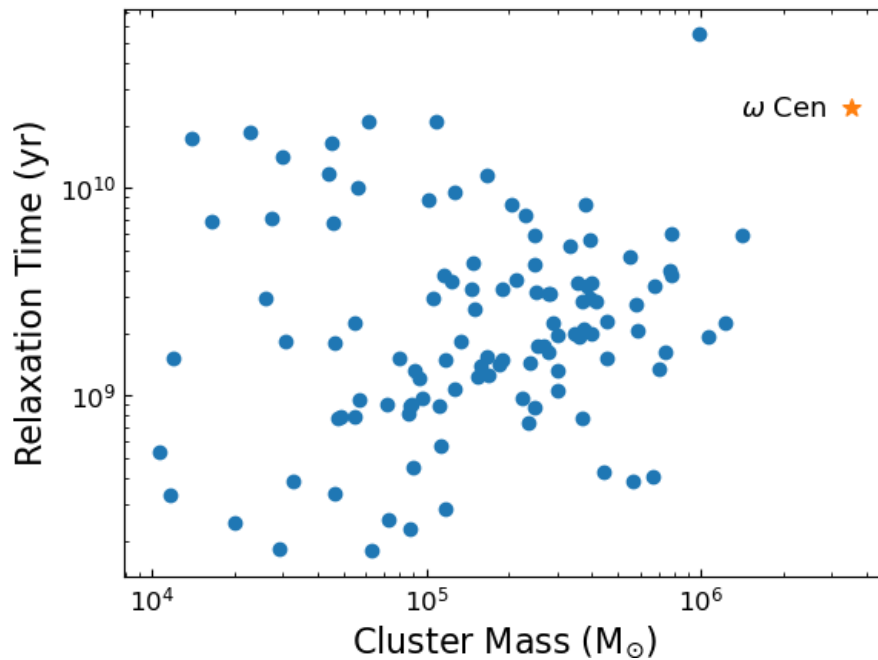


FIGURE 1.4: The half mass relaxation time as a function of cluster mass using the catalogue of globular cluster parameters by [Baumgardt & Hilker \(2018\)](#). We see that typically higher mass clusters have a longer relaxation time than lower mass clusters. The point marked with the orange star will be discussed in [Sec. 1.3](#).

of the total cluster mass for a variety of clusters in [Fig. 1.4](#) using the catalogue of cluster parameters by [Baumgardt & Hilker \(2018\)](#).

One of the effects of regular interactions is a state of “energy equipartition”, which describes the state in which stars all approach a similar specific kinetic energy, regardless of their masses. In practice, and on average, when a less massive star interacts with a more massive star, the less massive star will gain kinetic energy and escape further to the outer areas, orbiting with a higher velocity in the outermost regions of the cluster, while more massive stars lose kinetic energy and fall further towards the centre of the cluster, orbiting, with slower velocity, closer to the centre. After multiple interactions such as these, the cluster undergoes a process called “mass segregation”, in which the average mass of a star decreases with cluster radius. As an example, [Fig.1.5](#) shows how the stellar mass of cluster members of NGC 6293 are distributed within the cluster radius. NGC 6293 shows particularly pronounced mass segregation even within the clusters half light radius, with a positive stellar mass function slope in the innermost region of the cluster (shown in red), suggesting a larger fraction of higher mass stars, and a negative slope towards the clusters half light radius (shown in yellow), suggesting a larger fraction of lower mass stars. The result of mass segregation is the gradual stripping of low mass

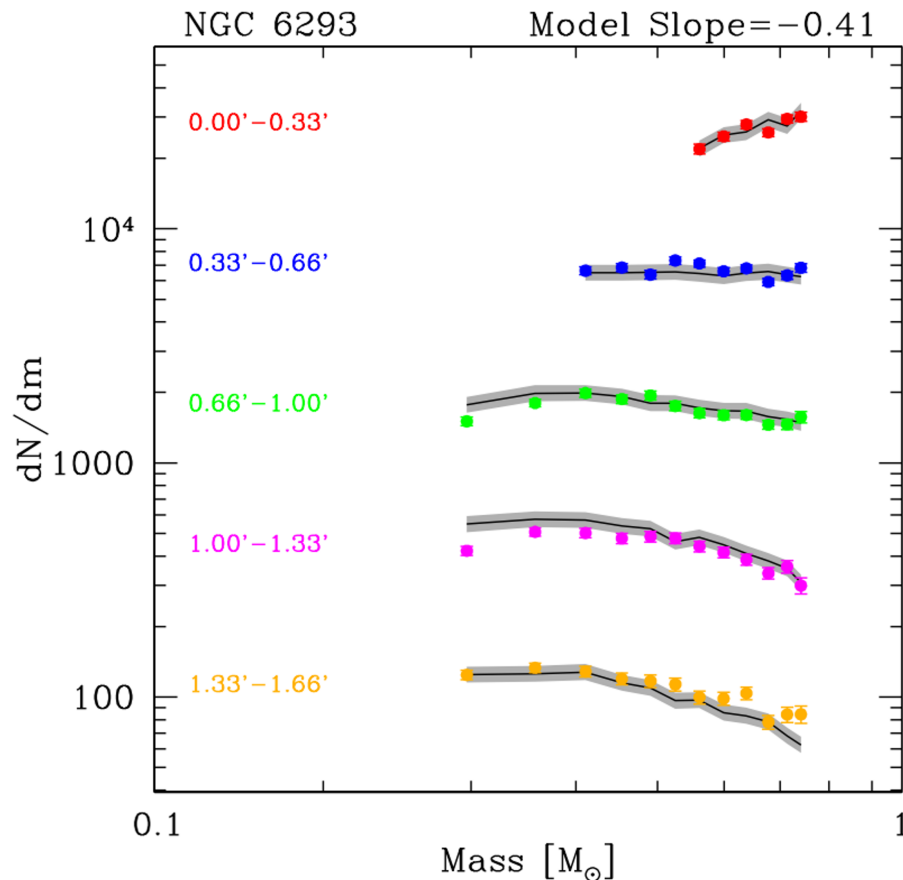


FIGURE 1.5: The distribution of mass within the cluster NGC 6293 taken from [Baumgardt & Hilker \(2018\)](#). The data points represent measurements based on star count, while the lines are the result of predictions from N-body models. The colours represent the range of separation to the cluster centre, and then shows the number of stars as a function of stellar mass. We see a positive slope within the closest separation from the cluster centre (seen in red), which shows a larger fraction of higher mass stars. At the furthest separation from the cluster centre (seen in yellow) we see a negative slope, which suggests that there are a larger fraction of low mass stars towards the half light radius.

stars, as they are more likely to be removed, with a typical globular cluster losing on average 75% – 90% of its initial mass over a Hubble time ([Baumgardt & Sollima, 2017](#)).

As the cluster becomes more and more segregated and the core becomes denser and “cooler” as kinetic energy is lost, the cluster becomes unstable in a state known as “core collapsed”, which is when a globular cluster is unable to prevent the most massive stars from falling into the centre. Due to the most massive stars infalling to the centre of the cluster, the surface brightness profile of a cluster can demonstrate whether or not the cluster is core collapsed, as displayed in Fig. 1.6 from [Noyola & Gebhardt \(2006\)](#), which shows the surface brightness profile for a variety of clusters. We see for non core collapsed clusters, such as NGC 5897 and NGC 5904 in Fig. 1.6, the surface brightness steadily increases with respect to the radius up until the core radius, where the surface

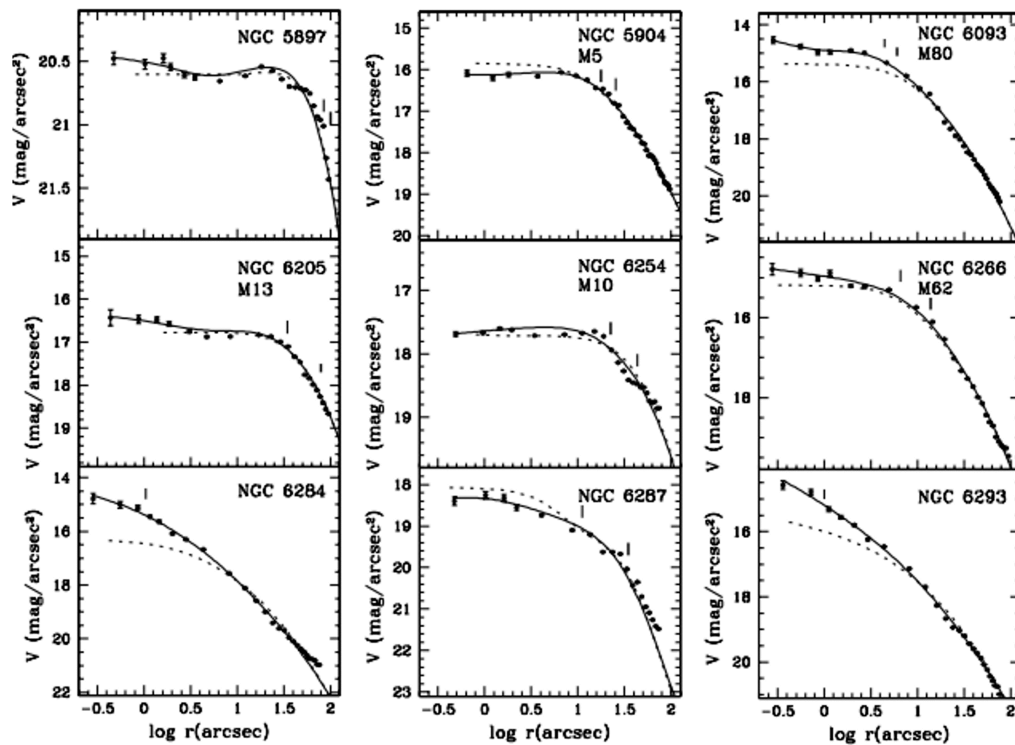


FIGURE 1.6: The surface brightness of a number of globular clusters as a function of radius, from [Noyola & Gebhardt \(2006\)](#). We see some examples of core collapsed clusters (e.g NGC 6284 and NGC 6293) with continuously increasing surface brightness profiles closer to the cluster centre, compared to core collapsed clusters (e.g NGC 5897 and NGC 5904), where surface brightness flattens towards the cluster centre.

brightness begins to plateau. In core collapsed clusters, such as NGC 6293 and NGC 6284 in Fig. 1.6, the surface brightness profile steadily increases even inside the core radius, which indicates that the most massive (and brightest) stars have fallen into the core radius. Due to their old age and relaxation times, all globular clusters should be core collapsed, however this contradicts observations, which show that less than 20% of globular clusters are core collapsed ([Harris, 1996](#)). The distinct lack of core collapse within globular clusters implies that there are other factors at play within these clusters that resist core collapse, such as dark remnants (e.g black holes) and binary stars which will be discussed in Sec. 1.1.3 and Sec. 1.1.4 respectively.

1.1.3 Black holes

The first suggestion of a body that was so massive that even light could not escape was a brief proposal in a letter by the English clergyman John Michell in 1784. The principles of a modern black hole were first described in 1915 by Albert Einstein's theory of General Relativity, but predicted that they should not exist in nature. A part of that theory

was the existence of Gravitational Waves (GW), small ripples in space time caused by accelerated masses, however in a similar vein, Einstein predicted that these would not be seen in nature as the effects would be too small. It was Karl Schwarzschild who then solved Einstein's field equations to show that they allow for a 'singularity'. From that point to the present, numerous studies have attempted to constrain the formation, evolution and properties of black holes. The term 'black hole' was not coined until the mid 1960s when a student reportedly suggested the phrase during a lecture by John Wheeler. Before this time, the term 'dark star' was commonly used as a name for the object, even being mentioned during multiple episodes of the classic TV show *Star Trek: The Original Series*.

Modern experiments such as the Advanced Laser Interferometer Gravitational-Wave Observatory (LIGO) and Advanced Virgo interferometers and the Event Horizon Telescope (EHT) have made great strides in the field. It was LIGO in 2016 (Abbott et al., 2016) that confirmed the first detections of gravitational waves, which answered three important points: GWs *do* exist in nature, the detections are completely consistent with General Relativity, and that stellar mass black holes can merge, confirming predictions made by Einstein and Schwarzschild over 100 years earlier.

1.1.3.1 Black hole classification

Our current understanding of black holes is that there are two parts to them. An outer area called the event horizon, this is the point at which light cannot escape and is what gives the black hole its "appearance". The centre of the black hole is the driving force behind the system, known as the singularity, which is the ultra dense high mass point source that is responsible for the gravitational forces. There are currently two confirmed types of black holes in the Universe: stellar mass black holes (BHs) and supermassive black holes (SMBH). Stellar mass black holes are normally the remains of stellar activity, forming when massive stars reach the end of their life and their cores compact to the point of degeneracy. It is the mass of the stellar core that determines if the star will become a black hole. If the stellar core is above the Oppenheimer-Volkoff limit of approximately $3 M_{\odot}$ (Bombaci, 1996), the star will collapse to a black hole.

SMBHs are similar to stellar mass black holes, but on a far larger scale. From observations of gas and stellar kinematics, SMBHs seem to reside in the centres of galaxies and have a mass of at least $10^5 M_{\odot}$. There are multiple suggestions for how these massive black holes form and grow, for example observations of the early universe suggest that SMBHs could form from primordial gas clouds (Volonteri, 2012). SMBHs may also arise from runaway merging of massive stars and stellar mass black holes, though this process

is metallicity dependent (Gieles et al., 2018b). Images taken by the EHT (Akiyama, 2020) show the accretion disk surrounding the SMBH at the centre of the galaxy M87. There have also been observations of the SMBH in the centre of our own galaxy, such as the Nobel prize winning observations by Ghez et al. (1998) and Schödel et al. (2002) of stellar orbits around the SMBH at the galactic centre.

By extrapolating the results of observations, it is reasonable for one to assume that, along with small stellar remnants and supermassive dark objects, there would be some black holes between the ranges of 10^2 and $10^5 M_{\odot}$. Black holes in this mass range are called intermediate mass black holes (IMBH). They have been predicted to exist in the Universe, although no confirmed detections have been made to date. From a theoretical view point, the gap between stellar mass and supermassive black holes is often described as the “forbidden range” as above $60 M_{\odot}$, the stellar core starts pair production. By producing electron-positron pairs, the pressure within the core caused by photon pressure is reduced (Stevenson et al., 2019), causing the core to suddenly collapse. For high mass stars, the core directly collapses into a black hole. For $60 M_{\odot}$ stellar cores, however, this process leads to the complete disruption of the star as it goes supernova (a so-called pair-instability supernova) and leaves no remnant (Heger & Woosley, 2002; Mapelli, 2018). It is important to note, however, that the $60 M_{\odot}$ limit on the stellar core is still very uncertain, and so it cannot be ruled out that stars form black holes slightly more massive than $60 M_{\odot}$.

A scenario for IMBH formation that is not directly caused by stellar collapse is long chains of mergers between black holes. This model suggests that large series of black hole mergers form more and more massive black holes (Mapelli et al., 2021), although this build up would only be possible in very particular environments and conditions (e.g massive, dense star clusters, see discussion in Sec. 1.1.3.2 and Sec. 1.2). IMBHs could also be formed due to multiple mergers in stars. If a massive star merges with multiple stars in a short time frame, this can trigger the collapse of a star resulting in a black hole with a mass $> 60 M_{\odot}$ (Kremer et al., 2020). Recently, LIGO/Virgo detected a particularly significant IMBH candidate, GW190521. The merger product was determined to have a mass of $\sim 142 M_{\odot}$, and is thought to have formed from a merger of two black holes with masses of $\sim 66 M_{\odot}$ and $\sim 85 M_{\odot}$ respectively (Abbott et al., 2020). This detection is a significant step in the search for IMBHs, as this suggests that mergers products reaching these masses are not only possible, but are also detectable.

1.1.3.2 Black holes in globular clusters

It has long been suggested that stellar mass black holes should form within globular cluster environments (e.g [Kulkarni et al., 1993](#)), but it was believed that only a small handful could survive the natal kicks and interactions that new black holes would experience. It was thought that black holes that were retained in the cluster would migrate to the centre, via mass segregation, and form an isolated interior structure with a short relaxation time, and that these black holes would be quickly ejected through dynamical interactions ([Spitzer, 1969](#)). In recent observations, however, we see that black holes are not only retained with globular clusters, but also interact with luminous cluster members ([Morscher et al., 2015](#)). Globular clusters are considered to be major contributors to observed GW rates, given the possibility to dynamically form binary pairs of black holes (see [Sec. 1.1.4](#)), although the fraction of their contribution is still debated ([Rodriguez et al., 2016](#); [Antonini et al., 2019](#)).

There have been a number of detections of stellar mass black holes in cluster environments (e.g [Maccarone et al., 2007](#); [Strader et al., 2012](#); [Chomiuk et al., 2013](#); [Miller-Jones et al., 2015](#)) using radio or X-ray observations to detect low mass X-ray binaries (see [Sec. 1.1.4.2](#)). Shown in [Fig. 1.7](#) is the velocity curve, using multi epoch spectroscopy, of a binary star in the globular cluster NGC 3201 from [Giesers et al. \(2018\)](#), which shows the star's observed radial velocity along with the best fitting orbital curve (shown in red). From this curve, the minimum mass of the companion was calculated to be $4.36 \pm 0.41 M_{\odot}$ ([Giesers et al., 2018](#)), which provides proof that this object must be a stellar mass black hole. This result is also particularly important, as it was the first detached (non-interacting) black hole that had been detected in a globular cluster. It is observations such as this that cement black holes as an important part of cluster evolution rather than exceptional objects ([Minniti et al., 2015](#); [Giesers et al., 2019](#)). It also highlights the importance of binary stars (further discussed in [Sec. 1.1.4](#)) in the hunt for black holes in globular clusters.

Although more massive stars were present during the early life of a typical globular clusters, allowing stellar mass black holes to form, the average mass of stars seen today within globular clusters is $\lesssim 1 M_{\odot}$. Due to the relatively high mass of stellar mass black holes compared with the current cohort of stars, it is natural to assume that, due to the energy transfer and mass segregation effects discussed in [Sec. 1.1.2](#), black holes would gravitate to the centre of the cluster, along with other higher mass objects such as white dwarfs and neutron stars. It is in the cores of the clusters that they prevent further infall, as black holes and other stellar remnants in the centre of the cluster provide a sort of barrier between the cluster core and stars falling into the centre. When a star falls into the centre, it will interact with a black hole and, as the black hole must be

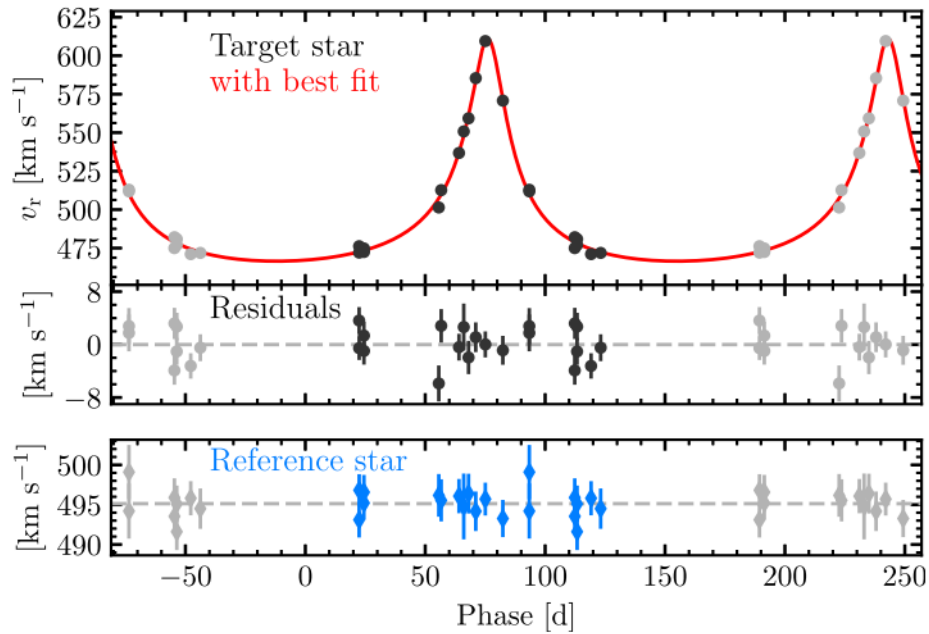


FIGURE 1.7: Radial velocity curve of a luminous star in NGC 3201 from [Giesers et al. \(2018\)](#). The observed radial velocity measurements are shown in black, and the best fitting orbital solution for the binary system shown in red. Using this, the minimum companion mass of the star was calculated to be $4.36 \pm 0.41 M_{\odot}$, which means the companion is a stellar mass black hole.

more massive than the current mass range of stars, the approaching star will, on average, gain kinetic energy through the encounter, which then moves the star to a wider orbit. This provides a large reservoir of kinetic energy or “heat” for the cluster to prevent the cooling associated with core collapse ([Askar et al., 2018](#); [Weatherford et al., 2020](#)). This implies that older clusters that have not yet undergone core collapse are likely to have a large population of black holes at the core.

Other than a large collection of stellar mass black holes, it is also important to consider the possibility of central IMBHs in clusters, as discussed in [Sec. 1.1.3.1](#). Indeed, IMBH formation may be the result of multiple mergers of stellar mass black holes within particularly massive clusters (see [Sec. 1.2](#)). It is important to remember, however, that even if IMBHs form within clusters, it is very likely that they would have been ejected from their host cluster due to the recoil kick that the merger product would receive due to the emission of gravitational waves. The likelihood that an IMBH will be retained in a cluster also decreases with each subsequent merger, as on average the kick velocity increases with each successive merger ([Fragione & Rasio, 2023](#)). In order for a cluster to retain a merger product, the natal kick must be lower than the clusters escape velocity, however the natal kicks that black hole-black hole (BH-BH) mergers typically receive is $\gtrsim 100 \text{ km s}^{-1}$, which is more comparable to the escape velocity of galaxies than star

clusters (Atri et al., 2019; Mapelli et al., 2021). As Milky Way globular clusters have escape velocities $< 90 \text{ km s}^{-1}$ (Baumgardt & Hilker, 2018), this means that only unusually massive clusters would be able to host IMBHs. The topic of IMBH and BH-BH merger product retention will be discussed further in Sec. 1.2.

There has been fierce debate on the topic of IMBHs in globular clusters, with a lack of clear evidence for or against and multiple studies attempting to identify potential IMBHs in clusters in the Milky Way. A study by Häberle et al. (2021) searched for an IMBH in the massive globular cluster NGC 6441 by searching for high velocity stars, as these are indicators of luminous stars in a binary orbit around a central IMBH. While the study could not conclusively say that there is an IMBH in the cluster core, the study also could not rule out the possibility. A study by Baumgardt et al. (2019) also investigated IMBH presence in Omega Centauri (ω Cen, NGC 5139), and NGC 6624. We show in Fig. 1.8 the surface density and velocity dispersion profiles for NGC 6624 compared to a range of IMBH mass N-body models, ranging from no IMBH to an IMBH which is 10% of the cluster mass. The study concluded that NGC 6624 showed no evidence of hosting an IMBH in the cluster center, which agrees with models by Gieles et al. (2018a) that, using data from Saracino et al. (2016), showed that NGC 6624 could be modelled without an IMBH. The models shown in Fig. 1.8 show some distinct differences within the central region of the cluster. For example, the models containing an IMBH show the surface brightness of the cluster flattening further from the cluster centre and the velocity dispersion increasing within the core radius. These effects show that an IMBH is effective at preventing core collapse within clusters, as when stars interact with the IMBH they gain kinetic energy which allows them to move further away from the cluster centre (Aros & Vesperini, 2023). The IMBH of modelling and observations will be discussed further in Sec. 1.3.

1.1.4 Binary stars

As will be demonstrated in this section, binary stars are a crucial element of the evolution of globular clusters. Despite their importance, and research into the dynamics of binary systems (e.g Heggie, 1975), there had been no observations of binary stars in globular clusters before the 1980s. Before this, and interpreted from the lack of spectroscopic binaries detected by Gunn & Griffin (1979), globular clusters were thought to be born with a significant lack of binary systems (Hut et al., 1992, otherwise known as “primordial binaries” created at the birth of the cluster). It was a study by Pryor et al. (1988) that observed singular spectroscopic binary in M3 which became the first of a many subsequent detections of binary stars in globular clusters, cementing binary stars

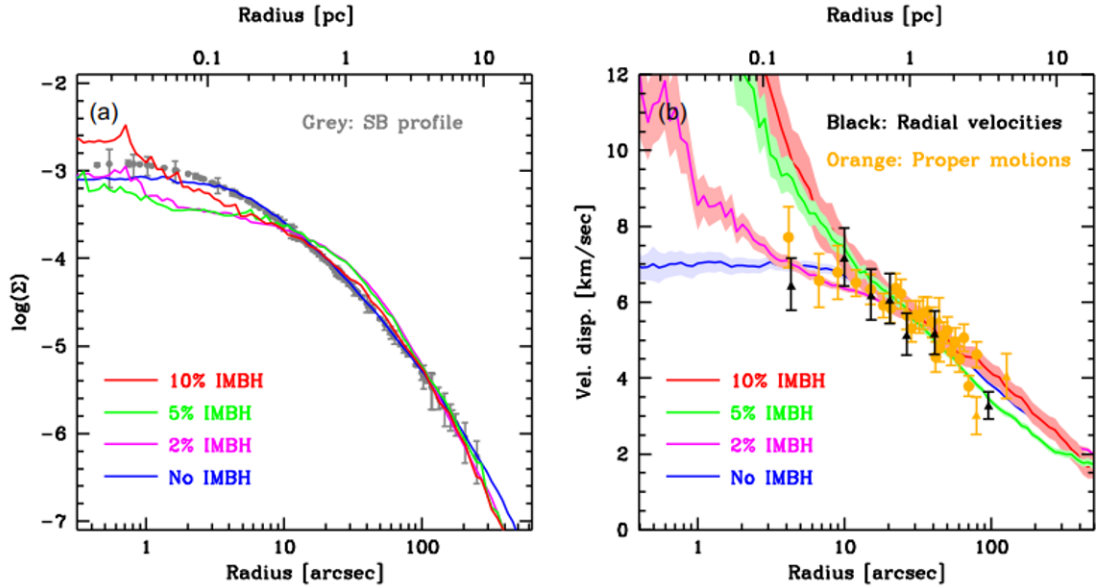


FIGURE 1.8: The surface density profile (left hand panel) and the velocity dispersion profile (right hand panel) of NGC 6624 compared to a number of models with a range of IMBH masses taken from [Baumgardt et al. \(2019\)](#).

as not only a standard of cluster formation but also as a crucial part of cluster evolution ([Heggie, 1975](#); [Goodman & Hut, 1989](#); [McMillan et al., 1998a](#)).

There are two types of binary systems: soft binaries and hard binaries. Soft binaries are defined as binary stars with a binding energy lower than the typical energy of a cluster member, while hard binaries are binary stars with a binding energy greater than the typical energy of a cluster member. Due to their weak connection, soft binaries are easily disrupted by a strong encounter with a star or another binary pair. Even though hard binaries can be disrupted, this only happens with particularly strong interactions with other binary pairs and often interactions actually harden the binary ([Ivanova et al., 2005](#)). When discussing binary systems and interactions from this point, this will pertain to hard binary systems. The hardness of a binary system is measured by η , which is defined in Eqn. 1.2 ([Ivanova et al., 2005](#)):

$$\eta = \frac{Gm_1m_2}{a\sigma^2\langle m \rangle} \quad (1.2)$$

Where η is the hardness of the system, m_1 and m_2 are the masses in the binary system respectively, $\langle m \rangle$ is the average mass of a star in the cluster, σ is the velocity dispersion of the cluster, a is the semi major axis of the system and G is the gravitational constant.

Using Kepler's third law, the semi major axis can be replaced by the orbital period, which allows a comparison between the hardness and the orbital period which can be used to constrain the upper limit for orbital period of a stable binary system in the cluster. For

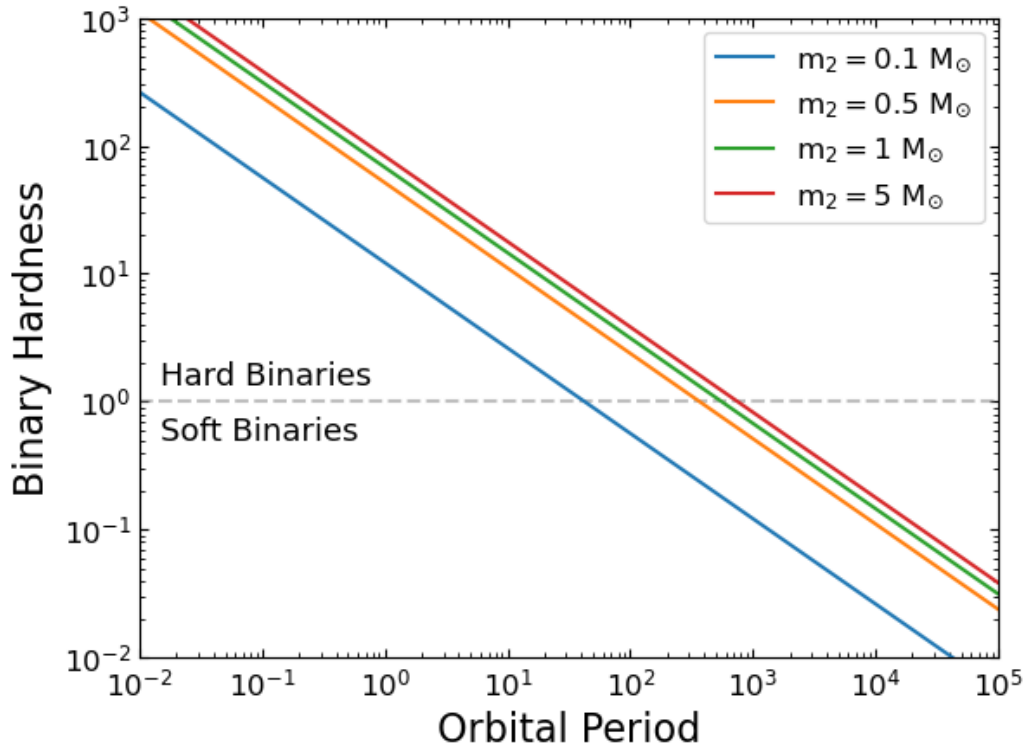


FIGURE 1.9: The correlation between binary hardness and orbital period for a range of companion masses, assuming both the primary star and mean cluster member has a mass of $0.5 M_\odot$. The hardness of a binary system increases as orbital period decreases, however the threshold of a hard binary is met at longer orbital periods for higher mass companions.

example, assuming that a test cluster has a velocity dispersion of $\sigma = 21 \text{ km}^{-1}$ (as is the case for ω Cen) and an average mass of $\langle M \rangle = 0.5 M_\odot$, a typical binary system would have a maximum orbital period of approximately 10^3 days. Using these same assumptions, the correlation between binary hardness and orbital period is shown in Fig. 1.9 for a variety of potential companion masses. The results of Figure 1.9 show that, for the same orbital period, an increased companion mass, such as a star with a black hole companion, makes the system harder and less likely to be disrupted.

We see in observations of binary systems an irrefutable link between binary stars and evolutionary processes within globular clusters. For example, the binary fraction of globular clusters is seen to decrease with radius (e.g., Milone et al., 2012d), which can be understood as a consequence of mass segregation (Hurley et al., 2007; Fregeau et al., 2009), as binary systems are by nature approximately double the mass of a typical cluster member. This has been seen in numerous studies of globular clusters, including the study of NGC 3201 by Giesers et al. (2019), from which Fig.1.10 shows that the binary fraction increases towards the cluster core for both observed (in blue) and simulated

data (in orange). There are a number of consequences to binary systems interactions, both binary-binary (when one binary system interacts with another binary system) and binary-single (when a binary system interacts with a single star): the destruction of the binary system, exchange interactions, the hardening or softening of the binary system or the binary system experiencing the Kozai-Lidov effect (see discussion below).

In the event that **the binary system is destroyed**, the incoming star or binary system completely disrupts the original system, and in the case of binary-binary interactions, both systems may be destroyed in the process. During **exchange interactions**, in both binary-binary and binary-single interactions, the stars in the interaction reconfigure to favour producing the highest mass binary system. This means if the single star is more massive than either star in the original binary, the least massive companion will be ejected and the single star will take its place. During binary-binary interactions, a higher mass binary system is formed similarly to the binary-single interaction, however the other binary system will be destroyed in the process, resulting in the highest mass binary system and two single stars. As this resulting binary system interacts with other systems in the cluster, on average the mass of a binary system will incrementally increase over time (Heggie, 1975). In the case of **hardening and softening binary systems**, this typically occurs in systems that are already considered hard or soft binaries respectively, as Heggie’s Law states that hard binaries tend to harden, while soft binaries tend to soften (Heggie, 1975). This is consistent with the trend seen that binary interaction products are commonly found in dense clusters (see Sec. 1.1.4.1 and Sec. 1.1.4.2). The final interaction is the **Kozai-Lidov effect** (Kozai, 1962; Lidov, 1962; Naoz, 2016), which happens in hierarchical triple systems (Antonini et al., 2016). In this case the orbit of the inner binary system is perturbed by the third star, which leads to the eccentricity and inclination of the inner binary system oscillating.

Interactions between binary systems are also a crucial factor for retarding core collapse. In essence, a cluster can repel the effects of core collapse by “burning” binary pairs in a similar way to a star burning Hydrogen. While the energy transfer processes discussed in Section 1.1.2 can act as a transfer of kinetic energy from the higher mass star to the lower mass star, binary stars act as an exchange pool of energy, where kinetic energy can be withdrawn or deposited. For example, if a more massive star falling towards the centre of the cluster interacts with a binary pair, it is possible for the in-falling star to capture a portion of the binding energy of the binary system and convert it to kinetic energy, allowing the star to stay in orbit further from the cluster centre. The binding energy acts as a reservoir which allows the stars to resist the effects of mass segregation within the cluster core and, in turn, allows the cluster to resist core collapse.

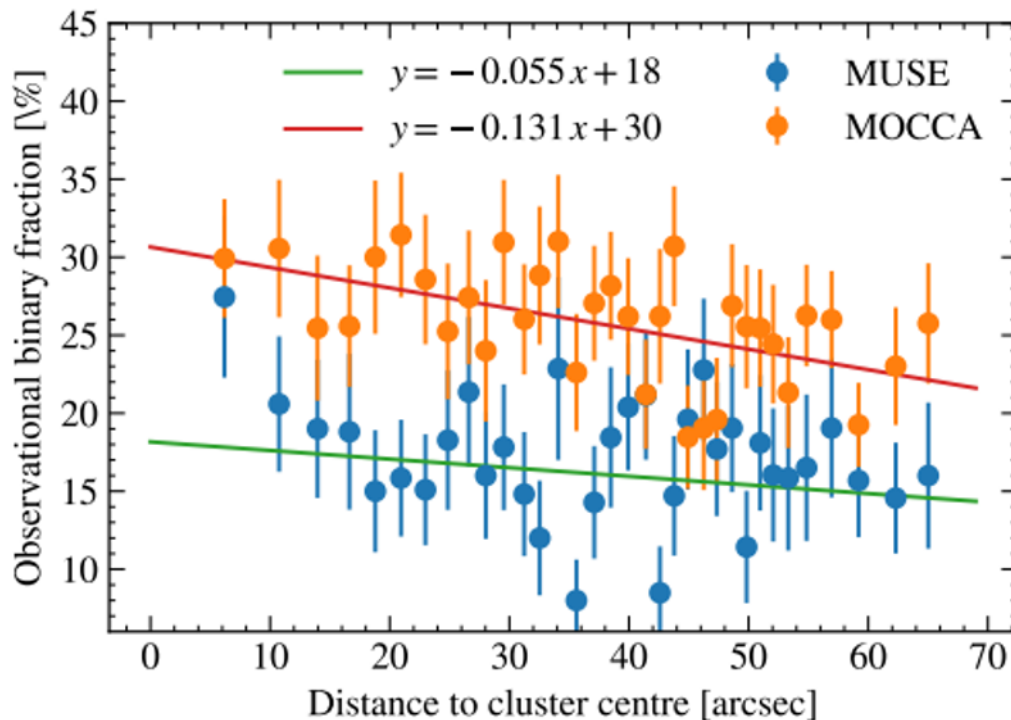


FIGURE 1.10: The binary fraction as a function of the distance from the cluster centre of NGC 3201 from [Giesers et al. \(2019\)](#). Observed data are shown in blue, while simulated data are shown in orange. Both distributions show that binary fraction increases closer to the cluster centre.

Even when a cluster goes into core collapse, binary stars play an important role. As stars fall into the centre and the core becomes denser, existing stars are more likely to form binary systems via three body interactions. The binary star systems that form then provide this same reservoir of energy that stars then use to move out of the core. This continues until the new binary systems are destroyed by this, at which point the core collapses once more. This cycle of binary systems forming and being destroyed produces oscillations in the core called post core collapse oscillations ([Fregeau et al., 2003](#)).

Among field stars, binary stars are common, with a typical binary fraction of $> 50\%$ ([Duquennoy & Mayor, 1991](#); [Duchêne & Kraus, 2013](#)), with the incidence of more massive stars in binary systems or in systems of three or more stars even greater due to a strong dependence on stellar mass ([Offner et al., 2023](#)). Globular clusters, however, typically have a binary fraction far lower than 50% , and the number of systems with three or more stars is thought to be significantly lower than the field ([Fragione et al., 2020](#)). Indeed, spectroscopic studies of M4 by [Sommariva et al. \(2009\)](#) and of NGC 3201 by [Giesers et al. \(2019\)](#) report global binary fractions of $3.0\% \pm 0.3\%$ and $6.75\% \pm 0.72\%$, respectively. The photometric study of 59 galactic globular clusters by [Milone et al. \(2012b\)](#) also supports a lower global binary fraction, which for most clusters falls between 2% and

15%. This discrepancy between field and cluster stars can be explained by the density of star cluster environments which causes a high frequency of dynamical interactions (e.g binary-binary and binary-star interactions), as this makes the disruption of binaries, and particularly soft binaries, more likely (Heggie, 1975).

Due to both the frequency of dynamical interactions and the naturally higher chance of binary disruption, the observed binary fractions we see today cannot be easily converted to a primordial binary fraction (Hut et al., 1992). The primordial binary fractions used in studies today are still poorly constrained, as simulations of globular clusters using a wide range of primordial fractions, between 5% (Hurley et al., 2007) and 100% (Ivanova et al., 2005), are able to reproduce the observed fractions. Studies of young massive clusters (ages $\lesssim 10$ Myr), such as 30 Doradus (Sana et al., 2013; Dunstall et al., 2015), Westerlund 1 (Ritchie et al., 2022), or NGC 6231 (Banyard et al., 2022) report binary fractions between 40 and 55%. These results suggest, assuming young massive clusters are representative of young globular clusters, that the primordial binary fractions of globular clusters were indeed much higher than the fractions observed today. However, care must be taken when comparing young massive clusters and ancient globulars, as results for each cluster class are based on very different populations of stellar mass and that the likelihood of a star in a young massive cluster being in a binary system is strongly linked to stellar mass (see Offner et al., 2023, for a recent overview).

1.1.4.1 Blue straggler stars

Due to binary interactions being so common in cluster environments, it is natural to expect that the products of these binary interactions are still present within globular clusters. One of the interaction products we observe in clusters is Blue Straggler Stars (BSS). It was Sandage (1953) that first detected BSS in the form of an extended branch of the main sequence toward bluer and brighter areas of the colour magnitude diagram (CMD). The detection of blue stragglers highlighted the incomplete understanding of stellar evolution and star formation within clusters. If BSS formed through a typical star formation process, they would have had to have formed several giga-years after the main population and would have also caused a widening of the main sequence and red giant branch, which is not seen (e.g Williams, 1964). It was both McCrea (1964) and van den Heuvel (1967) that first put forward the idea that BSS formation may be linked to binary activity. It is now understood that BSS are not only a ubiquitous and integral element of globular clusters (Ferraro & Lanzoni, 2009), but also linked to cluster evolution (Bailyn, 1995) and the evolution of the binary population within a cluster.

There are two widely accepted explanations for the BSS formation process: through mass transfer and stellar collisions within binary systems (Stryker, 1993). Mass transfer BSSs are thought to form either through a binary system hardening to the point at which mass transfer starts, or from the more massive companion in a binary system evolving off the main sequence and expanding, with both cases resulting in mass transfer. Collisional BSSs, on the other hand, are thought to form as a result of dynamical interactions with other binary systems or single stars, resulting in a stellar merger which forms the BSS (Leonard, 1989; Fregeau et al., 2004). This is seen in observations of separate tracks of the BSS population, as illustrated in the CMD of M30 in Fig. 1.11, which shows isochrones for both the mass transfer (red) and collisional (blue) branches. The dominant formation of BSSs is thought to be dependent on the evolutionary stage of the host cluster. This is seen in Fig. 1.11 as the mass transfer BSS branch is broader than the collisional BSS branch, which suggests that the branches formed at different times and is concurrent with the theory that collisional binaries form later in the cluster lifetime (Ferraro et al., 2009). Mass transfer BSSs are thought to form gradually during the evolution of the cluster’s first binary systems, which leads to the creation of a population of “primordial blue stragglers” (Ferraro et al., 2009; Hypki & Giersz, 2017). The formation of collisional BSSs is thought to be linked to core collapse (see Sec. 1.1.2) as, theoretically, denser environments, such as the core of a core collapsed globular cluster, would lead to a higher fraction of collisional BSS (Hypki & Giersz, 2017). The distribution of collisional BSSs in Fig. 1.11 agrees with this theory, as a narrower distribution suggests these BSSs likely formed during a single event. This is because if collisional BSSs form through a single event, such as core collapse, they will all have the same age, and hence can all be described by a single isochrone. It is clear from Fig. 1.11, however, that both formation processes contribute to the overall BSS population within clusters.

A higher BSS binary fraction compared to the global globular cluster population is well documented (Sollima et al., 2008; Milone et al., 2012b). In the study of NGC 3201 by Giesers et al. (2019) a BSS binary fraction was calculated to be $57.5\% \pm 7.9\%$, significantly higher than the global fraction of $6.75\% \pm 0.72\%$. The combination of formation theory and the simulations and observations of globular clusters are consistent with the concept that BSS are more likely to be in binary systems than typical cluster members.

1.1.4.2 Other exotic objects

Along with blue stragglers, there are a number of exotic binary interaction products that are observed within globular clusters today. **Cataclysmic variables (CVs)** are close binary systems where a white dwarf accretes mass from a red dwarf or subgiant. The dense environments of clusters also influence CVs, as a study by Ivanova et al. (2006)

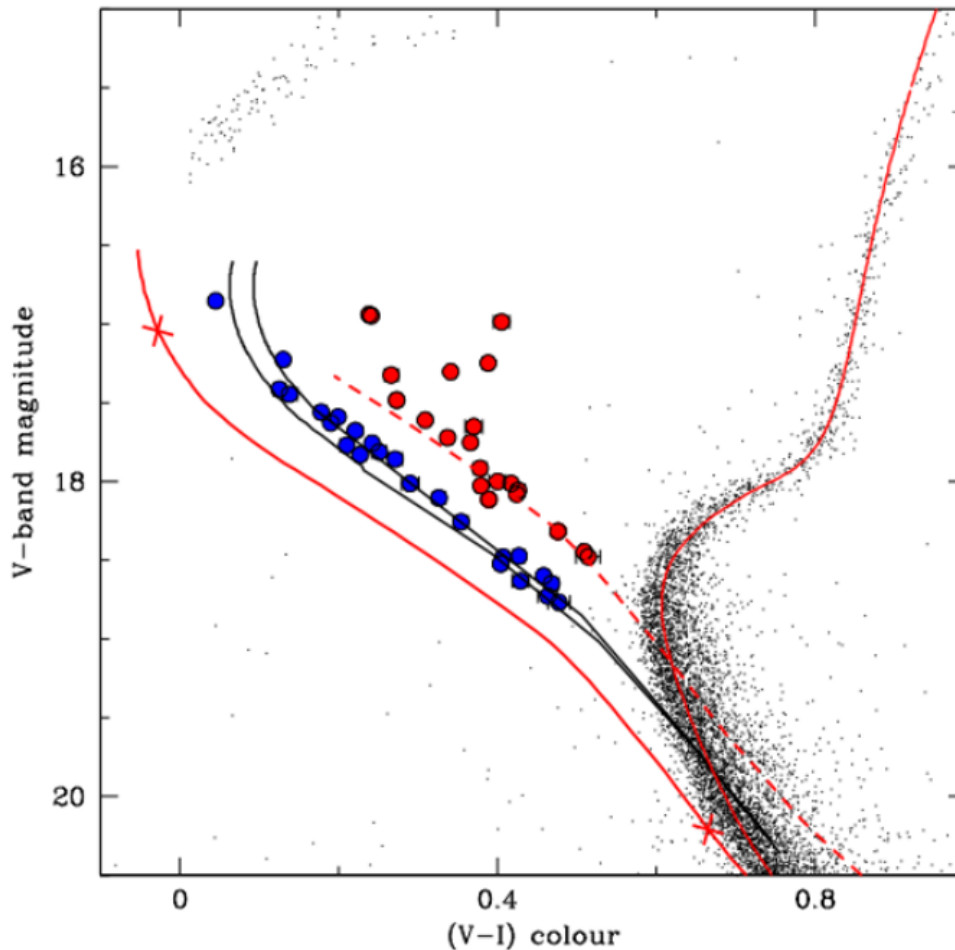


FIGURE 1.11: The blue straggler star region of the CMD of M30 from [Ferraro et al. \(2009\)](#), with identified BSS stars marked with larger points and isochrone tracks marked with lines. The red points and red dashed line represent BSS formed through mass transfer and the corresponding isochrone, and blue points and black solid line represent BSS formed through collisions and corresponding isochrone. The red solid lines correspond to the single star isochrones respectively corresponding to 13 Gyr (well fitting the main cluster evolutionary sequences) and to 0.5 Gyr (representing the reference cluster zero-age main sequence)

found that up to 50% form via binary encounters. In globular clusters these systems are relatively faint and spectra of these objects are rare ([Göttgens et al., 2019](#)).

Red stragglers (RSs), also named **sub-subgiants (SSGs)**, are systems that reside in the region of the CMD that is redder than the MS branch and fainter than the subgiant branch. There have been multiple formation scenarios proposed for SSGs and RSs, and it is clear that the evolution of these stars cannot be explained by the evolution of a single star ([Geller et al., 2017a](#)). The formation scenarios of SSGs and RS explained in [Geller et al. \(2017b\)](#) and [Leiner et al. \(2017\)](#) all include an element of binary evolution: isolated binary evolution, the rapid stripping of a subgiant’s envelope, or stellar collisions. **Millisecond pulsars (MSPs)** are rotating neutron stars with periods within

the range of 10^{-3} seconds that are spun up (or “recycled”) by accreting matter from their companion star in a close binary systems (Tauris & van den Heuvel, 2006).

Along with cluster evolution, black holes also have an important impact on binary systems in clusters. An example of this is **low-mass X-ray binaries (LMXBs)**, which are compact systems consisting of either a black hole or neutron star and a less massive star which transfers mass to the companion (Tauris & van den Heuvel, 2006). Black holes also have an effect on the overall binary fraction of a cluster. As shown in simulations by Aros et al. (2021), the radial distribution of binary stars sensitively depends on the number of black holes, or the presence of an IMBH, inside the cluster. As discussed in Sec. 1.1.2, the presence of a large black hole mass can act as a preventative for core collapse, and in turn mass segregation. Therefore, if a cluster has a substantial black hole component, either as a higher number of stellar mass black holes or an IMBH, the cluster will show less mass segregation. A low mass segregation also corresponds to a flatter distribution of binary stars, as binary stars would typically be more centrally concentrated due to their mass compared to a typical cluster member. The result of the simulations by Aros et al. (2021) also showed that the radial distribution of binaries (i.e. mass segregation) in clusters hosting an IMBH was significantly flatter than a cluster hosting a collection of black holes. As such, studying the properties and distribution of binary systems inside globular clusters promises to offer new insight into the distribution of unseen mass inside the clusters.

1.1.5 Multiple populations

The classic image of a globular cluster is a singular, simple stellar population of stars, all with the same ages and abundances. It has become clear that this static image of a globular cluster is not the case, as almost all globular clusters boast a significant spread of light element abundances (e.g. Carbon, Nitrogen, Oxygen, etc.) (Lee et al., 1999; Kraft, 1994). These multiple populations can be split into two broad groups, primordial stars (1P), which have a similar abundances to field stars with the same metallicities, and enriched stars (2P), which are enriched in some elements (e.g He, Na, Al) and depleted in others (e.g O, Mg, C) compared to field stars with the same metallicities. In some clusters, however, the 2P population can split into a number of sub-populations with varying levels of element depletion and enhancement. Enriched stars tend to make up the majority of stars in a cluster and are typically more concentrated in the centre of the cluster than primordial stars (D’Ercole et al., 2008), despite being exceedingly rare within the field (Martell et al., 2011; Ramírez et al., 2012). This concentration and ratio of 2P stars in central regions, however, is debated and studies have shown that it is dependent on cluster mass (e.g Leitinger et al., 2023; Cadelano et al., 2024).

The topic of multiple population formation is one of the most fiercely debated in the subject of globular clusters. To date, there is no generally accepted model for multiple population formation, however the majority of proposed formation scenarios are based on one fundamental model (e.g. [D’Ercole et al., 2008](#); [Valcarce & Catelan, 2011](#)): 1P stars form first within the cluster, pollute and enrich the remaining gas within the cluster, which then goes on to create 2P stars (exceptions to this scenario include [Bastian et al., 2013](#)). Despite this concept, however, the method in which the gas is enriched with light elements is hotly contested. The most popular models to date include AGB winds (e.g. [Cottrell & Da Costa, 1981](#); [Dantona et al., 1983](#); [Ventura et al., 2001](#)), fast rotating massive stars (e.g. [Prantzos & Charbonnel, 2006](#); [Decressin et al., 2007](#); [Krause et al., 2013](#)), massive interacting binaries (e.g. [de Mink et al., 2009](#); [Bastian et al., 2013](#)) and very massive stars formed by runaway stellar collisions (e.g. [Denissenkov & Hartwick, 2014](#); [Gieles et al., 2018b](#)).

Despite there being a number of models on the origin of multiple population formation, the ratio of 2P to 1P stars creates a fundamental tension, known as the “mass-budget problem”. The issue that arises from the concept that 1P polluted gas goes on to form 2P, is that the mass of the material that 1P stars eject into the surrounding gas that has the light element abundance pattern required to create 2P stars is only a small fraction of what would be needed to create the mass of 2P stars we see in globular clusters today ([Prantzos & Charbonnel, 2006](#)). According to the requirements of the 2P population, globular clusters would have to have been much more massive at formation, by a factor of $\sim 5 - 20$ (e.g. [Renzini, 2013](#)). Initial solutions included the cluster losing a fraction of the 1P population, however a suite of simulations by [Reina-Campos et al. \(2018\)](#) showed that dynamical cluster mass loss was unable to reproduce observed conditions. There is, to date, still no clear solution to this discrepancy, and research attempting to resolve this tension is still ongoing.

Observationally, there are a few methods to visualise and identify multiple populations within globular clusters. One of the key features of multiple populations is each population’s chemical abundances. By observing the cluster spectroscopically, the abundances of each element can be determined for each star and when plotted, show distinct correlations and highlight the different populations. Shown in [Fig 1.12](#) is the CMD of the globular cluster NGC 6752 along with a number of element abundance comparisons from [Bastian & Lardo \(2018\)](#), with each distinct population marked with different colours. The element abundances of multiple populations can also have an effect on the photometry of each star, and so multiple populations can also be separated in what is known as a “chromosome map” (discussed further in [Sec. 5.1](#)). The chromosome map shown in [Fig. 1.13](#) from [Milone et al. \(2017\)](#) shows the grouping of the populations within a globular cluster. Broadly speaking, the y axis of the chromosome map can be used as

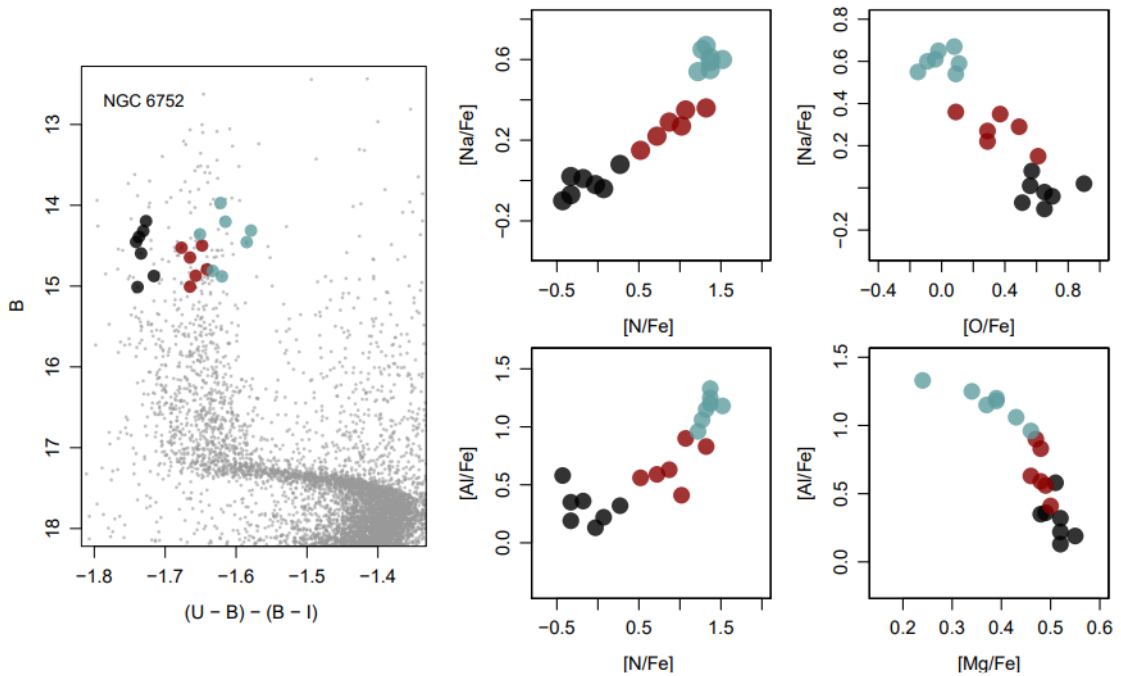


FIGURE 1.12: Spectroscopic analysis of multiple populations in the globular cluster NGC 6752 from Bastian & Lardo (2018). On the left hand side, the RGB sequence of the cluster is marked on the CMD, while the right hand side shows a of comparison of element abundances, with each separate population marked with different colors.

a proxy for the abundance spread in some elements, in particular Nitrogen, while the x axis can be used as a proxy for the abundance spread of Iron and also for the depletion of Helium within 1P and 2P stars. It is important to note, however, that these are only approximations. In some more unusual cases, multiple populations can be seen in the CMD as a splitting of the MS, into a redder and bluer branch, as seen in Fig. 1.14. From the CMD of NGC 2808 from Milone et al. (2012a), we see distinct populations within the MS region, although it is important to note that this is due to a particularly high spread in Helium within the cluster, which impacts how blue a star appears, and this phenomenon is relatively rare.

Clusters are typically split into “Type I” and “Type II” depending on the characteristics of their multiple populations. Type I clusters make up the majority of clusters within the Milky Way, but are characterised by a relatively “simple” chemical abundance spread: a 1P and a 2P population with similar metallicities. Type II clusters have a more complex chemical composition and are rarer than their Type I counterparts, only accounting for 15 – 20% of Milky Way globular clusters (Milone & Marino, 2022). Type II clusters are identified by having at least one of three markers: at least one additional group to the 1P and 2P populations in the cluster’s chromosome map (on the red side), split or broad SGB and RGB branches in the cluster’s CMD, and, most unusually for globular clusters, a significant spread in metallicity (Milone et al., 2017).

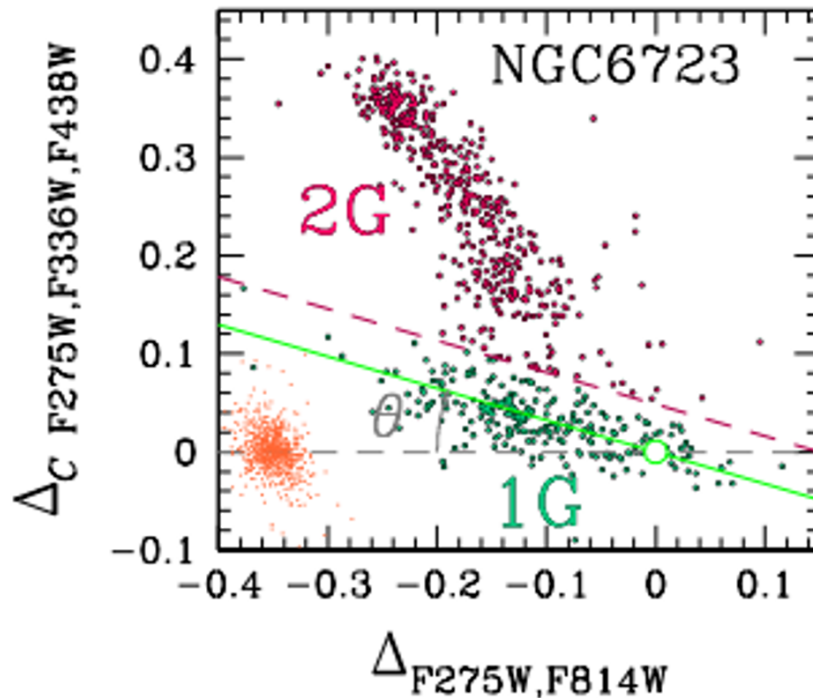


FIGURE 1.13: The chromosome map of NGC 6723 taken from [Milone et al. \(2017\)](#). This shows the separation of two stellar populations, 1P and 2P stars, which are labelled accordingly.

We can see the first and last points clearly in Fig. 1.15, which shows a comparison of chromosome maps for a Type I and a Type II globular cluster. While the Type I cluster (the same cluster as shown in Fig. 1.13) shows a relatively simple example of two groups with little metallicity variation that are clearly separated, the Type II cluster shows a more complex structure, including the additional population marked in red. Type II clusters also include some of the most massive clusters in the Galaxy, which suggests that these clusters being able to retain ejected material from events such as supernovae may have an effect on the fraction of 2P stars, and that a high mass may be needed to create the features seen in these clusters ([Marino et al., 2015](#)).

There are some typical behaviours of multiple populations in globular clusters, along with some dependence on their host cluster. For example, recent work has shown that cluster mass has an impact on multiple populations. The fraction of 2P stars in Milky Way globular clusters varies significantly with cluster mass, ranging from less than 40% in low mass clusters, to over 90% in the highest mass clusters ([Milone et al., 2017](#)). In addition to this, we also see that the internal variations of some light element abundances, such as Nitrogen and Helium, also seem to increase with cluster mass ([Lagioia et al., 2019](#)). Despite this, it is interesting to note that there is no clear dependence for multiple populations on individual stellar mass, as studies have shown that the abundances of

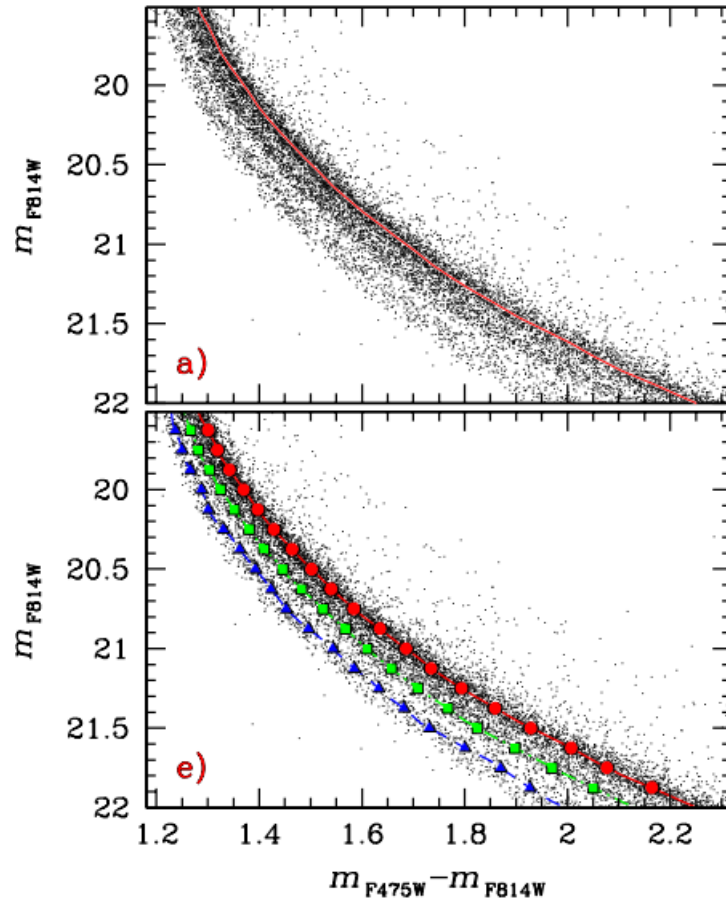


FIGURE 1.14: The CMD of the globular cluster NGC 2808 taken from [Milone et al. \(2012a\)](#) which, due to an extreme spread of Helium within the cluster, shows three split channels of the main sequence, which corresponds to distinct populations separated through light element abundance.

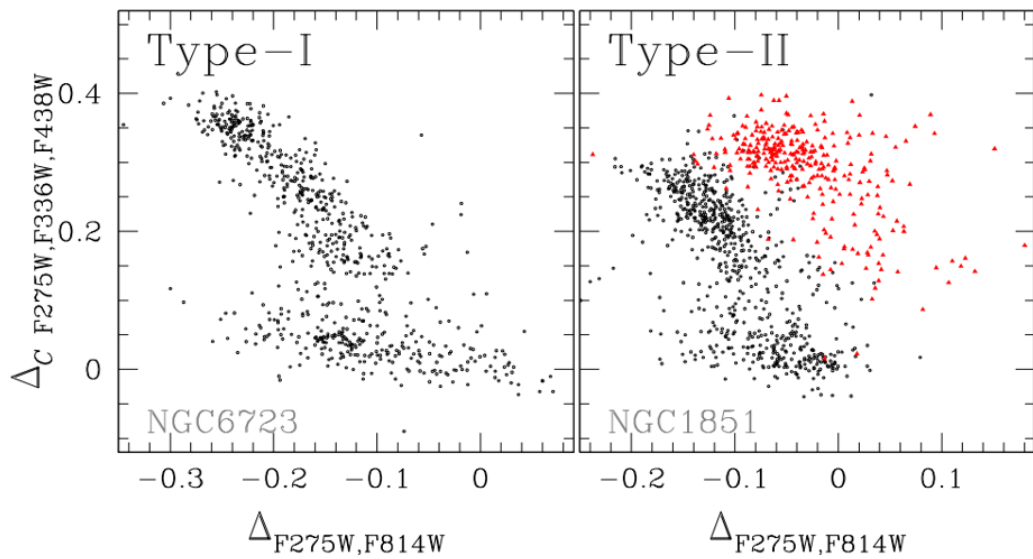


FIGURE 1.15: A comparison of chromosome maps for a Type I cluster (NGC 6723, left) and a Type II cluster (NGC 1851, right) from [Milone & Marino \(2022\)](#). This shows a number of distinct differences between Type I and Type II clusters, as the Type II cluster shows a distinct third population in red (photometry from [Milone et al. \(2017\)](#)).

very low mass stars are consistent with their more massive counterparts (Milone et al., 2014, 2019).

Different populations also have different spatial distribution within the cluster, which can act as a “fossil record” of when, where and how each population formed. In Type I clusters, 2P stars tend to be more centrally concentrated than 1P stars, which seem to reside towards the outer regions of the cluster (e.g Milone et al., 2012c; Cordero et al., 2014; Lee, 2017), although the distribution of populations for some Type I clusters have been observed to be more mixed (e.g Dalessandro et al., 2018; Milone et al., 2019; Dondoglio et al., 2021; Leitinger et al., 2023). These results are consistent with the scenario that 2P stars are formed more centrally than the 1P population and, while some clusters have retained that initial distribution, some clusters have become more mixed due to dynamical evolution (Vesperini et al., 2013). These behaviours are only typical for Type I clusters, however, as the distribution of populations in Type II clusters are poorly studied.

1.1.5.1 Multiple populations in binaries

The binarity of multiple populations is another important behaviour of multiple populations, again with links to cluster evolution and the other observed features. Overall, among Type I clusters, 1P stars tend to have a higher binary fraction than their 2P counterparts. This is seen in a number of observations, such as the study by Lucatello et al. (2015), which concluded that the fraction of 1P binary systems was 4.1 ± 1.7 times larger than the fraction of 2P binaries. This is consistent with observations that 2P stars tend to be concentrated in the denser environment of the cluster centre, in which binary systems are more likely to be disrupted (Dalessandro et al., 2019). Similarly, a study of NGC 6362 by Dalessandro et al. (2018) found a striking difference between the fraction of 1P stars in binary systems, $\sim 14\%$, compared to the fraction of 2P stars in binary systems, $\sim 1\%$. Another study of NGC 3201 by Kamann et al. (2020) reported an observed binary fraction of $23.1 \pm 6.2\%$ for 1P stars and $8.2 \pm 3.5\%$ for 2P.

There have also been a number of simulations on the binary fractions of multiple populations, which agrees with many of the observations. Simulations by Hong et al. (2015) and Vesperini et al. (2011) both show that 1P stars are more likely to be in binary systems than 2P stars. Results such as these suggest that this distribution may be a “fingerprint” of the populations formation, and are also consistent with the current understanding that 2P form in the inner regions of the cluster (Vesperini et al., 2013). Due to this radial distribution, 2P binary systems may have a higher disruption rate than the 1P binary population due the high density environments that 2P stars are more

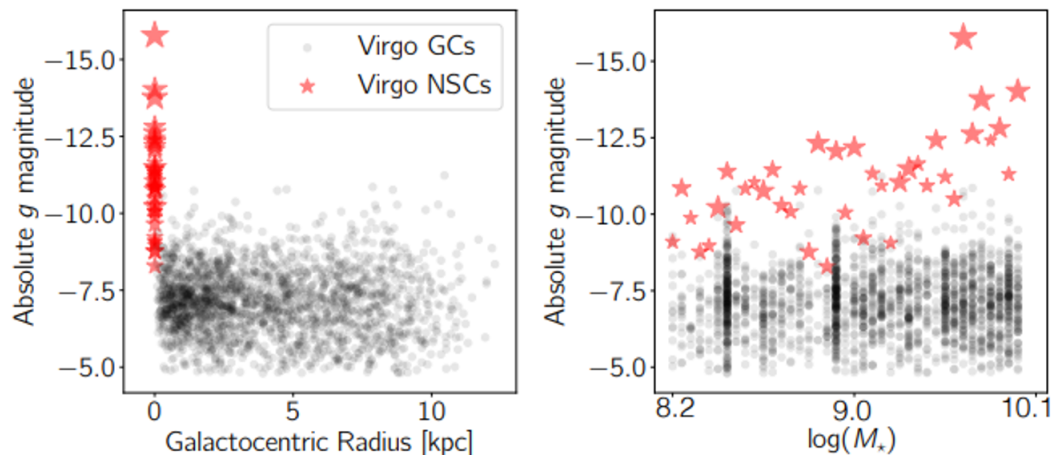


FIGURE 1.16: A comparison of the observed characteristics of globular clusters and NSCs, taken from [Neumayer et al. \(2020\)](#). The left hand side shows the absolute magnitude of NSCs and globular clusters as a function of the position of each cluster within their host galaxy, while the right hand side shows the distribution of absolute magnitudes separately for each galaxy, ordered by host stellar mass. From these plots, it is clear that NSCs are nearly always the brightest and most central cluster within their host galaxy.

likely to reside in ([Hong et al., 2019](#)). The suggestion that separate populations may be able to “remember” their initial formation conditions to some extent is expanded upon in [Kamann et al. \(2020\)](#), which suggests that, rather than the binary fraction being affected by interactions, the different populations may have also formed with different intrinsic binary fractions.

1.2 Nuclear Star Clusters

A nuclear star cluster (NSC) is identified as a massive, dense, compact and bright stellar system located at the dynamical centre (or “nucleus”) of its host galaxy ([Neumayer et al., 2020](#)). It’s due to their unusually high brightness and mass that these clusters are easily distinguished, and clearly “stand out”, from their surroundings of typical globular clusters. NSCs are also relatively common objects within galaxies (e.g [Bender et al., 2005](#); [Nguyen et al., 2018](#)) and have been known to co-exist with SMBHs in the centres of galaxies, the closest example being the NSC in our own Milky Way ([Genzel et al., 2005](#); [Feldmeier-Krause et al., 2017](#)). A comparison of globular clusters and NSCs within the Virgo galaxy cluster is shown in Fig. 1.16, which compares brightness to position within host galaxy, on the left panel, and the mass of their host galaxy, on the right panel. This result confirms that NSCs are both the brightest and most central cluster objects in almost all cases ([Böker et al., 2004](#)).

The presence of NSCs raises further questions on cluster formation. For example, when do NSCs form? How do NSCs fall to the centre and resist the displacement caused by merging galaxies? It is reasonable to argue that, given NSCs reside in the dynamical centre of their host galaxies, that NSCs (or at least some form of proto-NSC) could be some of the earliest structures to have formed within the galaxy. Due to the complexity of NSCs, however, detailed studies of the abundances of stars in NSCs, such as done for the Milky Way (Do et al., 2015; Rich et al., 2017), are needed to investigate this.

There are two main theories as to how these large dense structures form within the galactic centre: in situ or by migration. The first is in situ formation, as there is evidence that NSCs may form independently from other globular clusters within their host galaxy by forming directly at the dynamical centre (e.g Loose et al., 1982; Antonini et al., 2015). In this formation scenario, gas is funneled into the galactic centre, which is then able to form stars and massive compact objects, provided enough gas is available. The reason for the gas funneling effect has been proposed to be from a number of different sources, including gas-rich galaxy mergers (Mihos & Hernquist, 1994) and instabilities in the host galaxies internal gas structure (Milosavljević, 2004). The alternative is the migration of formed globular clusters into the galactic centre. A model offered by Tremaine et al. (1975) suggested that compact nuclear structures would form if globular clusters were “dragged”, via dynamical friction, to the centre of the galaxy, which has also been backed up by simulations by Hartmann et al. (2011) and Antonini et al. (2012). The strength of the dynamical friction that a cluster would face is also proportional to the mass of the cluster, which means that the most massive clusters would be more likely to fall to the centre and form an NSC.

There is also evidence that the likelihood of an NSC forming is linked to the mass and morphology of a galaxy. Studies have shown that there is some link between both galaxy mass and the presence of an NSC. In galaxies with masses $\sim 10^9 M_{\odot}$, over 80% contain an NSC, which steadily decreases with mass until the point where almost no NSCs are found in galaxies with a mass of $\sim 10^6 M_{\odot}$ (e.g den Brok et al., 2014; Ordenes-Briceño et al., 2018; Sánchez-Janssen et al., 2019). Both early-type elliptical galaxies and late-type spiral galaxies host NSCs, however, at particularly high masses, ellipticals are considerably less likely to host an NSC (Lauer et al., 2005). The lack of NSCs in high mass ellipticals could be explained by the merging of galactic nuclei with SMBHs, as this would lead to the formation of black holes in binary systems, which would decrease the central density to the point where the NSC would effectively be destroyed (e.g Quinlan & Hernquist, 1997; Milosavljević & Merritt, 2001).

Outside of formation, survival is an important mechanism when discussing NSCs. In the aftermath of galaxy mergers, and after an extended period of time, the remaining

structure of the host galaxy can be stripped away, leaving the nucleus as the only surviving visible entity. Commonly, more massive stripped NSCs (above $\sim 10^6 M_{\odot}$) are referred to as Ultra Compact Dwarf galaxies (UCDs) (Hilker et al., 1999; Drinkwater et al., 2000). Stripped NSCs can be mistaken for typical globular clusters at first glance, however, they share the same features that are used to distinguish NSCs from ordinary globular clusters within their host galaxy: a similar structure to typical globular clusters, but brighter, more massive, and with a more complex population, featuring metallicity and age spreads consistent with the regular infalling of gas to the galactic centre (Dabringhausen et al., 2008; Frank et al., 2011; Neumayer et al., 2020). In the Milky Way, there are thought to be as many as six globular clusters that can be defined as accreted NSCs that have been linked to previous galaxy mergers within the Milky Way’s history (Kruijssen et al., 2019; Pfeffer et al., 2021).

Stripped NSCs may also be prime candidates to host IMBHs (Pfeffer et al., 2021). As these objects are the former nuclei of galaxies, it is reasonable to assume that their original host would have a black hole at the centre, alongside their NSC. In the case of a more massive galaxy, this would likely be a SMBH, however, for a less massive galaxy, this could potentially be an IMBH (see Sec. 1.1.3). During the merging process, it is feasible that a stripped NSC may be able to hold onto the black hole of their original host (Pfeffer & Baumgardt, 2013; Askar et al., 2021). Although there have been no confirmed instances of IMBHs, this retention of black holes mass during accretion has been confirmed by a number of studies of massive ($\sim 10^8 M_{\odot}$) UCDs, including the detection of a $2.1 \times 10^7 M_{\odot}$ SMBH within a UCD in M60 by Seth et al. (2014) (see also Ahn et al., 2017, 2018; Afanasiev et al., 2018). It is important to note that massive black holes have only been detected in massive UCDs to date. It is unclear if less massive stripped NSCs would host a massive black hole, or be able to retain a massive black hole during the accretion process. For simplicity, we will refer to UCDs as stripped NSCs for the remainder of the introduction.

1.3 Omega Centauri

NGC 5139, Omega Centauri (ω Cen), is a particularly important and interesting object in the Milky Way. Located in the Centaurus constellation in the southern hemisphere ~ 5 kpc from the Sun, it is the most massive cluster in the Milky Way other than the Milky Way NSC at $3.94 \pm 0.02 \times 10^6 M_{\odot}$ (Baumgardt & Hilker, 2018).

There is a longstanding debate as to the classification of ω Cen, either as a genuine globular cluster or a stripped NSC (e.g Bekki & Freeman, 2003; Pfeffer et al., 2021) though, if ω Cen is in fact a stripped NSC, there is still no consensus on whether it

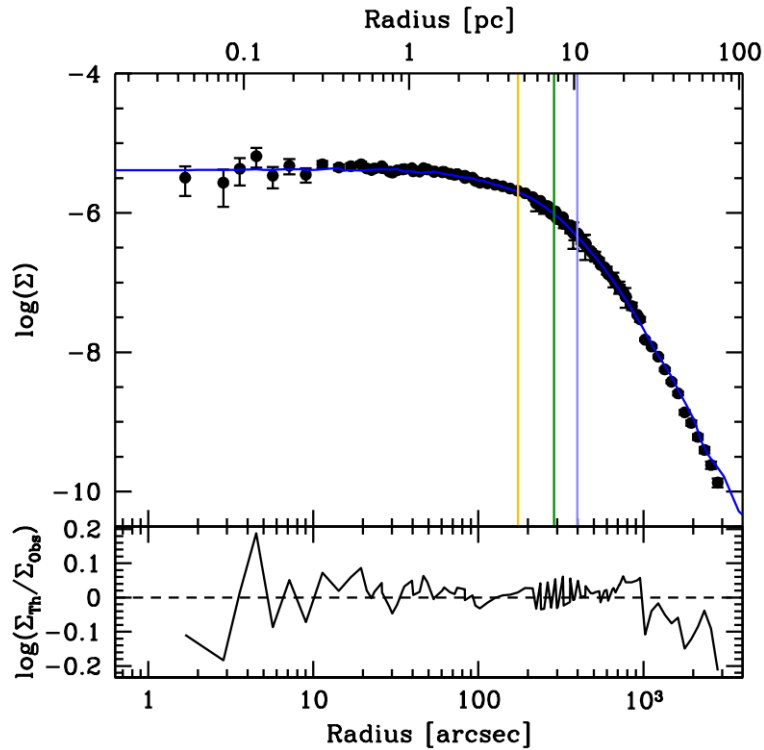


FIGURE 1.17: The surface brightness profile of ω Cen from Baumgardt & Hilker (2018), which shows the profile flatten within the core radius. The yellow line represents the core radius, the green represents the half light radius and the blue represents the half mass radius. This is evidence that the cluster is not core collapsed, and likely hosts a considerable black hole mass.

belonged to either the Gaia-Enceladus or the Sequoia dwarf galaxies (Massari et al., 2019a; Forbes, 2020; Pfeffer et al., 2021). The unusual complexity of ω Cen, however, supports its classification as a stripped NSC, as the cluster: shows complex kinematics and internal dynamics (van de Ven et al., 2006), has a particularly complex chemical composition (Alvarez Garay et al., 2024), and dynamical models have shown that the morphology and kinematics can only be explained by either an IMBH or large population of stellar mass black holes (or a combination of the two, discussed below).

Dynamically, ω Cen is classed as young. As seen in Fig. 1.4, ω Cen has a particularly long relaxation time at $\sim 10^{10}$ years. The surface brightness profile of the cluster in Fig. 1.17 is flattened towards the cluster centre, which shows that ω Cen is not core collapsed, which is further evidence for substantial black hole content in the cluster. ω Cen also shows limited mass segregation, as shown by the flat distributions in the mass profiles for each cluster region in Fig. 1.18.

Due to the cluster's status as a potential former NSC, and to the fact that the cluster is not core collapsed, there is a long standing debate as to whether the cluster hosts an IMBH, or a collection of stellar mass black holes at the cluster centre. There have previously been claims of IMBH detections, including suggestions of a $40000 M_{\odot}$ IMBH

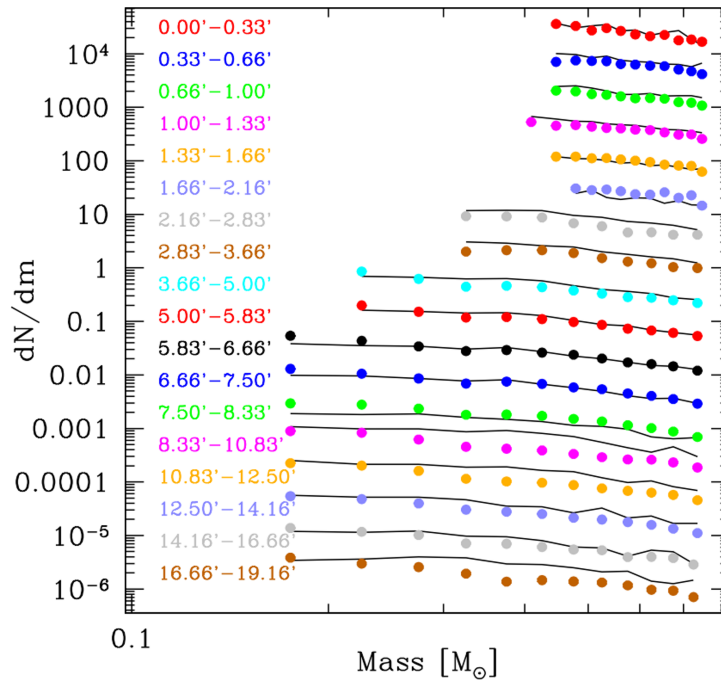


FIGURE 1.18: Similar to Fig. 1.5, this figure shows the stellar mass function of ω Cen with different projected distances to the cluster centre, taken from Baumgardt & Hilker (2018). The distributions within each of the cluster regions are flat, which suggests little mass segregation within the cluster.

at the centre of ω Cen based on its velocity dispersion and surface brightness profile (Noyola et al., 2008). These claims have been investigated by a number of studies since then, such as a study by van der Marel & Anderson (2010a), which found the upper limit of an IMBH to be $10000 M_{\odot}$. Other studies have also reported that ω Cen can be successfully modelled without an IMBH. A study by Zocchi et al. (2019), for example, was able to model the velocity dispersion of ω Cen with a concentrated central cluster of stellar mass black holes rather than a central IMBH. The comparison between models and observations in a study by Baumgardt et al. (2019) is shown in Fig. 1.19, which shows the proper motion and line of sight velocity dispersion of the cluster and N-body models with different assumptions; an IMBH and a low and high retention of stellar mass black holes, as the retention fraction of stellar-mass black holes in ω Cen is debated (see van der Marel & Anderson, 2010b; Noyola et al., 2010). The conclusion from Baumgardt et al. that if ω Cen does contain an IMBH, its mass would be significantly less than the $40000 M_{\odot}$, and suggested that the black hole content of ω Cen may be a combination of both a lower black hole retention fraction and a lower mass IMBH, though this would require further study.

A recent breakthrough has been made by a study by Häberle et al. (2024), which has made a convincing case for an IMBH presence by observing seven fast moving stars within the central region of the cluster. Shown in Fig. 1.20 is the observed velocity

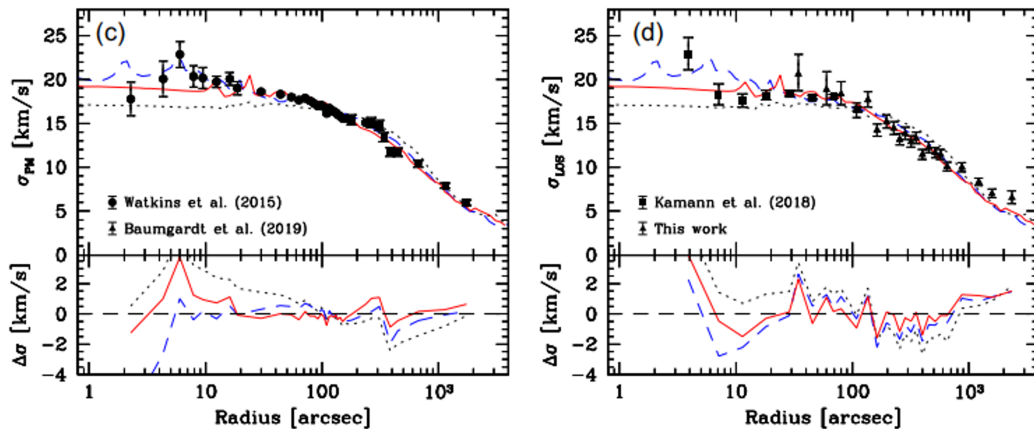


FIGURE 1.19: A comparison of observations (black points) to a number of models for the black hole content of ω Cen taken from Baumgardt et al. (2019). The black dotted line represents a 10% stellar mass black hole retention fraction, the red solid line a 75% retention fraction, and the blue dashed line represents a single $47\,500 M_{\odot}$ IMBH. The left panel shows the proper motion velocity dispersion and the right panel shows the line of sight velocity dispersion

distribution is compared to both a model with no IMBH and a model with a massive IMBH and, as seen, a number of observed stars have a velocity significantly larger than the 62 km s^{-1} escape velocity of ω Cen. This is in contrary to the no IMBH model, which is shown to have no stars with velocities higher than ω Cen's escape velocity. This means that these observations can only be explained by the stars being bound to a massive black hole. The study was also able to determine that the most likely mass for the black hole is $\sim 40\,000 M_{\odot}$, with a lower mass limit of $\sim 8\,200 M_{\odot}$, which provides compelling evidence for a IMBH presence.

Another unusual feature of ω Cen is the multiple populations in the cluster. ω Cen is classed as a Type II cluster and shows not only numerous additional populations, but also a wide spread in metallicity. The chromosome map of ω Cen from Milone et al. (2017) is shown in Fig. 1.21 and highlights the complexity of the cluster, with the traditional 1P and 2P stars shown in black and the additional populations observed in Type II clusters shown in red. This complexity is also shown in the cluster's main sequence, which is shown in Fig. 1.22 from Bellini et al. (2017). To date, at least 15 chemically distinct populations have been detected in ω Cen, which only raises more questions as to how the multitude of populations formed and evolved.

One of the key pieces of information missing about ω Cen is a well defined binary fraction. Determining the binary fraction of a cluster as complex as ω Cen will provide a crucial insight into the evolution of the cluster, which is particularly important given its status as a stripped NSC. The binary fraction can also give a better understanding on the black hole content of the cluster, which is important given the potential for the

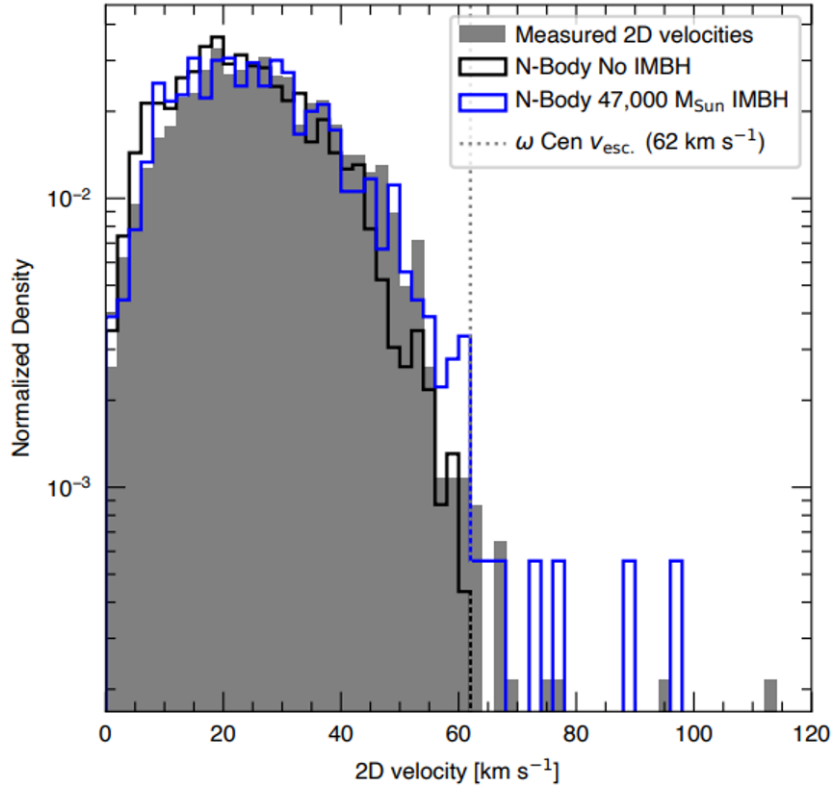


FIGURE 1.20: The observed stellar velocity distribution of ω Cen (grey) compared to two N-body models: a model with no IMBH (black) and a model with a $47\,000 M_{\odot}$ IMBH (blue) from Häberle et al. (2024). A number of stars are observed with a velocity significantly higher than the escape velocity of the cluster, which can only be explained by the presence of a massive black hole.

cluster to host an IMBH. Studies of multiple populations can also benefit from a well defined binary fraction, as binarity in multiple populations of Type II clusters is not well studied. To date, there have been a scarce few studies of the binary fraction of ω Cen and, of the very few direct investigations for binary systems in ω Cen, no studies that give a well measured value for the global fraction of the cluster. The most recently published estimates for binary fraction are photometric studies by Bellini et al. (2017), which estimates a fraction of $2.70 \pm 0.08\%$, and one by Elson et al. (1995), which estimates an upper limit of 5%. Dark remnants have also been recently detected by a study by Platais et al. (2024), which was able to successfully identify four cluster members that have acceleration patterns consistent with the gravitational pull of an invisible companion, such as white dwarfs, one of which is massive enough to be classed as a neutron star.

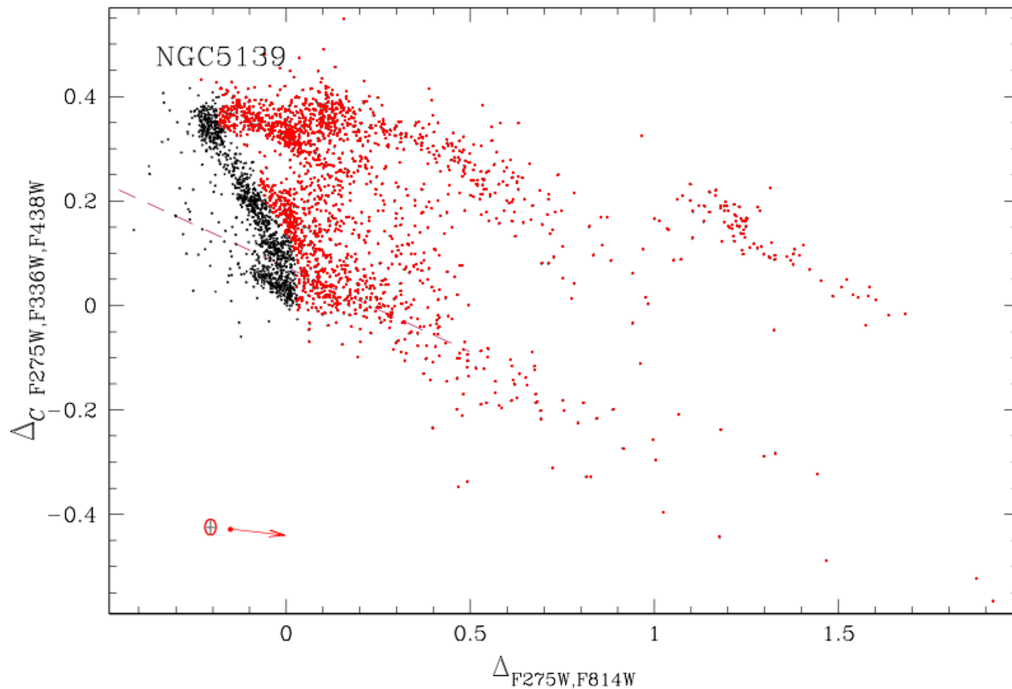


FIGURE 1.21: The chromosome map of ω Cen taken from Milone et al. (2017), which shows the traditional 1P and 2P population in black and the additional Type II cluster features in red. From the chromosome map, we see a number of additional populations and the characteristic spread in metallicity of a Type II cluster.

1.4 Observational techniques

1.4.1 Photometry vs. spectroscopy

Detecting stars in binaries poses a number of difficulties, particularly in globular clusters. The two most widely used and efficient methods are through photometry and through spectroscopy.

There are a number of different methods for detecting binaries photometrically. Multi epoch photometry, which traces the flux of one star, allows for the dip in brightness that may be caused by an eclipsing binary companion. Astrometric wobble is also used, in which a star is monitored for small but regular displacements in a star's relative position. The most commonly used method for photometrically detecting binaries in globular clusters, however, is based on the principle that, when observing an unresolved binary system (typical for tight binaries in distant globular clusters) made of two luminous stars (rather than stellar remnants), both the primary and the companion will contribute to the total brightness of the observed primary star. This has the effect of giving the primary star a different position in the CMD to that of a single star, with the severity of the difference dependent on the mass ratio of the secondary compared to the

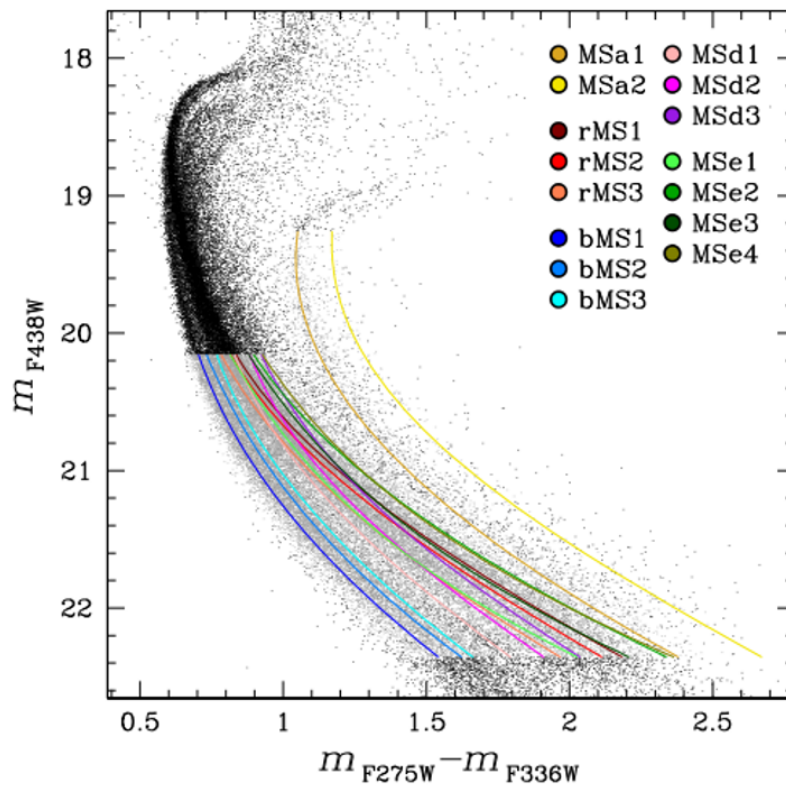


FIGURE 1.22: The main sequence portion of the CMD of ω Cen taken from [Bellini et al. \(2017\)](#) marked with separately identified populations. In total, there are at least 15 chemically distinct populations, which highlights the complexity of the cluster.

primary. For example, although an equal mass binary system will have the same colour, the observed star will be ~ -0.7 magnitudes brighter than if the star had no companion. This shifting in the main sequence forms a distinct branch along the main sequence that is often referred to as the binary main sequence. An example of a CMD with tracks to show the binary main sequence for different mass ratios is shown in Fig. 1.23. This CMD shows that a higher mass ratio results in a more separated and distinct binary main sequence region than lower mass ratio bands. A number of studies have successfully reported photometric binary fractions using a photometric approach, including the study of 59 galactic globular clusters by [Milone et al. \(2012b\)](#) and the study of binary systems in open star clusters such as [Cordoni et al. \(2023\)](#) and [Mohandasan et al. \(2024\)](#). Despite the success of previous studies, Fig. 1.23 also highlights a number of drawbacks to the photometric method.

The first is that, although the photometric approach allows for the estimation of the mass ratio of the system, it does not allow for the determination of orbital parameters such as orbital period or eccentricity, hence it offers a limited study into the demographics of the population. Secondly, as seen from the separation of the different mass ratios in Fig. 1.23, this method is less sensitive to binaries with a low mass ratio. Although the

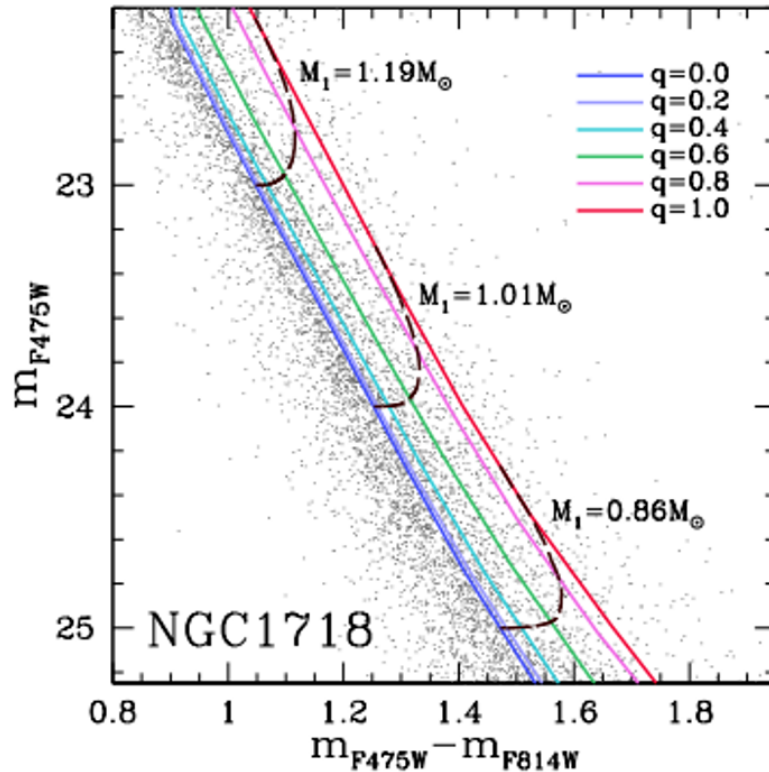


FIGURE 1.23: The CMD of the open star cluster NGC 1718 taken from Mohandasan et al. (2024) with coloured lines as a reference for binary systems with a variety of mass ratios (q). The black dash lines show the location on each track for primary stars of different masses.

separation is clear for binaries with mass ratios $\gtrsim 0.6$, binaries with mass ratios less than this are easily obscured by the CMD. Thirdly, this approach can also be affected by multiple populations. As seen in Fig. 1.14, multiple populations in exceptional cases can result in a secondary branch of the main sequence which is indistinguishable from a binary main sequence branch. This is particularly important in the case of ω Cen where, as seen in Fig. 1.22, the multiple populations of the cluster form a number of separate main sequence branches which makes estimating a photometric binary fraction particularly challenging.

This study uses the spectroscopic approach to detecting binary systems. The spectroscopic approach is based on the concept that, as the primary star will move due its binary counterpart, the observed star's spectrum will experience a Doppler shift proportional to the radial velocity of the star:

$$\Delta\lambda = \lambda_{\text{obs}} - \lambda_0 = \lambda_0 \frac{v}{c} \quad (1.3)$$

Where λ_0 is the actual wavelength of the source (if it were not moving), λ_{obs} is the observed wavelength and v is the stars radial velocity.

Using the magnitude of the shifts in spectra, it is then possible to calculate the orbital velocity of the primary star given the actual wavelength, λ_0 , is known. By taking a number of measurements, it is then possible to detect velocity measurements to detect significant velocity variation around the mean system velocity. An example of radial velocity measurements of a star in ω Cen that has been identified as a binary system, based on the work that will be presented in this thesis, is shown in Fig. 1.24. In this example, the radial velocities vary with each measurement and a clear variation around the mean system velocity can be seen (the systemic velocity of ω Cen is indeed $\sim 250 \text{ km s}^{-1}$). This method will also be discussed further in Sec. 2.4. This technique has a long history of success, with some of the first studies using this method dating to the 70's (e.g [Gunn & Griffin, 1979](#)). More recent studies that have used the spectroscopic approach to detect binary systems in star cluster environments include the study of NGC 3201 by [Giesers et al. \(2019\)](#), the study of NGC 1850 by [Saracino et al. \(2023\)](#) and the study of M4 by [Sommariva et al. \(2009\)](#). There are a number of advantages to using a spectroscopic approach as opposed to the photometric approach. One benefit is that this method can be used to provide further details into individual binary systems through the estimation of orbital parameters, including velocity amplitude, eccentricity, mass ratio and orbital period, rather than just the mass ratio derived from photometry (see Sec. 6.2). By estimating orbital parameters for binary systems within cluster environments, it is then possible to identify any trends within the binary population, which may provide a link to the properties of the host cluster, such as the clusters formation, evolution, and black hole content. This also enables a binary search in clusters where multiple populations are visible on the CMD as, unlike photometry, the detection of binary system is not reliant on the star's position on the CMD. Another advantage is that this is also sensitive to binary systems with dark components, such as white dwarfs, neutron stars and black holes.

There are still, however, some drawbacks to the spectroscopic approach that much be considered. This method is not sensitive to binary systems with particularly long orbital periods and low mass ratios, as in these cases the companion star has little observable effect on the primary star. This effect will be discussed further in Sec. 1.4.2. This method also relies on multi-epoch data in order to detect velocity variations, which requires more observation time.

1.4.2 Using velocity variations to identify binary systems

As discussed in Sec. 1.4.1, the spectroscopic approach adopted in this study relies on detecting velocity variations from the spectrum of the observed primary star that are caused by a binary companion. This means that the orbital properties of the binary

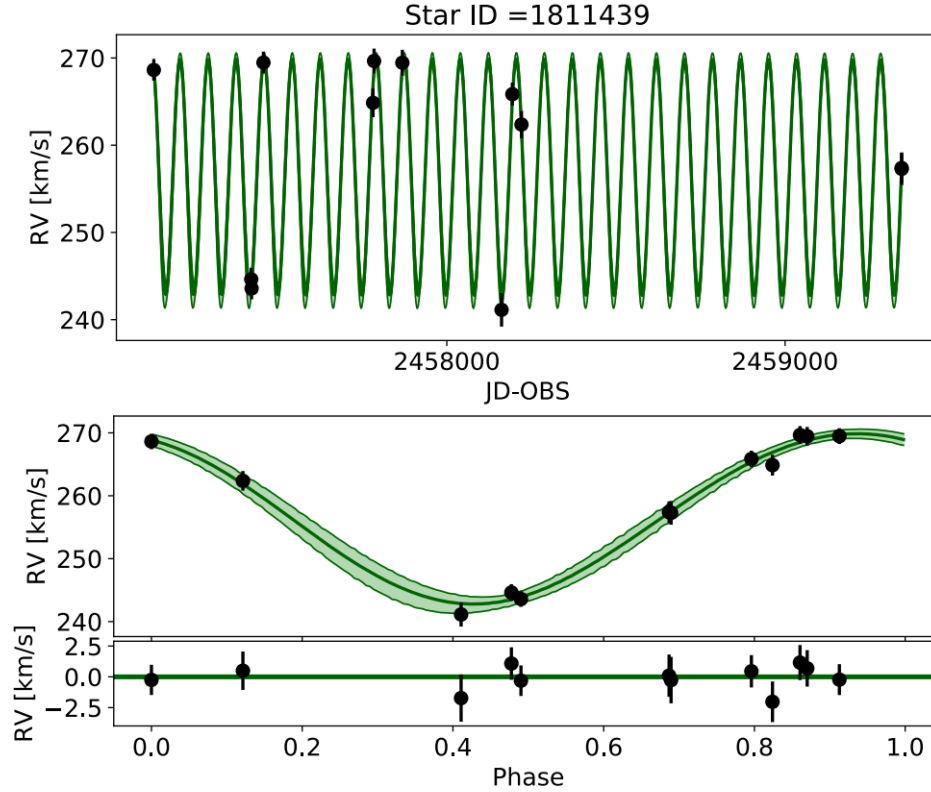


FIGURE 1.24: The radial velocity measurements for a binary system in ω Cen derived from the star's spectrum overlaid with the best fitting orbit from Saracino et al. (in prep.). The top panel shows the radial velocity measurements and best fitting orbit against the observation date, while the bottom panel shows the relative position of each radial velocity measurement within the fitted orbit.

system, in particular the orbital period, mass ratio, eccentricity and inclination, will have an impact on the system's velocity measurement. For this, consider a test binary system where: each star has the same mass, the orbital period is 10 days, the orbit is completely circular ($e = 0$), the inclination angle is 90° (discussed in this section), and the mean system velocity is set to be 250 km s^{-1} . For this test system, by varying each of these parameters, it is possible to see the effects of the orbital parameters on the detection of a binary system. The velocity measurements for the test binary system are calculated based on the principle of Kepler's third law, which can be rearranged to calculate individual velocity measurements, given by:

$$v_{r,1}(t) = v_0 + K_1 [e \cos(\omega) + \cos(T(t) + \omega)] \quad \text{where} \quad K_1 = M_2 \sqrt{\frac{G}{a(M_1 + M_2)(1 - e^2)}} \sin(i) \quad (1.4)$$

Where $v_{r,1}(t)$ is the measured velocity for each time step, v_0 is the barycentric system velocity, K_1 is the velocity amplitude, e is the system eccentricity, ω is the argument of periapsis (orientation of the eccentric system), a is the semi-major axis, M_1 and

M_2 are the primary and secondary mass respectively, and i is the inclination of the system. $T(t)$ represents the true anomaly of the system, which is a coefficient calculated for each system which is dependent on the system eccentricity and orientation (Lovis & Fischer, 2010). This equation is used to create all of the velocity curves shown in Figs. 1.25, 1.26, 1.27 and 1.28. This equation is also used to generate the mock data sample in Sec. 3.2

The first orbital parameter that will be discussed is the orbital period of the system. There are two major effects that increasing the orbital period has on the velocity curve: a lower velocity amplitude, and the elongation of the wave shape compared to shorter orbital periods. This is seen in Fig. 1.25, which shows the test binary over a range of orbital period values, 5, 10, 20 and 40 days. For the 5 day orbit, the velocity amplitude is $\sim 80 \text{ kms}^{-1}$, compared to the amplitude of $\sim 40 \text{ kms}^{-1}$ for the 40 day orbit. The elongation and, in turn, frequency of the orbit is also visible, as there are a total of 4 orbits visible within the observed range for the 5 day orbit, while only a 0.5 orbits are seen for the 40 day orbit. This results in a much less significant variation of orbital velocity for the longer period orbit compared to the shorter period orbit. Due to the higher velocity amplitude, the more frequent instance of the peak velocity, and the more significant variation in velocity within the observation period, it is more likely that a binary system with a shorter orbital period would be detected rather than a longer orbital period.

The mass of the companion compared to the primary, mass ratio, has an impact on the velocity measurements of the primary. The test binary is shown in Fig. 1.26 with varying mass ratio, between $M_2/M_1 = 0.1$ and $M_2/M_1 = 1$. From this, we see that the main effect of a low mass ratio is the lowering of the velocity amplitude. In the case that the primary and secondary have an approximately equal mass, each star exerts a comparable gravitational force on the other. This means that the primary star will have significant variations in velocity as it moves due to its companion, which is seen as the system has a maximum velocity amplitude of $\sim 80 \text{ kms}^{-1}$ for equal mass stars. This significantly decreases to $\sim 10 \text{ kms}^{-1}$ for a 0.1 mass ratio, as the companion has a negligible gravitational force compared to the primary. Due to the significantly reduced velocity amplitude, a system with a very low mass ratio is less likely to be classified as a binary. There are some observational effects that limit the detection of systems with equal mass stars, however this will be discussed in Sec. 3.2.

Despite having a significant effect on the observed radial velocity, eccentricity is unusual in the sense that it is the sinusoidal shape of the velocity curve that is impacted by increasing eccentricity, along with the velocity amplitude. Shown in Fig. 1.27 is the velocity curve for the test system with eccentricity values between $e = 0$ and $e = 0.9$,

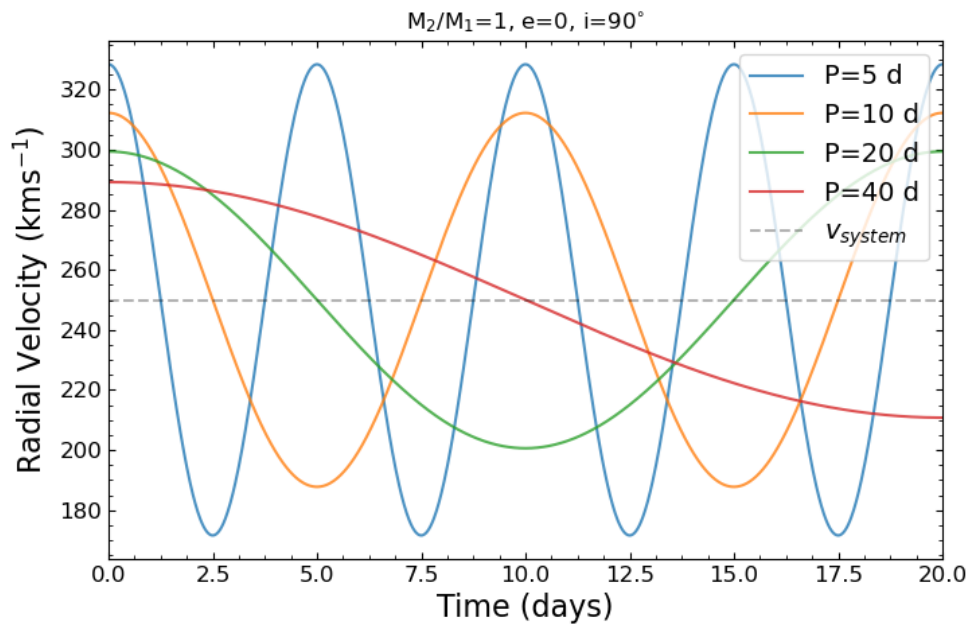


FIGURE 1.25: The radial velocity of a test star against time for a range of set values for orbital period, between 5 and 40 days. This shows the effect of a orbital period on the velocity curve of a binary system, as the velocity amplitude decreases, and the velocity variations happen over a more extended period of time, both of which make confidently identifying binary systems more challenging.

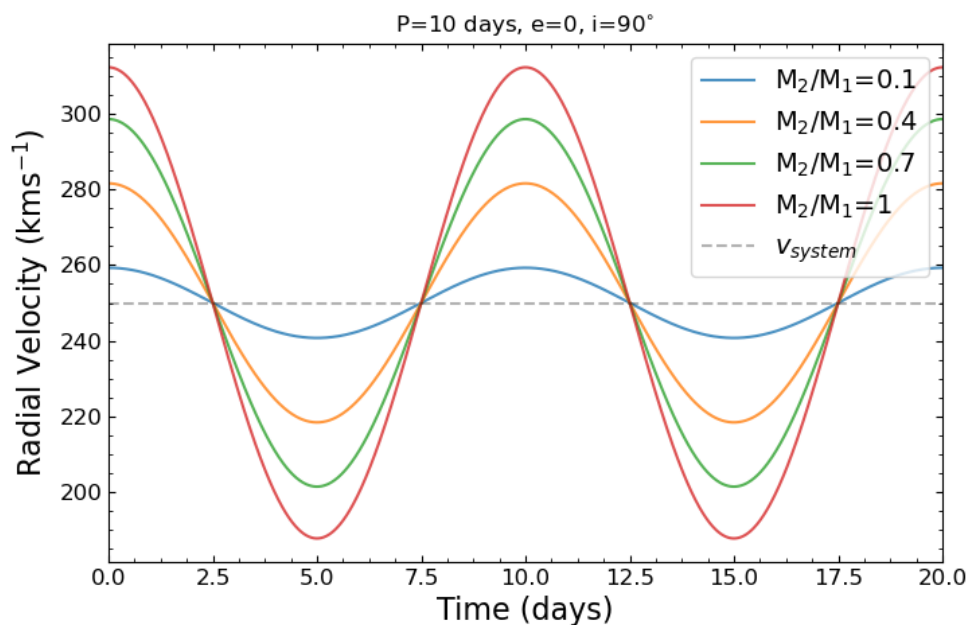


FIGURE 1.26: The radial velocity of the test binary with respect to time, with varying mass ratios. A smaller mass ratio results in the velocity amplitude of the system being significantly reduced, which reduces the likelihood of the star being classed as a binary system.

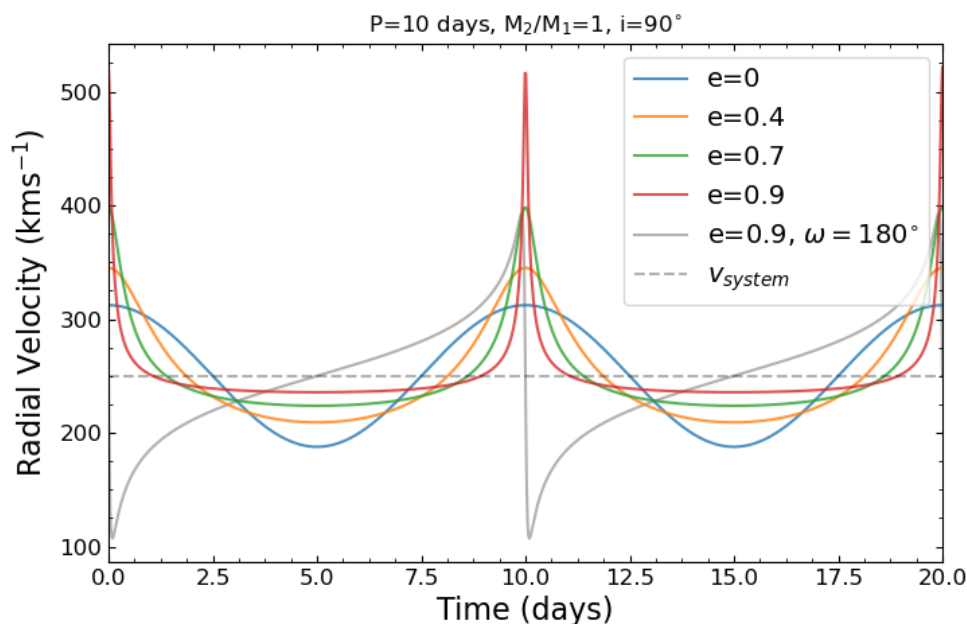


FIGURE 1.27: Radial velocity over time of the test binary system with a varied eccentricity, between 0 and 0.9. The eccentricity has an unusual effect on the velocity curve, as the curve becomes deformed, rather than sinusoidal. Increasing eccentricity, therefore, makes detection more difficult, as it relies on observing the system when the velocity variation is maximised.

which highlights this effect. In the case where $e = 0$, the companion orbits in a circular path, which leads to a sinusoidal velocity curve with a consistent velocity amplitude of $\sim 80 \text{ km s}^{-1}$. In the case of high eccentricity systems, such as $e = 0.9$, the companion orbits in an oval shaped path, which leads to the velocity curve becoming deformed. This is due to the effects of Kepler's Second Law, which states that a the orbit of a binary companion will sweep out equal areas at equal intervals of time, and so a closer distance between the two stars implies a higher orbital velocity. This makes detecting these systems more challenging, as it relies on observing the star as it moves closest to the primary to detect the largest variations, which in this case in the range of ~ 2 days. The shape of the radial velocity curve for an elliptical system is also dependent on the orientation of the system (referred to as argument of periapsis, ω , or mean anomaly), as shown by the solid grey line in Fig. 1.27.

Although inclination is a geometric effect rather than an orbital property, the inclination of a binary system has a significant impact on the measurement of radial velocities. Shown in Fig. 1.28 is the test binary with varying inclination angles which shows the effect of the system geometry. For example, when the system is edge on ($i = 90^\circ$) and the plane of the orbit is in line with the observer, the full shift of the spectrum, and therefore the maximum velocity amplitude, can be observed as the star moves toward and away from the observer. When the binary system is face on ($i = 0^\circ$) and the plane of the

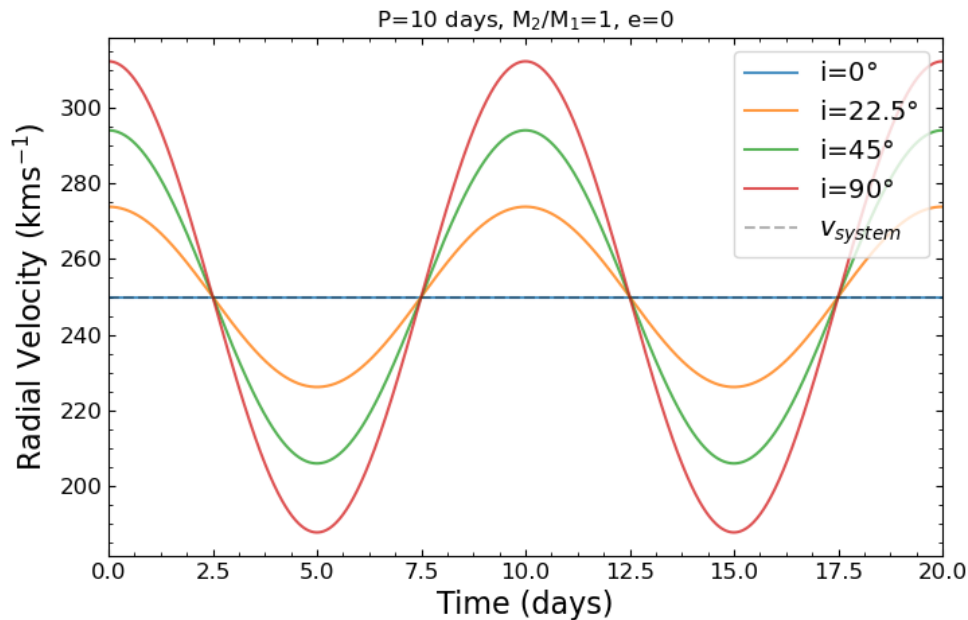


FIGURE 1.28: The radial velocity against time of the test binary with varying inclination angles. As the inclination angle approaches 0° (face on), the plane of orbit is perpendicular to the observer and the velocity curve becomes a line following the system mean velocity as the Doppler shift of the spectrum is not observable. As the inclination approaches 90° (edge on), the plane of orbit is parallel to the observer and the maximum velocity variation of the system is measured as the full shift of the spectrum is observable.

orbit is perpendicular to the observer, the velocity curve will be a flat line at the system velocity as, even though the star is moving, it is not possible to observe any shift in the spectrum, as the motion of the star is not in the plane of the observer. Both the mass ratio and the inclination have the same effect on the velocity curve, namely a reduction in the velocity amplitude. Hence, the two quantities are impossible to disentangle without further information and typically, only the minimum mass, $M_2 \sin(i)$, can be determined for any companion.

1.5 MUSE

The Multi Unit Spectroscopic Explorer (MUSE) (Bacon et al., 2010) is an integral field spectrograph (IFS) mounted on Yepun (UT4) at the Very Large Telescope (VLT) at the Paranal observatory in Chile of the European Southern Observatory (ESO). The project kick-off was in 2005, and then observed first light in 2014. The instrument has a wavelength range of 465-930 nm and two observing modes, Wide Field Mode (WFM) and Narrow Field Mode (NFM), which both use adaptive optics (AO) to improve resolution. The WFM has a $1' \times 1'$ field of view (FoV) and uses ground level AO (GLAO), which

results in an improved spatial resolution and a sampling of $0.2''$ per pixel. The NFM has a $7.5'' \times 7.5''$ FoV and uses more advanced laser tomography AO (LTAO), which greatly improves resolution, with a higher sampling of $0.025''$ per pixel. Although this improved sampling and resolution makes NFM ideal for studying dense stellar environments, such as the central regions of star clusters, the higher resolution limits the NFM FoV.

MUSE is classed as an integral field spectrograph (IFS), which is built around 24 separate integral field units (IFUs). An IFS allows for the observation of the entirety of an astronomical object, with each pixel being measured for the intensity of light as a function of wavelength. This results in a 3D data cube of the object: a 2D field of view plus a third dimension, which is the full spectrum of each pixel. Data from MUSE is routinely used to study a number of different objects including, but not limited to: globular clusters, high- z galaxies, ultra faint dwarf galaxies and Lyman α emissions (Bacon et al., 2023).

This study makes use of the Galactic Globular Cluster Survey (PI: S. Kamann), which has observed 27 Galactic globular clusters since first light in 2014 (Kamann et al., 2018). Observing dense stellar systems like globular clusters is challenging due to the crowded field, which causes multiple stars to blend together on the detector. Although there have been some previous photometric studies with HST, previous spectroscopic surveys of individual stars within globular clusters have been seriously limited by crowding, particularly in the cluster centre. Spectroscopy is limited as it does not preserve spatial information, and so the spectra of different stars cannot be de-blended. IFSs such as MUSE, however, are able to preserve spatial information, and therefore can de-blend individual spectra within the sample (Kamann et al., 2013). As discussed in Sec. 1.4.1, a large number of epochs is necessary for spectroscopically detecting variable stars and calculating a constrained binary fraction, which had also not been available before MUSE. There have been a number of studies of globular clusters using MUSE, which have been able to give important insights into the dynamics and demographics of globular clusters. These include the study of NGC 3201 by Giesers et al. (2019), the detection of a stellar mass black hole (Giesers et al., 2018), and the study of multiple populations within the cluster (Kamann et al., 2020). There has also been a study of the intermediate age LMC cluster NGC 1850 by Saracino et al. (2023), which has discovered an unusual object within the cluster that is debated to either be a stellar mass black hole (Saracino et al., 2022) or a post-interaction binary system (El-Badry & Burdge, 2022). There have also been a number of studies conducted for ω Cen, including a study by Pechetti et al. (2024) which investigated the location and kinematics of the cluster centre, as the location of the cluster centre is still uncertain.

1.6 Aims of this work

In this first of its kind study of ω Cen, the aim is identify, and then to study the demographics of binary systems within the massive globular cluster ω Cen. Due to the density of the cluster centre, the limited spectroscopic surveys of the past and the complications with photometry of multiple population branches obscuring the binary main sequence branch of the CMD, it has not been possible to calculate a well constrained value for the binary fraction of the cluster until now. Using MUSE, this analysis is now possible not only thanks to the large number of stars in the sample.

The first aim is to calculate a binary fraction, corrected for observational biases. As discussed in Sec. 1.1.4 and Sec. 1.3, binary stars, and a well constrained binary fraction, is vital to our understanding of the formation and evolution of globular clusters and can provide a key insight into other areas of globular cluster study, such as the number and masses of black hole. This is particularly pertinent for ω Cen, due to its status as a proposed stripped NSC and potential to host an IMBH. As well as providing a fundamental property of ω Cen to compare to other globular clusters in the Milky Way, a well constrained binary fraction has applications in simulations of cluster formation particularly as a standard to compare to. Beyond this, it is possible to calculate a corrected binary fraction for all areas of the CMD. By comparing the binary fractions for regions of the CMD, it will be possible to determine if any groups within ω Cen are intrinsically more likely to be in binary systems, such as BSSs that were discussed in Sec. 1.1.4.1.

The second aim is to then identify trends in binarity across the multiple populations of ω Cen. As discussed in Sec. 1.1.5 and Sec. 1.3, the topic of multiple populations is particularly active and hotly debated. In the case of ω Cen, this is particularly important due to the large number of chemically distinct populations. By determining the binary populations across the different populations of ω Cen and identifying any trends, this can provide an important insight into the formation and evolution of the multiple populations. Identifying trends in multiple populations can also provide more insights into the structure of multiple populations in other Type II clusters, which to date are relatively poorly understood.

The structure of the following work is as follows: Chapter 2 details the process of reducing the MUSE data, removing known photometric variables and calculating the probability that a star is variable. In Chapter 3, the process of generating a sample of mock MUSE data is discussed, including the physical principles that are considered, the method for calculating the mock sample, and the observational effects that are applied. After the mock sample is generated, it is then used to determine the necessary cuts on

the number of epochs to apply to the observed data and to give a reasonable threshold over which a star is considered binary. Chapter 4 then combines the results of Chapter 3 and the variability calculations from Chapter 2 to calculate and discuss both a discovery fraction and a completeness corrected binary fraction for each region of the CMD. The analysis of multiple population binarity is then discussed in Chapter 5 and the cluster is split into a number of distinct populations based on the distribution of chemical abundance within the cluster. Chapter 6 consolidates the main results of this study, and provides a discussion on the future work and the applications of these results.

A number of the data processing steps were not completed by the author, Florence Wragg. The initial observations (Sec. 2.1.1) were completed through the relevant survey team (Kamann et al., 2018). The data reduction stages (Sec. 2.1.2) were processed through the MUSE pipeline (Weilbacher et al., 2020). The spectral extraction, spectral analysis, CMD region separation and final sample cleaning cuts were completed by Sebastian Kamann and Tim-Oliver Husser (Sec. 2.2 Kamann et al., 2013; Husser et al., 2016). The pseudo colours (Sec. 5.1) were calculated by Husser et al. (2020) based on work by Milone et al. (2017). All work, other than the steps declared above, was completed by Florence Wragg. Throughout this thesis, the use of “we” refers to the study as a whole rather than a collection of authors.

Chapter 2

Detecting Variability

“It is the struggle itself that is most important. We must strive to be more than we are. It does not matter that we will never reach our ultimate goal. The effort yields its own rewards”

Lt. Cmdr. Data - *Star Trek: The Next Generation*

2.1 MUSE data

2.1.1 Observations

One of the biggest challenges in spectroscopic observations of globular clusters is the crowding of the field, resulting in the blending of sources. As a consequence, spectroscopic samples large enough to determine the demographics of the binary populations in clusters like ω Cen are still scarce. This is now possible with the Multi Unit Spectroscopic Explorer (MUSE, [Bacon et al., 2010](#)) at the Very Large Telescope (VLT). MUSE saw first light in 2014 and since has observed 27 globular clusters within the Milky Way, including ω Cen, as part of the guaranteed time observations (GTO, see [Kamann et al., 2018](#), for an overview of the observations). In the crowded cluster fields, MUSE enables simultaneous spectroscopy of thousands of stars.

For this study, we use all the MUSE GTO data available of ω Cen: 10 wide field mode (WFM) pointings with a $1' \times 1'$ field of view (FoV), and 6 narrow field mode (NFM) pointings with a $7.5'' \times 7.5''$ FoV were observed repeatedly between 2015 and 2022. On average, each WFM pointing was observed for 15 epochs, whereas each NFM pointing was only observed twice. However, the footprints of the NFM pointings are fully covered by the central WFM pointings as well. For the WFM data, cadences between epochs ranged from less than 1 h to several months. All observations were performed using the nominal wavelength range, covering 4750 to 9350 Å with a spectral resolution of $R \sim 1800 - 3500$. A visual representation of the WFM data available for ω Cen from MUSE is shown in [Fig. 2.1](#).

As can be seen from [Fig. 2.1](#), the GTO survey targets different areas in the central region of the cluster. We note that the data discussed in this work form part of the OMEGACAT project, recently presented in [Nitschai et al. \(2023\)](#). However, whereas the catalog published by [Nitschai et al.](#) contains the results obtained by averaging over the individual epochs, here we focus on the single-epoch data and study the stars for radial velocity variations between the individual epochs.

2.1.2 Data reduction

All observed data was processed with the standard MUSE pipeline ([Weilbacher et al., 2020](#)), which performs all the steps necessary to reduce integral-field spectroscopic data. Following bias subtraction, signal tracing, flat fielding, and wavelength calibration, the data from each of the 24 spectrographs are stored in a pixtable. In the next step, the data from the 24 pixtables are combined, corrected for differential atmospheric

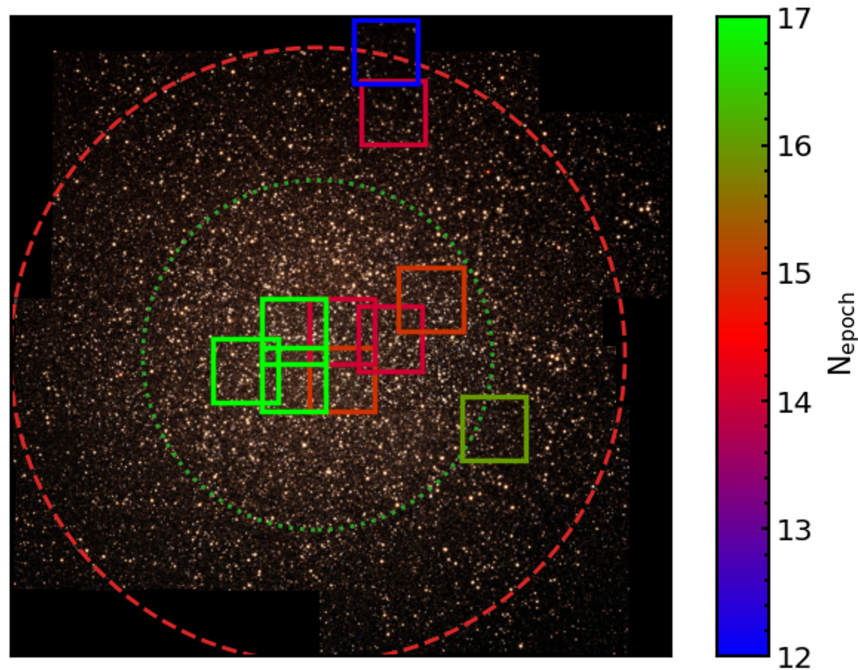


FIGURE 2.1: A mosaic of ω Cen from Nitschai et al. (2023), overlaid with the 10 WFM ($1'$ across) pointings of ω Cen as observed by MUSE (Kamann et al., 2018), with the number of epochs for each pointing shown via the colourbar. The 6 NFM ($7.5''$ across) pointings are not shown as they would be too small to see, but are in the overlap region of the four central WFM pointings. The green dotted circle represents the clusters core radius, and the red dashed circle shows the half light radius. In this image, up is north and left is east.

refraction, and flux calibrated. As outlined in Husser et al. (2016), we do not perform a sky subtraction nor a correction for telluric absorption. These features are corrected for during the post-processing steps described below. This process is repeated for every individual exposure before the data for the three (or four, in the case of NFM data) exposures per pointing and epoch are combined and resampled onto a final data cube, showing the RA and Dec coordinates along the spatial dimensions and the wavelength along the spectral dimension. We note that we do not investigate variability between the individual exposures entering a data cube. These exposures were usually taken back-to-back, with time offsets of a few to a maximum of 30 minutes.

2.2 Spectral analysis

2.2.1 Spectral extraction

The extraction of individual spectra is done using the PAMPELMUSE software, an algorithm designed to simultaneously deblend the spectra of multiple stars within a single

datacube, detailed in [Kamann et al. \(2013\)](#). In order to properly perform the extraction, the MUSE data must first be matched to an astrometric reference catalog, in order to obtain relative positions and brightness estimates for the stars in the field of view. For the central fields, we used the *Hubble* space telescope (HST) photometric catalog from the ACS survey of Galactic globular clusters ([Sarajedini et al., 2007](#); [Anderson et al., 2008](#)). MUSE pointings that were not completely covered by the footprint of the ACS survey were instead processed with the HST catalog published by [Anderson & van der Marel \(2010\)](#).

The analysis with PAMPELMUSE starts with an initial guess of the point spread function (PSF), modelled as a Moffat profile, which is iteratively improved using the brightest and most isolated stars in the sample. Within each iteration, the contributions from other nearby stars are subtracted using the PSF model. The iterative process is then repeated on each layer of the datacube and each solution is combined to create a wavelength dependent PSF model and to predict the position of each source as a function of wavelength. Finally, this wavelength dependent model is used to build the final spectrum for each source by extracting the flux from each layer of the datacube.

2.2.2 Spectral analysis

The analysis of the spectra is performed with SPEXXY ([Husser et al., 2016](#)), which performs full-spectrum fitting against a library of template spectra in order to measure stellar parameters and radial velocities. In order to obtain initial guesses for the former, the photometry of the stars with extracted spectra is compared to an isochrone from the PARSEC database ([Bressan et al., 2012](#)), which assumes a distance of 5.3 kpc, extinction of $A_V = 0.4$, an age of 13.5 Gyr and a metallicity of -1.2. Using a nearest-neighbour approach, each star is assigned an initial value for effective temperature (T_{eff}), surface gravity ($\log(g)$) and metallicity ($[\text{Fe}/\text{H}]$). Using these values, a template from the Göttingen Spectral Library of PHOENIX spectra (GLIB, [Husser et al., 2013](#)) is chosen for each star and initial values for the radial velocities are determined by cross correlating the observed spectra of each star with the selected template.

During the actual fitting using SPEXXY, the initial guesses for the parameters are improved using a least-squares optimisation between spectra and templates across the entire MUSE wavelength range. The details of this process vary, depending on the evolutionary state of each star. For the majority of stars (on the main sequence, subgiant, red giant, and asymptotic giant branches), the template spectra are taken again from the GLIB library and all aforementioned parameters except for the surface gravity $\log(g)$ are optimized. This is because $\log(g)$ has little effect on the stellar spectra within the

sample of ω Cen (Husser et al., 2013), due to the limitations imposed by the relatively low spectral resolution of MUSE. However, the GLIB templates do not cover the effective temperature range $> 15\,000$ K required to fit the extended horizontal branch stars. Therefore, these stars were instead compared to a dedicated library, recently presented in Latour et al. (2023). In such cases, the parameters that were optimized during the fit were T_{eff} , $\log(g)$, the helium abundance instead of the metallicity (given the absence of any significant metal lines in the MUSE spectra of hot stars) and the radial velocity.

For each measured radial velocity, SPEXXY returns the nominal uncertainty derived from the covariance matrix. As previous MUSE radial velocity studies have shown (e.g., Kamann et al., 2016; Nitschai et al., 2023), SPEXXY tends to underestimate the true velocity uncertainties. As underestimated uncertainties can artificially inflate the measured binary fractions, we followed the approach outlined in Kamann et al. (2016) and determined a correction factor for the uncertainty of each velocity measurement. For each measurement of each star, we selected a comparison sample of 100 measurements from the same cube with similar stellar parameters and spectral S/N. For the measurements in the comparison sample, we calculated the normalized (by the squared sum of the uncertainties) velocity differences relative to other epochs and used the standard deviation of the resulting distribution as correction factor. For more details about this process, we direct the reader to Kamann et al. (2016).

2.2.3 Separating CMD regions

In addition to determining the radial velocities and stellar parameters, we also identify the evolutionary stage of each star in order to investigate the binarity of each evolutionary type. To do this, we separate the regions of the CMD by eye into eight main stages: main sequence (MS), turn off (TO), sub giant branch (SGB), red giant branch (RGB), horizontal branch (HB), asymptotic giant branch (AGB) and BSS.

This is an important metric, as some regions of the CMD are more likely to show binarity than others, whether it be through physical properties or observational biases. For example, BSSs are more likely to be identified as binary because this class of objects is predicted to be formed through the interactions between the two components in a binary, as discussed in Sec. 1.1.4.1. Bright stars, such as RGB stars, tend to have a higher SNR and therefore typically have lower observed velocity errors. In our sample, RGB stars have a mean velocity error of 3 km s^{-1} compared to MS stars, which have a mean velocity error of 12 km s^{-1} and lower velocity errors improve the detection limits of radial velocity variations.

We note that due to the nature of the assignment of evolutionary stage, there are some cases where multiple stages are applicable, namely at the edges of connecting regions. For these cases we include this source for all applicable evolutionary stages. This may mean that sum of the number of stars and binary systems reported totaled over each evolutionary stage may be larger than the reported global values.

2.2.4 Final sample

To select our final sample of stars, we perform a number of quality cuts as well as a cluster membership selection. The details of this process are provided in the following:

- Only results derived from spectra that were formally successfully fitted by SPEXXY were considered. A common reason for the failure of a spectral fit was that it hit the limits of the template grid for T_{eff} , $\log(g)$, or $[\text{Fe}/\text{H}]$.
- The contamination from nearby sources – that were too close to the target star to be resolved in the MUSE data and hence could not be deblended by PAMPELMUSE – in the extracted spectrum is less than 5%, as contamination under this value has little effect on the extracted spectra.
- The star was extracted more than 2 spaxel away from the edge of the MUSE field of view in order to avoid artifacts caused by incomplete coverage.
- The magnitude accuracy of the spectrum, as determined by PAMPELMUSE, is above 0.6. To determine this value, PAMPELMUSE tries to recover the magnitudes available in the photometric reference catalog by integrating over the extracted spectra. The magnitude accuracy is a measure for the agreement between the two, relative to the scatter observed for spectra of similarly bright stars. A value of 1 indicates perfect agreement whereas a value of 0 indicates a strong outlier. The cut value of 0.6 is motivated by the success of previous studies, such as [Kamann et al. \(2018\)](#) and [Giesers et al. \(2019\)](#).
- The reliability of each radial velocity measurement, as defined by [Giesers et al. \(2019\)](#), is over 80%, to ensure that the radial velocity measurements are reliable and have approximately Gaussian distributed uncertainties.
- The values derived from the spectrum analysis for T_{eff} , $\log(g)$, and $[\text{Fe}/\text{H}]$ show no outliers when compared to results from other spectra obtained for the same star. Outliers of these values suggests that the spectral analysis for that particular spectrum was unreliable.

- Field stars were discarded using a membership probability cut of 0.5. As explained in [Kamann et al. \(2016\)](#), the probability of cluster membership is derived by comparing the average [Fe/H] and radial velocity measurements of each star to assumed populations of cluster and Milky Way stars. In the case of ω Cen, which has a broad range of metallicities, this is predominantly derived using the radial velocity measurements, as the stars that would be in the foreground have a velocity of $\sim 0 \text{ kms}^{-1}$, while the systemic velocity of ω Cen is $\sim 250 \text{ kms}^{-1}$ ([Baumgardt et al., 2023](#)). Despite the spread in metallicity within the cluster, foreground stars are also expected to be considerably more metal rich than the most metal rich population of ω Cen, which allows for these stars to be confidently removed from the sample.

Following these cuts, there are 312 248 individual spectra for a total of 37 225 stars. The distribution of the number of epochs across the sample is shown in [Fig. 2.2](#). On average, a star in our sample has valid radial velocity measurements for 6 epochs. However, a large scatter in the available number of epochs per star is evident in [Fig. 2.2](#). This is caused by the varying observing conditions during the campaign, impacting the number of spectra that could be extracted from the MUSE data during each epoch. The sharp cutoff beyond 17 epochs indicates the maximum number of epochs available per pointing. Note, however, the tail extending to $\gtrsim 50$ epochs, composed of stars that are located in the overlap regions between adjacent pointings.

2.3 Removing photometric variables

In order to properly identify binary candidates in ω Cen, we also must remove stars that have been previously reported as photometrically variable, such as RR Lyrae and SX Phoenicis (SX Phe) stars. These radially pulsating stars show radial velocity variations, however the variation is not caused by a companion orbiting around in a binary. In this study we compare our sample to a compilation of two catalogues of photometric variables available in the literature, a catalogue from [Clement et al. \(2001\)](#) and a catalogue from [Braga et al. \(2020\)](#).

The [Clement et al.](#) catalogue is a summary of literature reporting variable stars, such as RR Lyrae, SX Phe stars, Semi Regulars (SRs) and Long Period Variables (LPVs). The sources in the [Clement et al.](#) catalogue were matched to the MUSE data initially via their WCS positions, with a 2 arcsecond allowance. To avoid mismatches, we restricted the potential matches in the MUSE catalog to stars on the HB, BSS, and AGB stars, as the types of variable stars previously mentioned are only found in these areas of the

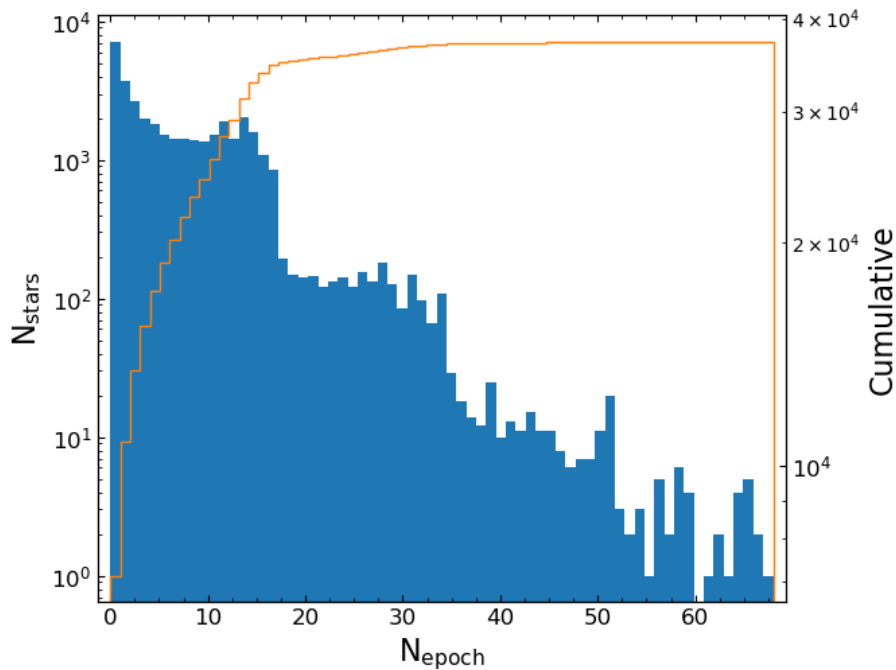


FIGURE 2.2: The distribution of the number of epochs for each source in ω Cen. The median number of epochs is 6. The orange histogram represents the cumulative number of stars that have at least a given number of epochs.

CMD. The matches were then manually confirmed by comparing the magnitudes from the [Clement et al.](#) catalogue to the F625W magnitudes available in the [Anderson & van der Marel \(2010\)](#) photometry. A source was considered a match if the magnitude reported in the [Clement et al.](#) catalogue was within 1 magnitude of the HST magnitude. From the [Clement et al.](#), we identify a total of 22 variable stars with a MUSE counterpart in our sample. The [Braga et al.](#) catalogue contains photometric variables, such as RR Lyrae, Type II Cepheids and LPVs that were found using Near Infrared and Optical data. The [Braga et al.](#) catalogue was also matched to the MUSE data through coordinate matching. From this catalogue, we identified a further 4 photometric variables.

The locations in the CMD of the matches to both the [Braga et al.](#) and [Clement et al.](#) catalogues are visualized in the right panel of Fig. 2.3. As expected, LPV and SR are found on the AGB branch, the RR Lyrae stars cluster on the horizontal branch, and nicely illustrate the location of the instability strip, and SX Phe stars are found among the blue stragglers, in agreement with the findings by [Cohen & Sarajedini \(2012\)](#).

2.3.1 MUSE identified photometric variables

The MUSE data offer the possibility to search for photometric variables, by reconstructing broadband magnitudes from the extracted stellar spectra and comparing them across

different epochs. In order to determine the probability of a star being photometrically variable, each magnitude of each star is measured relative to a sample of comparison stars that have a comparable colour and show little photometric variation across the different epochs available for each pointing. Further discussion of this method is detailed in Appendix A.1 of [Giesers \(2020\)](#). For the purposes of this study, we select a cut of 0.8 for the photometric variability, where stars with a variability > 0.8 are considered photometrically variable. The stars that we class as photometrically variable are shown as black points on the left panel of [Fig. 2.3](#). In total, 912 stars were listed as photometric variables, 6 of which match the variable stars reported in the literature. As can be verified from [Fig. 2.3](#), the majority of RR Lyrae stars are identified as photometrically variable in the MUSE data, which can be explained by their relatively strong brightness variations compared to other types of variables. However, we emphasize that the majority of stars identified as photometrically variable in the MUSE data are unlikely to show intrinsic variability. Instead, it is more likely that the photometric variations point to problems during the extraction of the spectra. Therefore, we exclude the stars showing high probabilities for photometric variability from further analyses.

2.4 Calculating the probability of variability

A common way to detect velocity variations is to determine the χ^2 of the velocity measurements per star under the assumption of a constant actual velocity. However, when processing samples as large as ours, a considerable number of large χ^2 values is expected even in the absence of binaries. This statistical noise presents a challenge when determining which stars are variable, and can strongly impact the results, especially in the regime of low binary fractions expected for ω Cen. We utilise the probability calculation method presented in [Giesers et al. \(2019\)](#), as this method avoids the high false positive detection rate by weighting each χ^2 value against the likelihood of the source being statistical noise.

This process first starts by computing the χ^2 for each star in the sample to determine how compatible the velocity measurements are with the star's mean velocity using:

$$\chi_i^2 = \sum_{j=1}^m \frac{1}{\sigma_j^2} (x_j - \bar{x})^2 \quad \text{where} \quad \bar{x} = \frac{\sum_{j=1}^m \frac{x_j}{\sigma_j^2}}{\sum_{j=1}^m \frac{1}{\sigma_j^2}} \quad (2.1)$$

For a star with m measurements of x_j with an uncertainty of σ_j compared against the mean \bar{x} . For stars with significant radial velocity variations, the value of $\chi^2 > 1$, while for stars that show little velocity variation, the value of $\chi^2 \approx 1$. In the case where there are

no binary systems in the cluster, the null hypothesis, and assuming a common degree of freedom, v (where $v = m - 1$), the expected shape of the cumulative distribution function (CDF) is known. If there are binary systems in the cluster, however, this will result in an excess of higher χ^2 values compared to the known CDF of the null hypothesis, which will result in a slower increase of the CDF. Using this principle, we can therefore compare both the expected and observed CDFs to calculate the probability for each star to match the null hypothesis:

$$\bar{P}(\chi_i^2, v_i) = \frac{1 - \text{CDF}(\chi_i^2, v_i)_{\text{theoretical}}}{1 - \text{CDF}(\chi_i^2, v_i)_{\text{observed}}} \quad (2.2)$$

To then determine if a star is variable for a given degree of freedom (v_i), the probability of variability is $P = 1 - \bar{P}$:

$$P(\chi_i^2, v_i) = \frac{\text{CDF}(\chi_i^2, v_i)_{\text{theoretical}} - \text{CDF}(\chi_i^2, v_i)_{\text{observed}}}{1 - \text{CDF}(\chi_i^2, v_i)_{\text{observed}}} \quad (2.3)$$

This approach, however, does not take into consideration that the number of velocity measurements (degrees of freedom, v_i) varies for each star. To take all degrees of freedom into account, the contributions from each degree of freedom are summed for form a “super CDF”:

$$\hat{S}(\chi_i^2) = \frac{1}{n} \sum_v \text{CDF}(\chi_i^2, v) n_v \quad (2.4)$$

Where \hat{S} is the “super CDF”, n is the total number of stars and n_v is the number of stars per degree of freedom. Using $n\hat{S}$ as an analogue for $n\text{CDF}_{\text{theoretical}}$ (and $n\text{CDF}_{\text{observed}}$) in Eqn. 2.4, we therefore define the probability of a star to be variable as:

$$P(\chi_i^2, v_i) = \frac{n\hat{S}(\chi_k^2) - k}{n - k} \quad (2.5)$$

Where k is the number of stars with a reduced χ^2 (χ_i^2/v_i) lower than that of a given star. In practice, this method compares the number of stars with a given χ^2 value against the number expected from statistical noise, and their fraction is converted to a probability value, henceforth P_{var} .

We show the calculated P_{var} values for each star in the right panel of Fig. 2.3 across the different regions of the CMD. We find a particularly high concentration of potential binary stars among blue stragglers, however this will be discussed throughout Sec. 4.2 and Sec. 6.1.

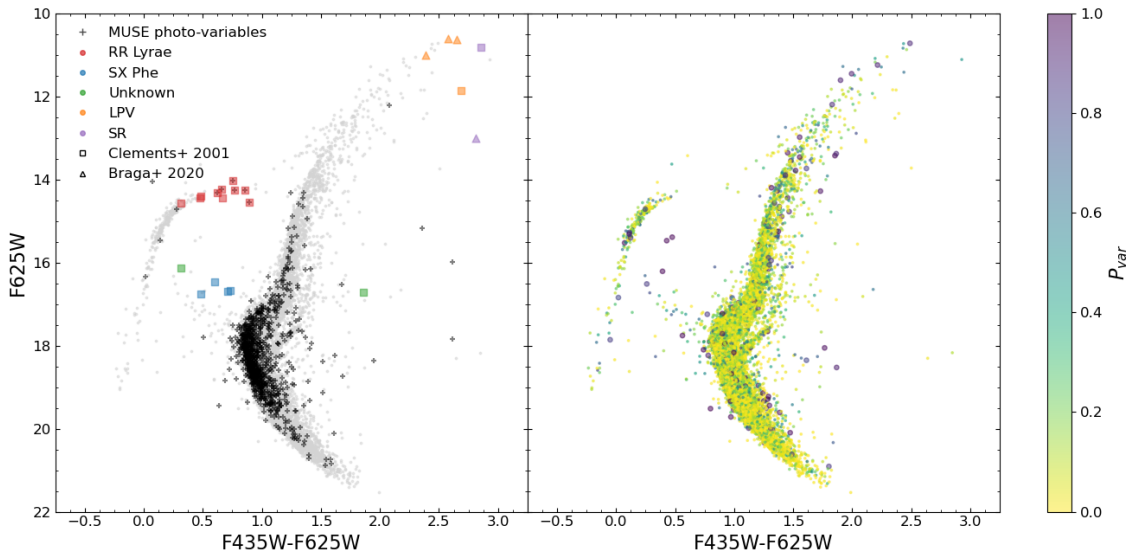


FIGURE 2.3: Stellar variability in ω Cen. Both panels show the distribution of stars in the MUSE sample across the colour magnitude diagram (CMD) of the cluster using F625W and F435W magnitudes. The left hand panel shows stars that are considered photometrically variable either in the MUSE data or the [Clement et al. \(2001\)](#) and [Braga et al. \(2020\)](#) catalogs. The right panel shows the sample with all photometric variables removed and uses a colour overlay to indicate P_{var} , the probability of a star to show velocity variations, where purple is more likely to be variable and yellow less likely, as indicated by the colour bar to the right. The larger points of the right hand panel show stars with $P_{\text{var}} > 0.8$, a cut which is discussed in [Sec. 3.3](#), which we consider as binary stars.

The distribution of P_{var} is also shown in [Fig. 2.4](#). Note that only stars with a minimum of six measurements are included in [Fig. 2.4](#), a choice that will be motivated in [Sec. 3.3](#) below. The inserted axis shows the distribution of stars with a $P_{\text{var}} > 0.8$, which will also be discussed in [Sec. 3.3](#). It is evident from [Fig. 2.4](#) that the P_{var} distribution returned by the method of [Giesers et al. \(2019\)](#) is bimodal, with a dominant peak at low probabilities. We will further elaborate this point in the following sections of this paper. We also present the full binary fraction in [Sec. 4.2](#), after a discussion on the chosen cut values.

2.5 Summary

- After the MUSE data has been reduced, the spectra extracted and quality cuts have been made, there are a total of 312 248 individual spectra across 37 225 star. The median number of epochs per star is 6.
- A total of 22 previously reported photometric variables with a MUSE counterpart and removed from the sample, 18 from the [Clement et al.](#) catalogue and 4 from

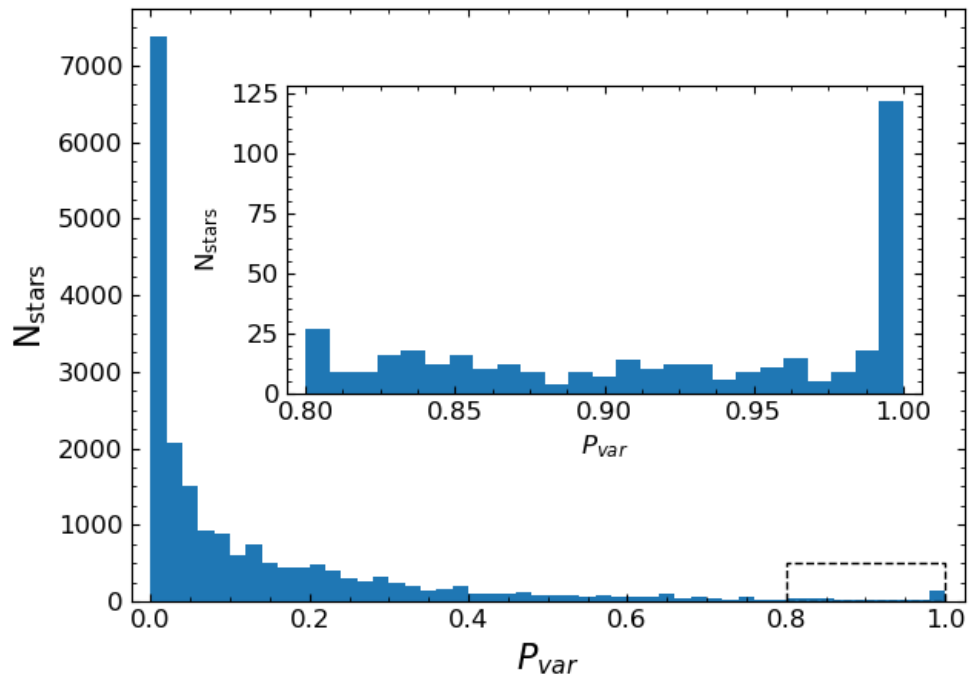


FIGURE 2.4: The number of stars in the MUSE sample with six or more epochs as a function of variability probability, P_{var} , as designed by [Giesers et al. \(2019\)](#). The inset axis shows the distribution of P_{var} between 0.8 and 1.

the [Braga et al.](#) catalogue: 10 RR Lyrae, 4 SX Phe, 4 LPV, 2 SR and 2 that are not classified.

- A total of 912 stars were identified as photometrically variable using the MUSE data, which included 6 of the identified photometric variables from the [Clement et al.](#) and [Braga et al.](#) catalogues.
- The probability of each star to be variable (P_{var}) was calculated for each source using a weighted chi-square test to assess the significance of velocity variations around the system mean velocity.

Chapter 3

Determining the Sample Completeness

“That sounds like some strange math... But I’m ready!”

Steven Universe - *Steven Universe*

In order to determine the binary fraction of ω Cen, we need to correct for the incompleteness in our analysis. Inevitably, there will be binary stars that are not classified as variable via the probability method detailed in Sec. 2.4 due to effects such as systems having a low inclination, low-mass companions on wide orbits, or damping of the true radial velocity curves by secondary stars of a similar luminosity (cf. Sec. 3.2).

Although evolutionary models for globular clusters exist, such as MOCCA (MOnte Carlo Cluster simulAtor; Giersz, 1998) and CMC (Cluster Monte Carlo; Joshi, 2000), there are no evolutionary models of ω Cen with a realistic binary population to date. There are two main factors that make modelling ω Cen difficult, the first being the unknown origin of ω Cen which, as a theorised former NSC, would require models that rely on too many assumptions to realistically track evolution. The second issue is the high number of stars in ω Cen, which would make realistic models too computationally expensive to run.

Therefore, to correct for selection effects we generate mock MUSE samples, with known binary populations and individually known orbital parameters, and apply the same probability calculation method as was applied to the observed data. By determining the ratio of the inputted binary fraction to the outputted discovery fraction of the simulated cluster, a correction factor can be derived and applied to the actual data in order to obtain a completeness-corrected binary fraction.

To generate the mock samples, we use the observed time stamps and velocity errors for each measurement of each star and calculate a new set of velocity measurements for each star, with variations depending on whether the star has been simulated to have a binary companion or it is considered a single star.

3.1 Physical principles

In order to create mock samples that are representative of ω Cen, there needs to be some consideration of what types of binary stars are expected in the dense cluster environment. In particular, we consider the constraints imposed by three-body interactions and Roche-lobe overflow on the distribution of orbital periods we expect to observe.

3.1.1 Binary hardness

The first point to consider is the hardness of the binary system; the binding energy between a primary star and its secondary companion relative to the kinetic energy of an average cluster member. As discussed in Sec. 1.1.4, if a binary system has a low binding

energy (a soft binary), it will be easily disrupted by interactions with single stars or other binary systems. If a binary system has a high binding energy (a hard binary), it is much more likely to survive the cluster environment, as it is harder for interactions to destroy the system (Heggie, 1975). In order to determine the hardness of a binary, we follow Ivanova et al. (2005) and write down the ratio between the binding energy of a binary and the kinetic energy of a typical clusters star as

$$\eta = \frac{GM_1M_2}{a\sigma^2\langle M \rangle}, \quad (3.1)$$

where η is the binary hardness, M_1 and M_2 are the masses of the primary and secondary stars respectively, $\langle M \rangle$ is the average mass of a star in the cluster, a is the semi-major axis of the binary system, and σ is the average velocity dispersion of the cluster.

A binary system is considered a soft binary if $\eta < 1$, and a hard binary if $\eta > 1$. Using Eq. 3.1 with Kepler's third law, the binary hardness can be determined for different orbital periods for given companion masses. For example, assuming a dispersion of $\sigma = 21 \text{ kms}^{-1}$, calculated using the MUSE data, and an average mass of $\langle M \rangle = 0.5 M_\odot$, we can estimate that the maximum period for a binary system composed of two typical main sequence stars of average mass is approximately 10^3 days, with the maximum period getting shorter as the companion becomes less massive. As soft binary systems are expected to be rapidly disrupted in the dense environment of ω Cen, simulated binary systems with a hardness $\eta \leq 1$ are ignored.

3.1.2 Roche lobe filling

In order to obtain a lower limit for the periods feasible in our sample, we consider the Roche limit, i.e. the point at which two stars in a binary system become connected by the mass transfer of one of the stars. The radius r_1 of the Roche lobe of the primary star is described by the Eggleton (1983) equation:

$$\frac{r_1}{A} = \frac{0.49q^{2/3}}{0.6q^{2/3} + \ln(1 + q^{1/3})}, \quad \text{with } q = \frac{M_1}{M_2} \quad (3.2)$$

Here, A is the orbital separation of the stars and M_1 and M_2 are the mass of the primary and secondary star, respectively.

In order to determine if a binary system is feasible, we compare r_1 to the radius of the primary star, estimated using the isochrone comparison described in Sec. 2.2 above. If the latter exceeds the former, we discard the binary system and treat the system as a single star. We note that interacting binary stars showing Roche-lobe overflow

are expected in a dense environment such as ω Cen, but are unlikely to contribute significantly to the overall statistics. The study by [Göttgens et al. \(2019\)](#) found only 9 emission-line sources in the MUSE sample of ω Cen, with most of them being known photometric variables (cf. Sec. 2.3).

3.2 Generating the mock sample

When creating a mock sample, we pick a random subsample of the stars (with a size corresponding to the selected binary fraction) and assign each star as the primary star in a binary systems with orbital properties in line with the following assumptions:

- The mass ratio distribution is described by a power law function $F(q) = q^\gamma$. The default value for γ is 0, corresponding to a uniform distribution of mass ratios, in line with [Ivanova et al. \(2005\)](#) and [Woitas et al. \(2001\)](#).
- The default distribution for inclination is a uniform distribution of $\arccos i$ between 0 and 1, corresponding to an isotropic distribution of orbital planes.
- The period distribution is a log normal distribution with a mean value of $10^{0.5}$ days and a standard deviation of $10^{1.5}$ days. This choice is motivated by the period distributions found in the simulations of [Ivanova et al. \(2005\)](#).
- The phase of time in the orbit during the first epoch, t_0 , is a uniform distribution between 0 and the value of P for each given binary.
- The default distribution of eccentricity, e , is a beta distribution, for which the probability density function (PDF) is defined as:

$$f(x, \alpha, \beta) = \frac{\Gamma(\alpha + \beta)x^{\alpha-1}(1-x)^{\beta-1}}{\Gamma(\alpha)\Gamma(\beta)} \quad (3.3)$$

Where Γ is the gamma function. The use of a beta distribution is motivated by work by [Kipping \(2013\)](#), which found that a beta distribution most accurately represents the observed distribution of eccentricity in exoplanet orbits. We use default values of $\alpha = 2$ and $\beta = 5$, however as part of our analysis, a wide range of assumed β values are tested (see discussion in Sec. 3.4). For short periods, we also impose a maximum eccentricity to avoid Roche lobe overflow according to the following formula ([Moe & Di Stefano, 2017](#)).

$$e_{\max}(P) = 1 - \left(\frac{P}{2 \text{ days}}\right)^{-2/3} \quad \text{for } P > 2 \text{ days} \quad (3.4)$$

If a binary system is found to have an eccentricity higher than e_{\max} , that systems eccentricity is set to e_{\max} . For periods ≤ 2 days, we assume that the orbit is circularised. Implementing this maximum eccentricity prevents generating orbits that are so eccentric that they will overflow their Roche lobes.

- The argument of periapsis, ω , is a uniform distribution between 0 and 2π for each given orbit.

Along with each set of randomised orbital parameters for the binary systems, each star, whether binary or not, is assigned a randomised mean system velocity, v_{sys} , which is taken from a normal distribution with the mean value $\mu = 250\text{kms}^{-1}$, the mean velocity of ω Cen calculated using the MUSE data, and a standard deviation $\sigma = 21\text{kms}^{-1}$, the central velocity dispersion of ω Cen, also calculated using the MUSE data. We assume a constant velocity dispersion as the velocity dispersion curve of ω Cen is relatively shallow (e.g., Sollima et al., 2019) within the central region relevant for this study and, while this assumption may lead to an overestimation of completeness, we anticipate that the effect on the results are limited. This will be discussed further in Sec. 6.2.1.

Following the assignment of orbital parameters, we discard all systems that violate the criteria on binary hardness and Roche-lobe overflow set out in Secs. 3.1.1 and 3.1.2, respectively. These stars are treated as single stars instead. We note that the binary fraction that we assume for the mock set is calculated following this step. For each actual velocity measurement in the MUSE catalog, we then create a mock velocity measurement. To this aim, we first use the orbital parameters of the mock sample to determine the Keplerian velocities of the stars in binaries, at the timestamps of the observations, using the method discussed in Sec. 1.4.2 and Eqn. 1.4.

Having calculated the Keplerian velocity, we then consider luminosity damping of a primary star due to its secondary, particularly in the case where the primary and secondary stars have comparable luminosities. In these cases, the red and blueshifts in the spectra of the two components relative to the observer negate one another, resulting in widened spectral lines rather than observable shifts. As shown by Bodensteiner et al. (2021) or Saracino et al. (2023), this effect causes the detection efficiency of MUSE observations to drop for binaries composed of unevolved stars with mass ratios close to unity. To take this effect into account, we adopt the equation used by Giesers et al. (2019)

$$v_{\text{obs}} = v_{\text{sys}} + (1 - 10^{0.4(m_1 - m_2)})v_t, \quad (3.5)$$

where v_{obs} is the observed velocity of the primary, v_{sys} is the systemic velocity of the binary, v_t is the true Keplerian velocity of the primary, and m_1 and m_2 are the F625W magnitude of the primary and secondary star, respectively. The magnitude of

the secondary is adopted from the isochrone, by finding the closest match in terms of mass along the main sequence. This damping factor is then applied to the Keplerian velocities of all binary systems in the mock data.

For the single stars in the sample, the velocity is simply set to v_{sys} for all timestamps, which is a valid assumption as the detection efficiency is not impacted by the exact velocity measurement. Finally, we create each mock measurement by drawing a random number from a Gaussian distribution, centred on the velocity calculated for the star and the timestamp in question, with standard deviation equal to the uncertainty of the observed velocity. These mock data sets are created for a set of 11 input binary fractions ranging between 0% and 20% input fraction in steps of 2%. The flow chart shown in Fig. 3.1 provides a visual guide to the mock data generation process.

Figure 3.2 shows the distribution of the orbital parameters for both the initial input of binary systems, and the surviving fraction following the removal of soft and interacting binaries. For this, we use the default assumptions for input parameters, where $\log(P_{\text{mean}}/d)=0.5$, $\log(P_{\sigma}/d)=1.5$, $\gamma=0$, $\beta=3$, and the input binary fraction 4%. We select the input fraction as 4% as this gives a discovery fraction comparable to the observed data, which will be discussed in Sec. 4.1. The top panel of Fig. 3.2 shows that the Roche-lobe criterion outlined in Sec. 3.1.2 limits the periods we expect in our sample to $\gtrsim 0.1$ d, whereas the criterion on binary hardness defined in Sec. 3.1.1 confines the expected distribution to $\lesssim 1000$ d. The impact of the binary hardness criterion is also visible in the middle panel of Fig. 3.2, as binaries with low mass ratios are preferentially removed from the input sample. The peak of eccentricity at 0, visible in the lower panel of Fig. 3.2, is due to the assumed circularisation of binaries with periods under 2 days.

3.3 Binary recovery as a function of probability

Using the mock samples, we first investigate how the completeness and purity of our sample of detected binary candidates in ω Cen changes depending on the requirements we impose on the minimum values of P_{var} and the number of epochs. Our aim here is to minimise the number of false positive detections of binary stars, whilst at the same time maximizing the fraction of detected binaries. In Fig. 3.3, we show the fraction of detected binaries (relative to the number of binaries in the mock sample) as well as the fraction of false positives (relative to the number of total detections) as a function of the cut-off on the P_{var} , and for different cut-offs on the number of available epochs.

Fig. 3.3 shows that the fraction of false positives is most dependent on the minimum P_{var} value, while the minimum number of epochs only marginally affects the fraction.

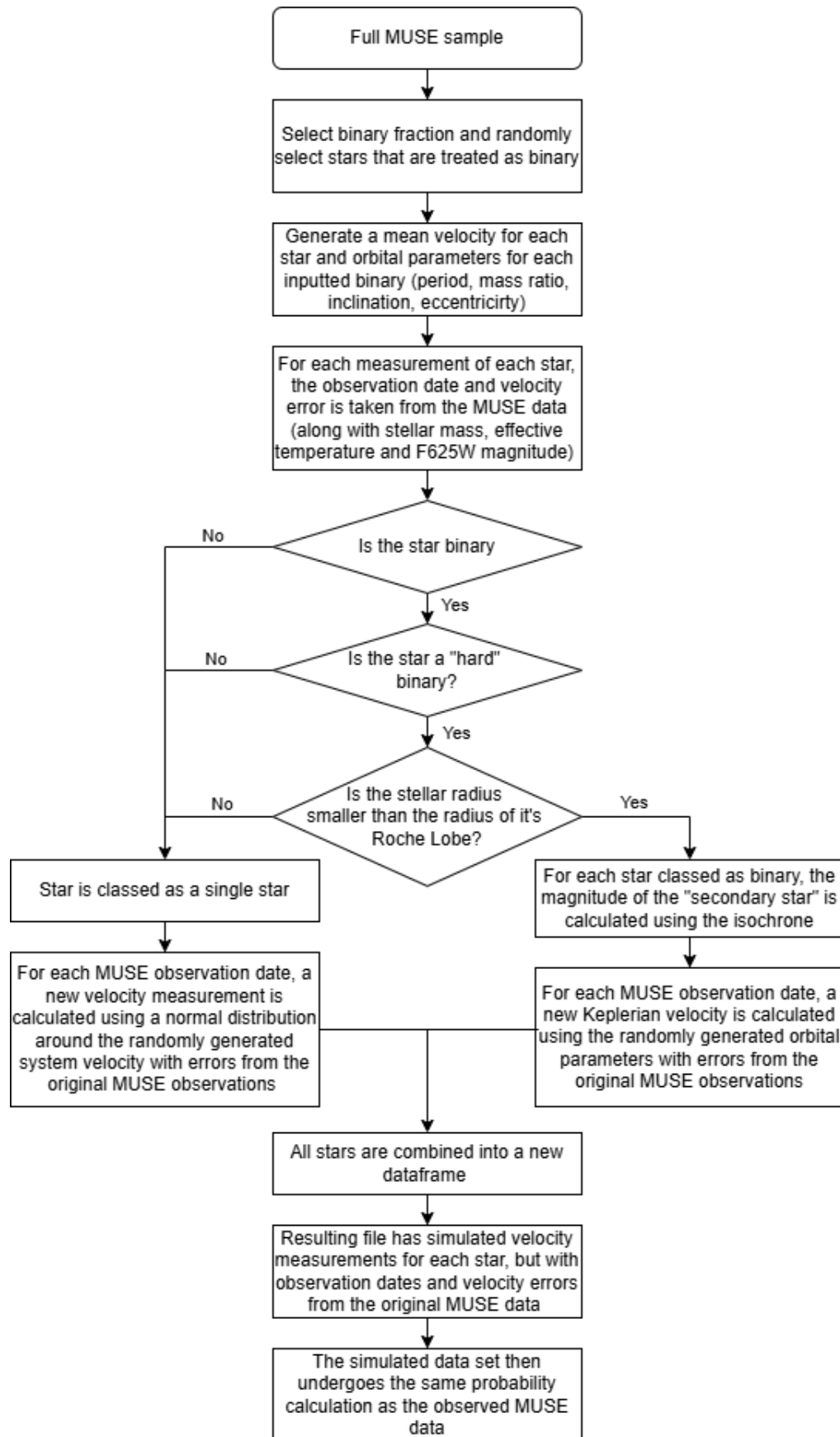


FIGURE 3.1: A flow chart highlighting the key steps in generating the mock data sample. This process is repeated for 11 input binary fractions, between 0 – 20%.

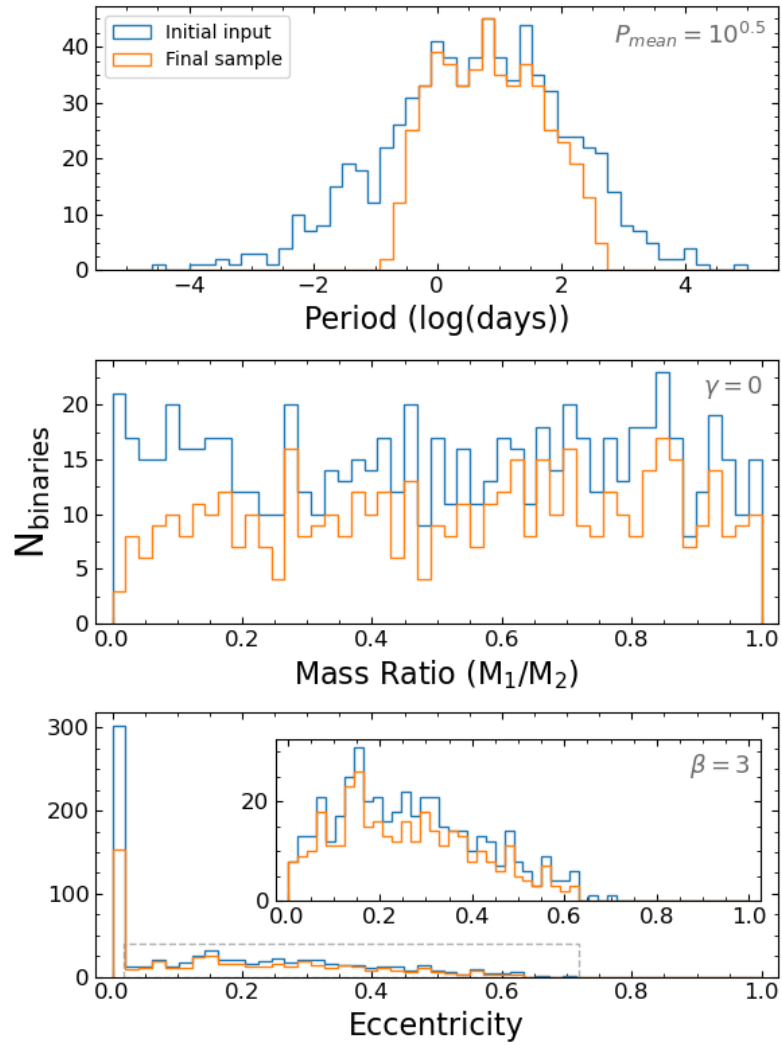


FIGURE 3.2: The distribution of orbital parameters in the mock sample with an intrinsic binary fraction of 4%, both before (blue) and after (orange) the removal of soft and interacting binaries. The top panel shows the distribution of periods, the central panel the distribution of mass ratios, and the bottom panel the distribution of eccentricities. In order to better visualize the distribution of binaries with non-zero eccentricity, the inserted panel shows the eccentricity distribution following the removal of circular orbits. The initial sample (blue) contains 485 stars and the final sample (orange) contains 265 stars

However, the minimum number of epochs has a significant impact on the completeness of our analysis, which increases by $\sim 10\%$ when going from 4 to 10 epochs.¹

In order to maintain a clean sample of binary stars, we request that the false positives represent 2σ outliers in the final sample, i.e. that $\lesssim 5\%$ of the stars considered as binaries are false positives. For the baseline simulation discussed at the end of Sec. 3.2, adopting a minimum of $P_{var} = 0.8$ yields a false positive fraction of 4.5%, almost independent

¹Note that “completeness” is defined relative to the number of stars surviving our quality and epoch cuts, not relative to the entire MUSE sample.

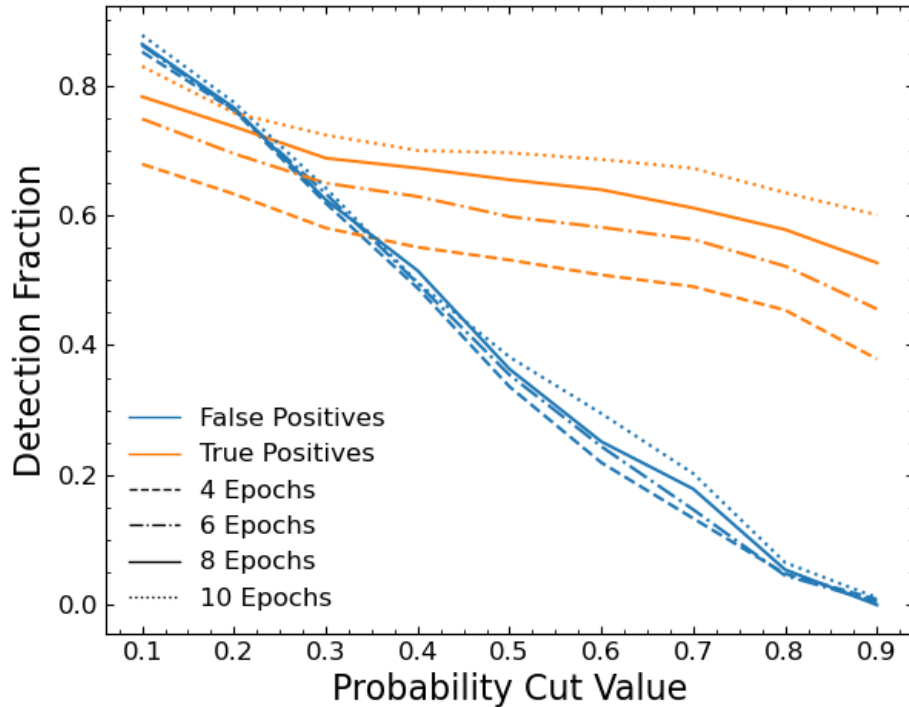


FIGURE 3.3: Completeness and purity of the sample of detected binaries in ω Cen, as predicted by the mock data. In orange, we illustrate how the fraction of detected binary stars depends on the minimum required P_{var} , while in blue, we show the dependence of the fraction of false positives as a function of the P_{var} cut-off. Different line symbols are used to illustrate the impact of increasing the number of required epochs available for each star entering the analysis.

of the number of epochs required. We note that other methods can be used to infer a well-defined cut-off value. For example, [Johnson et al. \(2015\)](#) studied the relation between completeness and contamination and adopted the probability threshold that minimized the distance of the relation to the point representing the ideal situation of a fully complete and uncontaminated sample.

Furthermore, we adopt a minimum number of 6 epochs per star, as it represents a good trade-off between maintaining a large sample and retaining a high fraction of correctly identified binaries. Using these cuts, we find that the fraction of known binary stars from the mock simulation that are correctly identified is 52%. We completed a similar test, using these updated cut values, to assess the effect of the minimum required signal-to-noise on the false positive fraction, but the effect was negligible compared to the effects of P_{var} and epoch cut. Having applied the 6 epoch cut to the observed data, our sample now includes 19 059 individual stars.

3.4 Binary recovery as a function of orbital parameter

Using the simulated data, we can investigate the completeness of our binary search in ω Cen for different parts of the parameter space. To this aim, we show in Fig. 3.4 how the detection of velocity variations is affected by the period, mass ratio, inclination, and eccentricity of the mock binary systems. We combined the values of P_{var} of the input binary population across all simulations with the default parameter distributions, binned them as a function of the various orbital parameters, and calculated the mean value of P_{var} in each bin. As expected, the period of a binary system has the strongest impact on its detectability. Excluding systems with very low mass ratios, our detection rate is expected to be nearly 100% for periods $\lesssim 10$ d, whereas it drops to $\sim 30\%$ for longer-period binaries. In terms of mass ratio, we see a significant increase in the detection rate for more massive companions. The MUSE data appear most efficient in detecting binaries with mass ratios $\sim 0.6 - 0.8$, with the drop in efficiency as the mass ratios approach unity due the damping explained in Sec. 3.2. The drop in efficiency with decreasing inclination visible in the central panel of Fig. 3.4 is also expected. It is reassuring though that even for inclinations as low of 20 degrees, we still detect a considerable fraction of the binaries.

In light of the strong variation of P_{var} across the binary parameter space expected in ω Cen that is visible in Fig. 3.4, we also investigate the impact of changing the binary parameter distributions that are underlying the mock sets. To test the impact of the assumed period distribution, we use a range of $\log(P_{\text{mean}}/\text{d})$ values between -0.6 and 2.0, in steps of 0.2, with a fixed standard deviation of $10^{1.5}$ days. The reasoning behind this choice is that the resulting period distributions include some that are significantly skewed towards the minimum period range set by the onset of Roche-lobe overflow (cf. Sec. 3.1.2), and others that are significantly skewed towards the boundary between hard and soft binaries (cf. Sec. 3.1.1). To test the impact of the mass ratio distribution, we use a range of γ values (see Sec. 3.2) ranging from 0.6 to 2.0 in steps of 0.2. This distribution is chosen as it allows testing of both a uniform mass distribution, which is used as an assumption in the simulations by Ivanova et al. (2005) in line with Woitas et al. (2001), but also distributions biased towards lower and higher mass ratio systems respectively. To test the impact of the assumed eccentricity distribution, we use a range of β values (described in Sec. 3.2) between 3 and 11 in steps of 2, resulting in distributions which are more biased to circularised and elliptical orbits, respectively. For each parameter distribution, we determine the discovery fraction for each of the 10 input binary fractions, ranging from 0% to 20%,

Following these tests, and having determined appropriate cut values based on P_{var} and the minimum number of measurements, we can now determine the completeness of

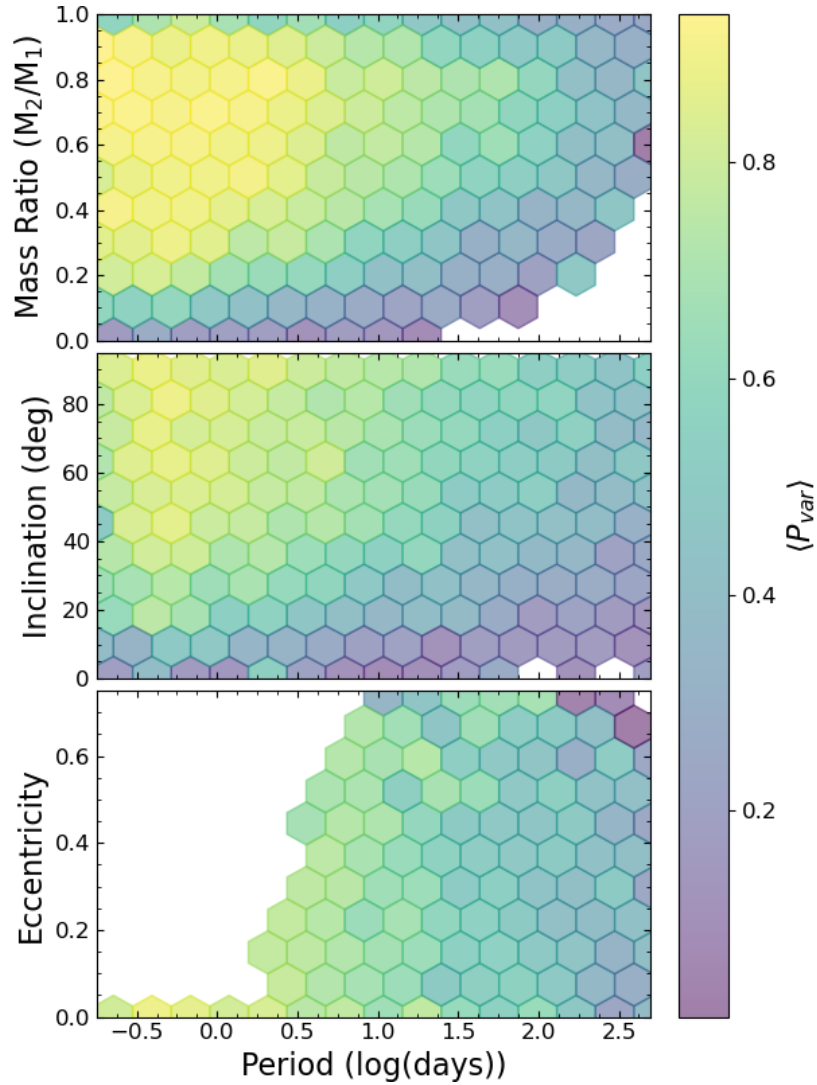


FIGURE 3.4: The mean binary probability, $\langle P_{\text{var}} \rangle$, of binary systems in the mock samples, shown as a function of their orbital period, mass ratio, inclination and eccentricity. Brighter colours correspond to higher mean values, as indicated by the colour bar to the right.

the sample. Our completeness is based on the mock data with the default parameter assumptions, as detailed in Sec. 3.2. To calculate the completeness, we compare the number of stars that are classed as binary systems in the mock data against the number of stars that are classed as binary using P_{var} . By doing this across all of the 11 input binary fractions (see Sec. 3.2), it is possible to determine the average fraction of detected binary systems. To determine the uncertainty, we combine the standard deviation of the combined correction factors for all of the mock data across each of the various parameter distributions. In Fig. 3.5, we show the dependence of the detection on the values assumed for the different distribution parameters, averaged over all input binary fractions. The detection fraction is shown for both the entire MUSE sample, and different regions in the CMD of ω Cen. From the figure, we see that the orbital period

Stellar Type	CF
Global Fraction	0.7 ± 0.1
MS	0.6 ± 0.1
TO	0.6 ± 0.1
SGB	0.8 ± 0.1
RGB	0.9 ± 0.1
HB	0.8 ± 0.1
AGB	-
BSS	$0.6 \pm 0.1^*$

TABLE 3.1: The completeness, CF, of the global population and across the regions of the CMD. Calculating completeness for the AGB region was not possible due to the lack of identified binaries within the region.

*Using MS correction factor (see Sec. 3.4)

distribution has the largest effect on the completeness correction value, the latter varying by $\sim 20\%$ between the two extremes of the distribution parameter range. Interestingly, the assumption on the mass ratio distribution seems to have a comparably strong impact, whereas the assumed eccentricity distribution has little effect on the completeness. Globally, we determine a completeness of 0.7 ± 0.1 , however the completeness varies across the CMD. Our detection efficiency is highest for the SGB, RGB, and HB stars in the sample, whereas we appear to be most incomplete in detecting MS binaries, due to the differences in brightness between the individual groups, resulting in signal-to-noise ratio differences in the MUSE spectra and ultimately in differences in the achieved radial velocity accuracies. We note that due to the small sample size of the BSS population, the detection efficiency for this region is poorly constrained and so, as velocity error has the largest effect on detection efficiency, we adopt the efficiencies determined for MS stars for the region as the velocity uncertainties for BSS and MS stars are similar. The full set of completeness values for each region of the CMD is listed in Tab. 3.1 and Tab. 4.2 column (e).

3.5 Summary

- We have created a script to generate a set of mock MUSE observations for a known binary fraction, which takes into account not only physical principles, such as Roche-Lobe filling, binary hardness and limits on eccentricity, but also observational effects, such as luminosity damping and observational noise
- We then created a suite of mock data sets for ω Cen, with a range input binary fractions and a range of distributions of orbital parameters, such as orbital period, mass ratio and eccentricity.

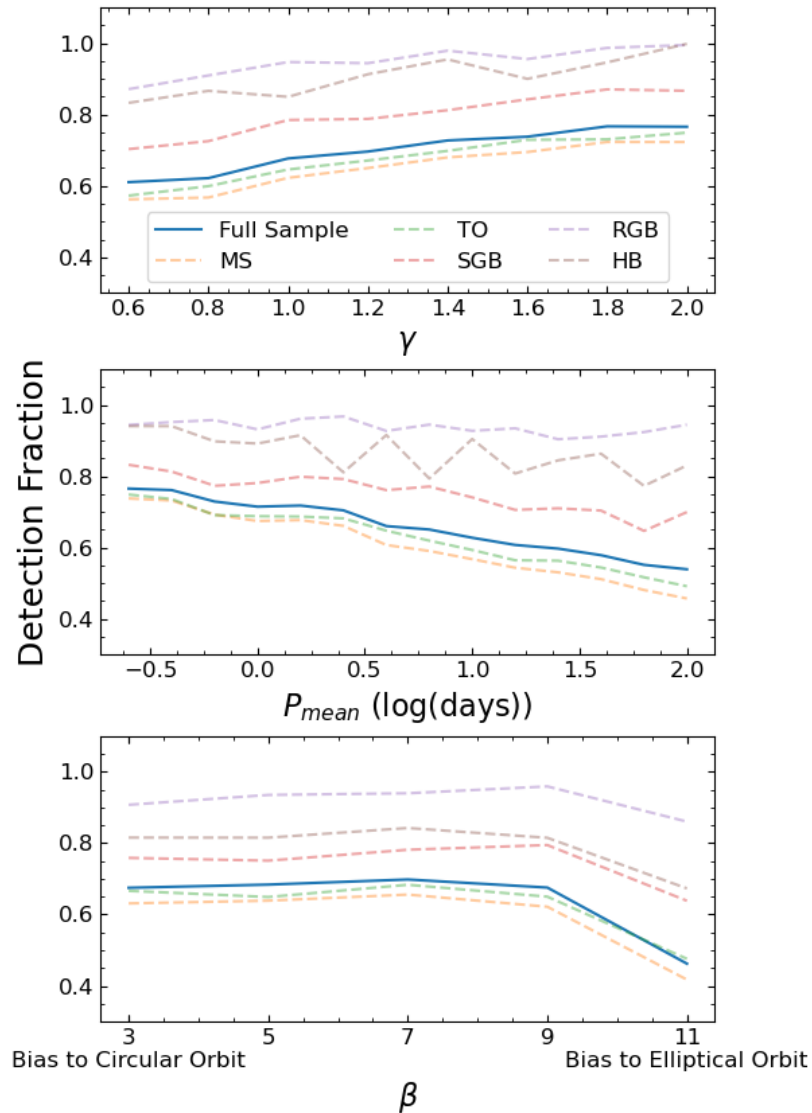


FIGURE 3.5: The recovered fraction of binaries in the mock data, as a function of the assumed values of different parameters that govern the distribution of orbital properties in the mock data: the power-law coefficient of the mass-ratio distribution (top), the mean period (middle), and the β -parameter defining the shape of the eccentricity distribution (bottom). The results for the full MUSE sample are shown as solid blue lines, while dashed coloured lines display the results obtained for different evolutionary stages.

-
- The optimal cuts to ensure a low percentage of false positive results, while maintaining a large sample size, has been determined. All sources must have at least 6 epochs, which reduces the sample to 19 059 individual stars, and to be considered binary, a star must have a $P_{\text{var}} > 0.8$.
 - Overall, the completeness of the sample is 0.7 ± 0.1 . The completeness is higher, however, for RGB stars, as the velocity errors of RGB stars are typically smaller than MS counterparts.

Chapter 4

Calculating the Binary Fraction

“There are millions of possibilities for the future, but it’s up to you to choose which becomes reality.”

Garnet - *Steven Universe*

4.1 Calculating the discovery fraction

With the reported photometric variables cleaned from the sample, the discovery fraction of ω Cen can be determined both globally and for different regions of the CMD, calculated by dividing the number of observed variable stars by the total number of stars. Therefore, having removed photometric variables from the sample and applying the minimum 6 epoch cut, and using the probability calculation method discussed in Sec. 2.4 with a probability threshold $P_{\text{var}} > 0.8$, we find that out of the 19059 stars in the sample, 275 show variability in their radial velocities. To calculate uncertainty, we use a bootstrapping analysis on the values of P_{var} with a 1σ confidence level to calculate the confidence interval of the calculated discovery fraction, both for the global population and for each area of the CMD. A breakdown of the number of stars and identified binary systems for each region of the CMD are shown in Tab. 4.1 and in Tab. 4.2 in columns (b) and (c), respectively. We find the global discovery fraction for ω Cen to be $1.4 \pm 0.1\%$, with the global discovery fraction and the fraction for the separate regions of the CMD shown in Tab. 4.2 in column (d). This fraction varies depending on the region of the CMD that is considered. As discussed in Sec. 3.4, our efficiency is higher for brighter stars and at fixed colour, and also tends to increase for cooler stars. This being the case, we find that the discovery fraction amongst RGB stars is approximately 1% higher than MS stars.

Although the discovery fraction for most areas of the CMD is approximately 1-3%, we note that the Blue Straggler Stars (BSS) have an enhanced discovery fraction of $13.6 \pm 5.1\%$. This is considerably higher than any of the other discovery fractions and suggests a $\sim 3 \times 10^{-5}$ probability that the discovery fraction of BSS is consistent with the global discovery fraction. This is, however, an expected result as it is commonly assumed that BSSs form via binary interactions, like mergers or mass accretion from a binary companion (Stryker, 1993), as discussed in Sec. 1.1.4.1.

Stellar Type	N_{stars}	N_{bin}	f_{disc}
Global Fraction	19059	275	$1.4\% \pm 0.1\%$
MS	14871	183	$1.2\% \pm 0.1\%$
TO	7897	84	$1.1\% \pm 0.1\%$
SGB	2396	23	$1.0\% \pm 0.3\%$
RGB	1811	41	$2.3\% \pm 0.4\%$
HB	232	6	$2.6\% \pm 1.3\%$
AGB	33	0	0%
BSS	44	6	$13.6\% \pm 5.1\%$

TABLE 4.1: The discovery fraction, f_{disc} , of ω Cen, along with the number of stars, N_{stars} , and the number of identified binary systems, N_{bin} , in the sample. We see a statistically significant increase in the BSS discovery fraction.

4.2 Corrected binary fraction

Using the discovery fractions presented in Sec. 4.1 and the completeness corrections from Sec. 3.4, we present the results for the binary fraction of ω Cen in Tab. 4.2 column (f).

We report that the global corrected binary fraction of Omega Centauri is $2.1\% \pm 0.4\%$. This fraction is in reasonable agreement to the photometric estimate of $2.70\% \pm 0.08\%$ obtained by Bellini et al. (2017) and the upper limit of 5% from Elson et al. (1995). Existing spectroscopic estimates of the binary fractions of globular clusters include the study of M4 by Sommariva et al. (2009), which reported a lower limit of $3\% \pm 0.3\%$, and the study of NGC 3201 by Giesers et al. (2019), which reported a fraction of $6.75\% \pm 0.72\%$. Both clusters are significantly less massive than ω Cen and Milone et al. (2012b) have shown that the binary fraction of Galactic globular clusters decreases with cluster luminosity (and hence mass). For the most massive clusters in their sample, Milone et al. (2012b) derive central binary fractions of few percent, in good agreement with our estimate for ω Cen.

Both the results from Elson et al. (1995) and Bellini et al. (2017) use the photometric approach discussed in Sec. 1.4.1. The study by Elson et al. used a CMD created from data from the Planetary Camera aboard HST, while the study by Bellini et al. used the 26 filter astro-photometric catalogue of the central region of ω Cen, also from HST. In both cases, the estimates for binary fraction rely on the separation of CMD into a binary main sequence, as the luminosity of a binary system made up of two equal mass stars will be double that of a singular star of the same mass. As discussed in Sec. 1.4.1, the complexity of ω Cen makes this approach particularly difficult, particularly as each

Stellar Type (a)	N_{stars} (b)	N_{bin} (c)	f_{disc} (d)	CF (e)	f_{bin} (f)
Global fraction	19059	275	$1.4\% \pm 0.1\%$	0.7 ± 0.1	$2.1\% \pm 0.4\%$
MS	14871	183	$1.2\% \pm 0.1\%$	0.6 ± 0.1	$2.0\% \pm 0.5\%$
TO	7897	84	$1.1\% \pm 0.1\%$	0.6 ± 0.1	$1.6\% \pm 0.4\%$
SGB	2396	23	$1.0\% \pm 0.3\%$	0.8 ± 0.1	$1.2\% \pm 0.4\%$
RGB	1811	41	$2.3\% \pm 0.4\%$	0.9 ± 0.1	$2.4\% \pm 0.4\%$
HB	232	6	$2.6\% \pm 1.3\%$	0.8 ± 0.1	$3.0\% \pm 1.5\%$
AGB	33	0	0%	-	-
BSS	44	6	$13.6\% \pm 5.1\%$	$0.6 \pm 0.1^*$	$21.9\% \pm 9.5\%$

TABLE 4.2: The binary fraction of ω Cen. Column (a) denotes the area of the CMD focused on for each calculation, along with the full sample. Columns (b) and (c) show the total number of stars, N_{stars} , and number of detected binary systems, N_{bin} , for each region of the CMD, respectively. Column (d) lists the discovery fraction, f_{disc} , of ω Cen as discussed in Sec. 4.1. Column (e) lists the completeness, CF, of each sample (see Sec. 3.4). Column (f) lists the fully corrected binary fraction, f_{bin} , of ω Cen. We see an increase in both the discovery and binary fractions particularly in the BSS region of the CMD.

* Using MS correction factor (see Sec. 3.4)

of the 15 multiple population branches will have their own binary sequence. In the study by [Elson et al.](#), multiple populations were not considered and the binary main sequence was selected as the parallel branch to the main sequence, while the study by [Bellini et al.](#) attempted to identify and remove binary stars from the sample for their study of multiple populations. This may explain why the upper limit from [Elson et al.](#) is approximately double that of this work, which is independent of photometry or chemical abundance, and the study by [Bellini et al.](#), which took into consideration the effect of multiple populations.

As discussed in the drawbacks of the photometric approach in Sec. 1.4.1, binary fractions calculated using photometry is biased towards systems where the mass ratio is close to unity, as the method is not sensitive to low mass ratio systems. This is emphasised by both authors, who each report their calculated binary fraction as a cautious estimate. The binary fraction we calculate is independent of photometry and chemical abundance, and therefore may provide a more robust binary fraction for the cluster.

The results also show a larger binary fraction in the BSS population, with a binary fraction of $21.9\% \pm 9.5\%$. While the binary fraction has a large error associated due to the small sample size, there is a significantly higher percentage seen both in the binary fraction and the discovery fraction. A higher BSS binary fraction is also seen in the [Giesers et al. \(2019\)](#) study of NGC 3201, at $57.5\% \pm 7.9\%$. This result is consistent with the mass transfer BSS formation scenarios, either within binary and triple systems ([Antonini et al., 2016](#)).

4.2.1 Radial distribution of binaries

To investigate the effects of mass segregation within the cluster, we determined the discovery fraction as a function of projected distance to the cluster centre, using the cluster centre position $(\alpha, \delta) = (13:26:47.24, -47:28:46.45)$ as reported by [Anderson & van der Marel \(2010\)](#). We separate the stars into bins of 1000 based on the distance from the cluster centre, and applied the completeness discussed in Sec. 3.4 to each bin. The results of this analysis are shown in Fig. 4.1. Also shown in Fig. 4.1 is the best fitting linear gradient and its uncertainty interval.

Through mass segregation, discussed in Sec. 1.1.2, we would expect there to be some dependence on distance from the cluster centre. From Fig. 4.1, however, and assuming a linear relation, we see no significant correlation, with a gradient of $(-0.001 \pm 0.003) \text{ arcsec}^{-1}$ inside the half mass radius of the cluster, which suggests that binary segregation in ω Cen is limited. This result agrees with results based on other tracers,

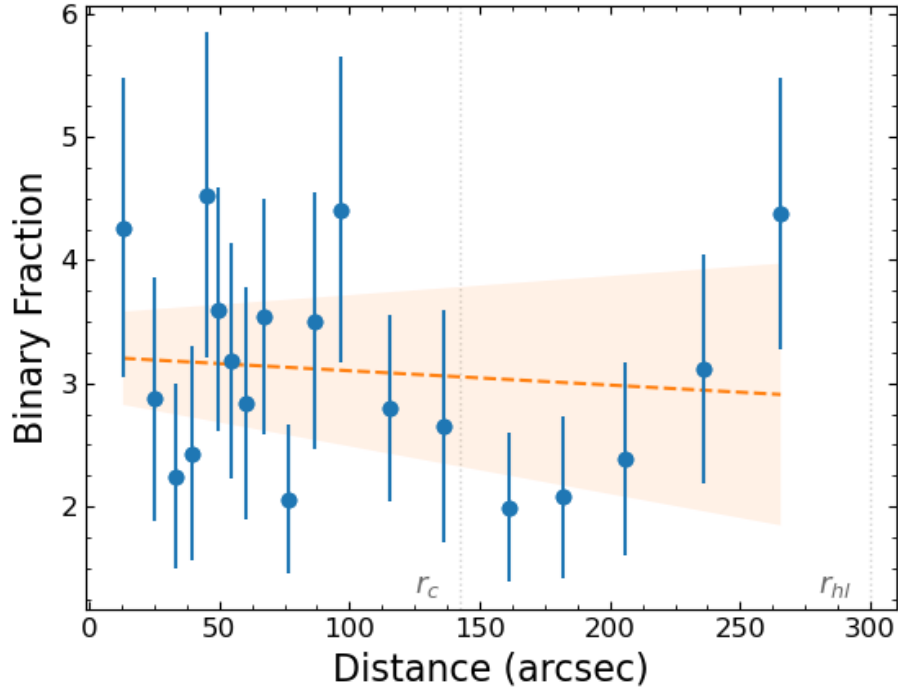


FIGURE 4.1: The binary fraction of ω Cen against the radius from the cluster centre. The data is binned such that one point represents 1000 stars. The best-fitting gradient of the distribution of $(-0.001 \pm 0.003) \text{ arcsec}^{-1}$ is shown as a dashed line, and the confidence interval as an orange-shaded area. The core radius and half light radius as reported by Harris (1996) are marked with dotted grey lines.

such as a limited amount of energy equipartition (Watkins et al., 2022) or the shallow gradient in the slope of the mass function (Baumgardt et al., 2023).

Simulations of GCs by Aros et al. (2021) suggest a flattened and lowered radial distribution of binary stars may also indicate an IMBH, however, a large collection of black holes may also have the same effect, albeit lessened. This is particularly important given the recent detection of high velocity stars at the centre of ω Cen by Häberle et al. (2024), and a flattened radial distribution of binary systems may provide additional evidence for the cluster to host an IMBH. The simulations by Aros et al. use simulated clusters of a lower mass than ω Cen with a binary fraction of 10% and with binary properties specific to each cluster, which may make the results less applicable to the observed distribution. Hence, further investigations into the expected distribution of binary stars in ω Cen in either scenario are needed in order to draw firm conclusions from Fig. 4.1.

Although we initially assume a linear relation between clustercentric distance and binary fraction, it is important to consider a non linear relation. The apparent dip seen in Fig. 4.1 between $\sim 110''$ and $\sim 220''$ shows similarities to the so called “dynamical clock” presented by Ferraro et al. (2012, 2020), which describes a link between the radial

distribution of BSSs and dynamical age. For dynamically young clusters in the early stages of mass segregation, BSSs from intermediate distances from the cluster centre migrate towards the centre of the cluster. Due to the longer relaxation time in the cluster outskirts, however, binaries in the outer regions of the cluster have not yet migrated into this intermediate region, resulting in a dip in the population of BSSs at this intermediate distance. The observations of the “dynamical clock” have been corroborated by further observations of dynamically young clusters by [Salinas et al. \(2012\)](#) and [Dalessandro et al. \(2015\)](#). Given that binary systems are impacted by mass segregation in a similar fashion as BSSs and that ω Cen is a dynamically young cluster, it is possible that the feature seen in the $110''$ and $220''$ region is an example of this relationship. In our analysis, we fit higher order polynomials to the data and, while higher order polynomials do improve the fit, the improvements seen were not statistically significant.

4.3 Summary

- Having determined an appropriate binarity threshold, the discovery fraction of ω Cen is calculated to be $1.4\% \pm 0.1\%$. This fraction is slightly increased to $2.3\% \pm 0.4\%$ for RGB stars due to the increased sensitivity in RGB binary detection.
- The BSS population shows a significantly increased fraction of binary stars at $13.6\% \pm 5.1\%$, which has a $\sim 3 \times 10^{-5}$ probability of being consistent with the global population.
- Having then corrected for completeness, the binary fraction of ω Cen is calculated to be $2.1\% \pm 0.4\%$. This is again higher for RGB stars, however the fraction of RGB binaries is more consistent with the global fraction. There are a total of 275 detected binaries in the cluster.
- The binary fraction of BSS stars is higher than the global fraction at $21.9\% \pm 9.5\%$, despite a large error associated due a smaller sample size.
- By determining the distance of each star to the cluster centre, it is found that there is no significant trend for binary stars with respect to radius. The best fit for the distribution is a linear fit with a gradient of $(-0.001 \pm 0.003) \text{ arcsec}^{-1}$.
- Potentially, there is a “dip” feature at $\sim 150''$, which may be indicative of a “dynamical clock” effect, however, fitting higher order polynomials could not produce enough of a statistically significant improvement to justify their usage.

Chapter 5

Characterising Identified Binaries

“It is important to draw wisdom from many different places. If you take it from only one place, it become rigid and stale.”

Uncle Iroh - *Avatar: The Last Airbender*

5.1 Binary stars across multiple populations

As discussed in Sec. 1.1.5, the topic of multiple populations is crucial for understanding globular cluster formation and evolution. Binarity across multiple populations also has implications on the evolution and formation of the different populations within their host cluster (Kamann et al., 2020). This is particularly true for ω Cen as, due to its status as a stripped NSC, the cluster hosts a complex chemical composition and a large number of chemically distinct populations, including a large metallicity spread (see discussion in Sec. 1.3).

In order to investigate the significance of metallicity and light element abundances on the binary population of ω Cen, we utilise the $[\text{Fe}/\text{H}]$ measurements determined during the MUSE spectral analysis. We also use the pseudo-colours $\Delta G_{\text{F275W-F814W}}$ (ΔG) and $\Delta C_{\text{F275W-2.F336W+F438W}}$ (ΔC) from Husser et al. (2020), based on work by Milone et al. (2017) (shown in Fig. 1.21), which can be used as proxy for iron abundance and Helium enhancement, and Nitrogen abundance respectively. The pseudo-colours are calculated by tracing the outer edges of the spread of the RGB region, of both the $\text{F275W} - \text{F814W}$ and $\text{F275W} - 2 \cdot \text{F336W} + \text{F438W}$ CMDs respectively, into a blue and red edge. The separation each star in the RGB region from the edges of the spread is then compared, and the pseudo-colour is determined by normalising the colour spread of the RGB region.

Our analysis focuses on the RGB population, a total of 1597¹ stars. Typically, this analysis is only possible with RGB stars, as below the RGB region, the CMD typically becomes a single track rather than a spread due to other regions being less sensitive to light element abundance. We use a photometric approach to detecting multiple populations rather than using chemical abundances calculated from the MUSE spectra, as MUSE spectra are not sensitive to nitrogen variations. Despite having metallicities for the full sample of stars, we limit our analysis to the RGB sample, as the photometric selection is only possible along the RGB. To reduce noise, we apply an SNR cut of 15 to the sample, as this allows for a clearer visual identification of trends.

5.1.1 Binarity as a function of $[\text{Fe}/\text{H}]$

In order to comprehensively investigate separate populations, we choose to initially separate the sample based on MUSE metallicity measurements, as $[\text{Fe}/\text{H}]$ spreads are closely linked to chemical enrichment and galactic evolution, while there are a number of factors that may affect abundance of light elements. In Fig. 5.1, we show the spread

¹1190 stars in the sample are confidently identified as RGB. While the remaining stars lie in intermediate regions between other areas of the CMD, we ensure that all stars in the sample are partially classed as RGB stars.

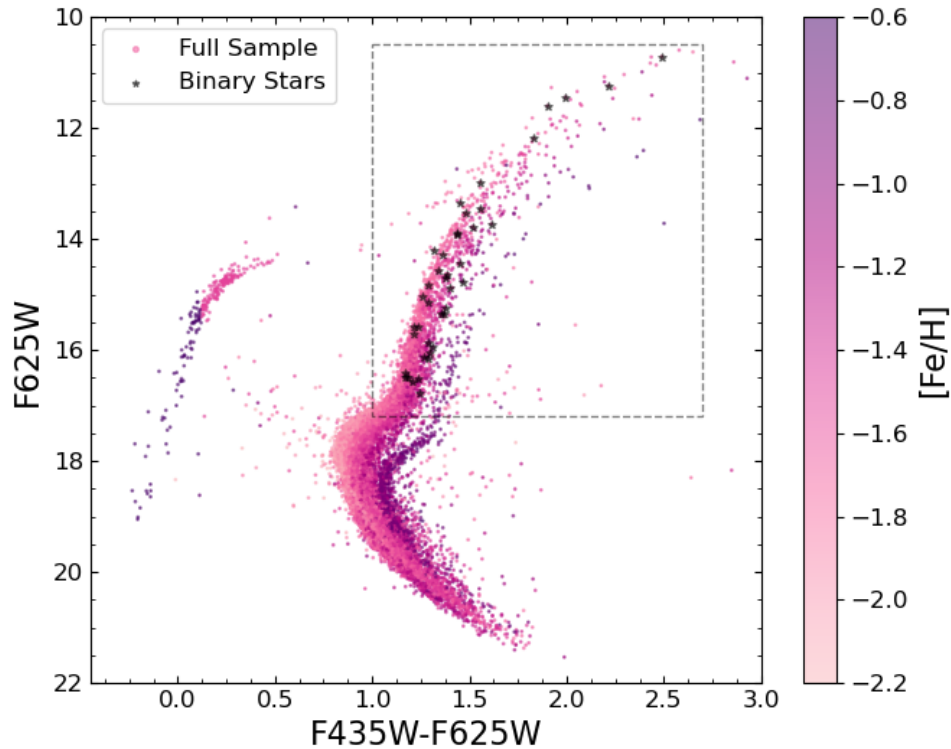


FIGURE 5.1: Stellar metallicity across ω Cen. Both panels show the distribution of stars in the MUSE sample across the colour magnitude diagram (CMD) of the cluster using F625W and F435W magnitude. The main axis shows the metallicity variation across the cluster. We highlight the RGB sample that we focus on in the study with a grey dashed outline, along with the binary systems identified within the RGB sample, indicated by black stars.

of metallicity across the CMD, which shows a clear increase in metallicity for stars on the redder side of the MS, SGB and RGB branches. Also shown within the grey dashed box is the RGB population which will be focused on for the remainder of the study.

We initially plot the distribution of metallicity for the full sample, which is seen in Fig. 5.2. From Fig. 5.2, we see a number of notable features in the metallicity distribution: a large peak at $[\text{Fe}/\text{H}] \approx -1.7$ with further peaks at $[\text{Fe}/\text{H}] \approx -1.5$, -1.1 and -0.8 , which agree with other studies of ω Cen (e.g. Pancino et al., 2000; Johnson & Pilachowski, 2010). These observed peaks are also seen in Fig. 5.1, with the $[\text{Fe}/\text{H}] \approx -0.8$ population seen as a distinct, redder branch of the main sequence and SGB region. When comparing our results to those of Johnson & Pilachowski, we find the peak at $[\text{Fe}/\text{H}] \approx -1.7$ corresponds to their ‘RGB-MP’ population, the peak at $[\text{Fe}/\text{H}] \approx -1.5$ corresponds to their ‘RGB-Int1’ population, the peak at $[\text{Fe}/\text{H}] \approx -1.1$ corresponds to their ‘RGB-Int2+3’ population and the peak at $[\text{Fe}/\text{H}] \approx -0.8$ corresponds to their ‘RGB-a’ population.

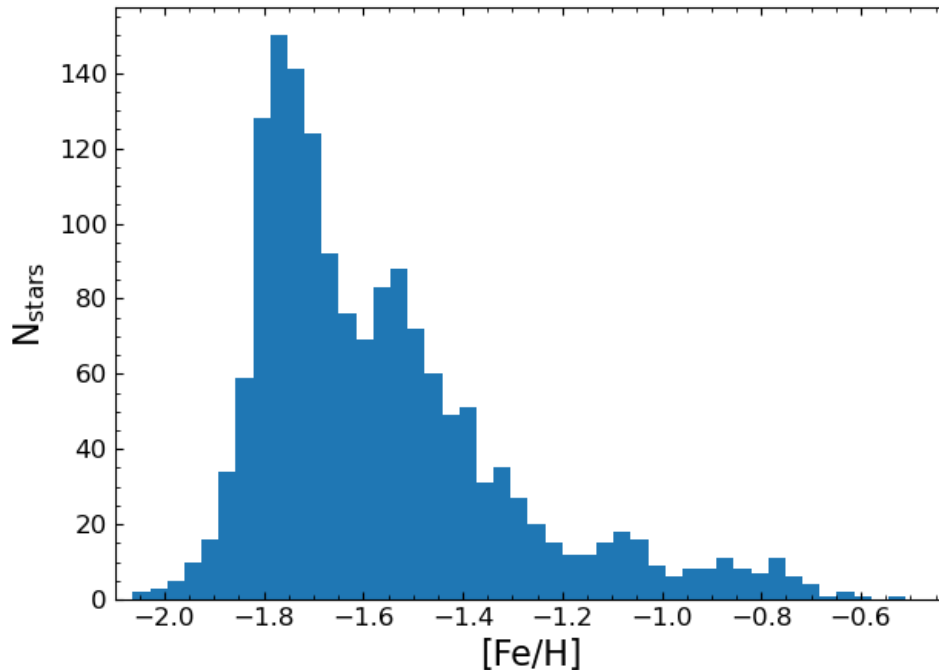


FIGURE 5.2: The distribution of metallicities across the reduced sample of stars. We see a peak at $[\text{Fe}/\text{H}] \approx -1.75$, with smaller peaks at ≈ -1.5 , ≈ -1 and ≈ -0.8

Following this analysis, we then separate the metallicity into our own populations using a Gaussian Mixing Model (GMM) to identify blended Gaussian distributions, which is used in studies such as [Johnson & Pilachowski \(2010\)](#) and [Alvarez Garay et al. \(2024\)](#). To find the optimum number of populations to separate the sample into, we use the Bayes Information Criterion (BIC). Typically, simply increasing the number of Gaussian curves fit to the data will improve the fit, but may lead to overfitting. The BIC is criterion for selecting models which attempts to resolve this by weighting the likelihood of a model fitting with the number of Gaussians in said model. The best fitting model will have the lowest BIC value, as this represents a balance between accurately modelling the populations and overfitting. Using the BIC, we determine that the optimal number of curves to fit to the data is 3. We show the results of the GMM fitting in [Fig. 5.3](#), where we see the distribution of metallicity for the RGB sample along with the normalised histogram showing the three Gaussian models that are fit to the results. We find three peaks in metallicity at $[\text{Fe}/\text{H}] = -1.75 \pm 0.08$, which we refer to as Metal Poor (RGB-MP), $[\text{Fe}/\text{H}] = -1.48 \pm 0.10$, referred to as Intermediate (RGB-I), and $[\text{Fe}/\text{H}] = -1.04 \pm 0.16$, referred to as Metal Rich, (RGB-MR). While the RGB-MP and RGB-I populations are detected in the studies by [Johnson & Pilachowski](#) and [Pancino et al.](#), the RGB-MP population encompasses the RGB-Int2, RGB-Int3 and RGB-a populations reported by [Johnson & Pilachowski](#). As we were unable to deblend these populations effectively,

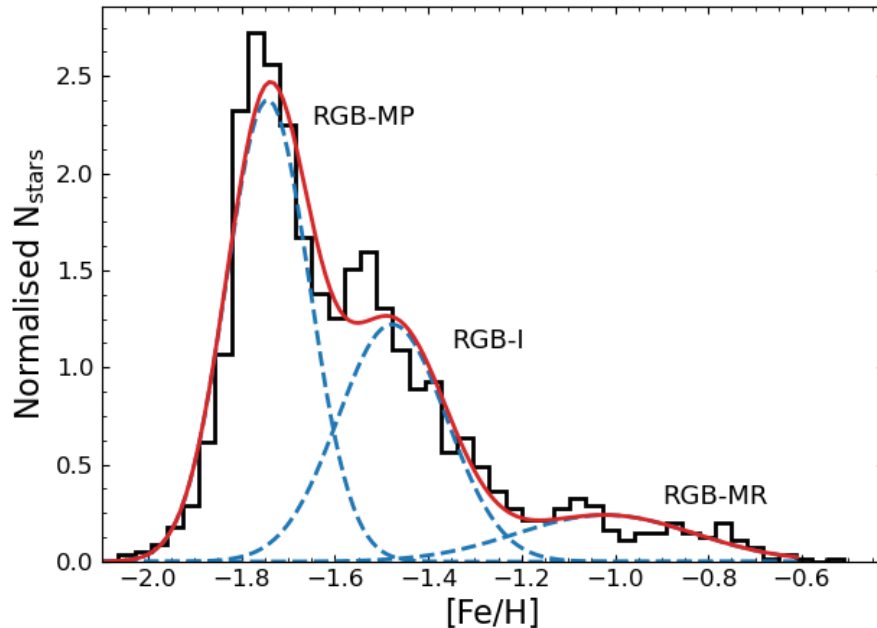


FIGURE 5.3: The normalised distribution of metallicity with three Gaussian mixing models fit. The three mixed models show peaks at $[\text{Fe}/\text{H}] \approx -1.7$, -1.5 and -1.0 .

however, we treat them as one broader population. By determining the probability for each star to belong to each population, we assign stars with a membership probability of 50% or more as a member of the population. We find a total of 860 stars in the RGB-MP population, 566 in the RGB-I population and 170 in the RGB-MR population (see Tab. 5.1 column (c)).

Having separated the sample into $[\text{Fe}/\text{H}]$ populations, we can now investigate the binary fraction across metallicity. We use the mock data set described in Sec. 3.2 to calculate the completeness both globally and for each distinct population. To calculate the overall trend of binary fraction across metallicity, we separate the sample into bins, each containing 200 stars, with increasing metallicity and calculate the average metallicity, completeness and corrected binary fraction for each bin. We show the results of this analysis in Fig. 5.4, along with the best fitting linear gradient and its uncertainty interval. We find a gradient of 1.6 ± 0.9 which, due to the large uncertainty, suggests a that there is no statistically significant ($< 2\sigma$) correlation between metallicity and binary fraction within the cluster for the full population. We note, however, that the statistical robustness of this result is affected by the small sample in each population (as seen in Tab. 5.1 column (d)).

We then split the data into separate metallicity population and calculate the completeness, uncertainty and corrected binary fraction for the RGB-MP, RGB-I and RGB-MR

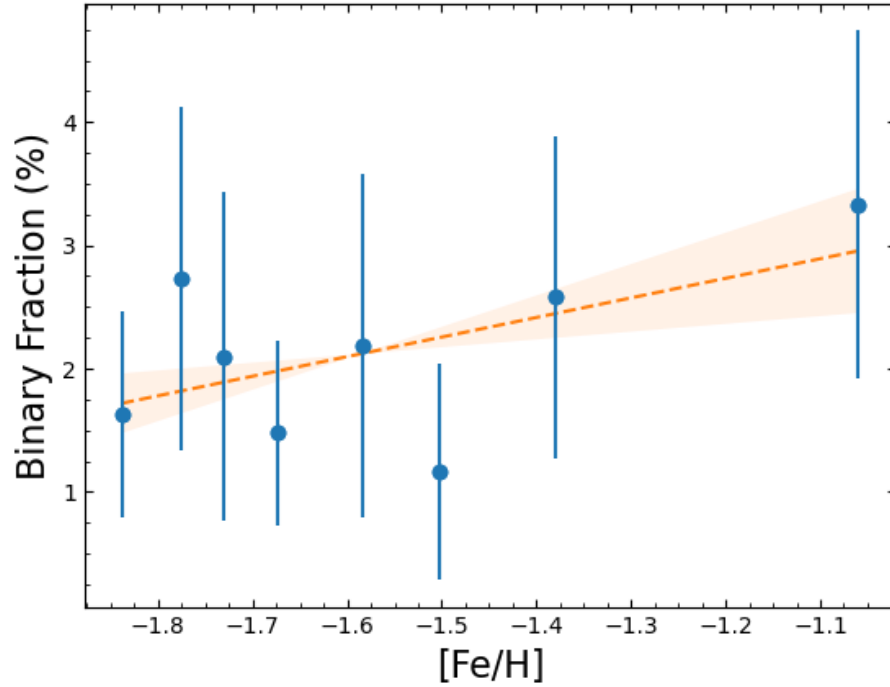


FIGURE 5.4: The binary fraction of ω Cen as a function of metallicity. The best-fitting gradient of the distribution of (1.6 ± 0.9) , shown as a dashed line and the uncertainty as the shaded region, which suggests that any increase in binary fraction is not statistically significant. Each point represents 200 stars.

Pop (a)	σ_{GMM} (b)	$[\text{Fe}/\text{H}]_{\text{Avg}}$ (c)	N_{stars} (d)	N_{binaries} (e)	f_{bin} (f)
RGB-MP	0.09	-1.75 ± 0.08	860	19	$2.3\% \pm 0.6\%$
RGB-I	0.12	-1.48 ± 0.10	566	7	$1.4\% \pm 0.5\%$
RGB-MR	0.19	-1.04 ± 0.16	170	6	$3.9\% \pm 1.6\%$

TABLE 5.1: The binary fraction across the different populations of metallicity. Column (a) shows the identifier for each of the metallicity populations in ω Cen, and corresponding uncertainty is shown in column (b). The average metallicity for each population shown in column (c). Columns (d) and (e) show the total number of stars and the total number of binaries for each metallicity population respectively. Column (f) shows the binary fraction for each population.

populations individually. We see in Fig. 5.5 and Tab. 5.1 a continuation of the results from Fig. 5.4, in that the difference between the binary fraction for each population is within 2σ , and so we conclude that there is no statistically significant trend in binarity across the discrete metallicity populations. We note that for the analysis of binary fraction for both the global metallicity relation and for the separate populations, we find a completeness of over 90%, which is consistent with the high completeness of the RGB population reported in Tab. 3.1.

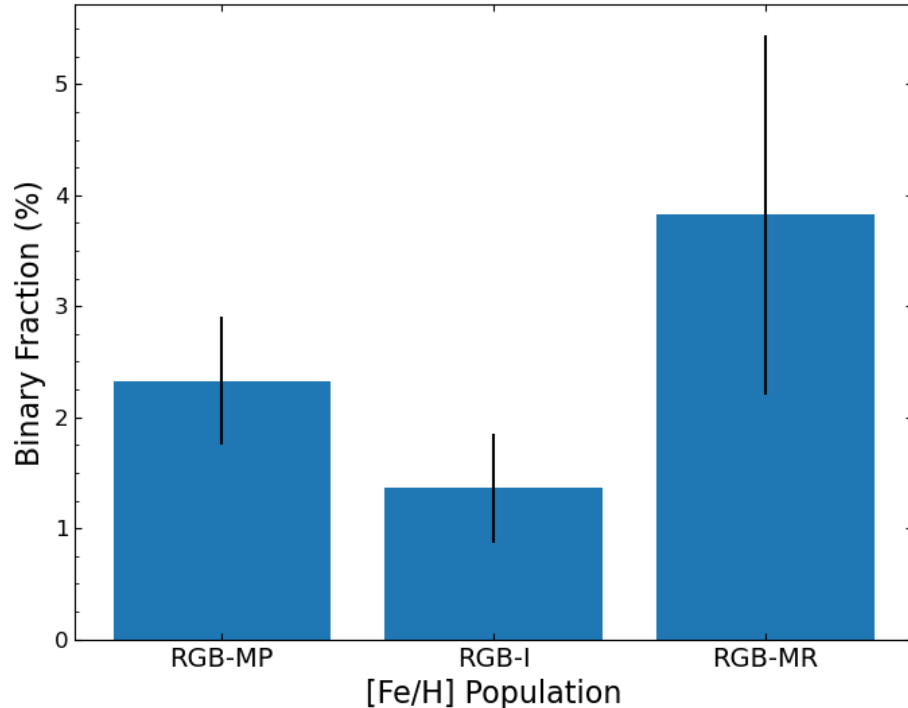


FIGURE 5.5: The binary fraction of each metallicity population: metal poor (RGB-MP), with an average metallicity of -1.75 ± 0.08 , metal intermediate (RGB-I), with an average metallicity of -1.48 ± 0.10 and metal rich (RGB-MR), with an average metallicity of -1.04 ± 0.16 .

5.1.2 Binarity as a function of abundances

We now focus on the light element variance (using ΔC as a proxy for Nitrogen) of ω Cen, and how the binary fraction varies across 1P and 2P populations (see Sec. 1.1.5.1 for discussion). From the chromosome map of ω Cen shown in Fig. 5.6, we see not only a the spread in ΔC , which suggests a spread in light element abundances typical of multiple populations, and the spread in metallicity for both the 1P and 2P populations, discussed in Sec. 5.1.1, but also the additional populations which are characteristic of a Type II cluster (see Sec. 1.1.5 and Fig. 1.21), although ω Cen is an extreme case compared to other clusters (e.g Lee et al., 1999; Pancino et al., 2000; Johnson & Pilachowski, 2010; Milone et al., 2020, see Sec. 1.3).

Similarly to the analysis of the metallicity distribution, we initially plot the distribution of ΔC in Fig. 5.7. We visually identify three clear peaks in abundance, at $\Delta C \approx 0.3$, 0.15 and 0.05, which agrees with the grouping seen in ΔC of Fig. 5.6. The peaks we identify, and the grouping of these populations, is also largely consistent with a recent study by Milone et al. (2020), where our identified population at $\Delta C \approx 0.05$ matches

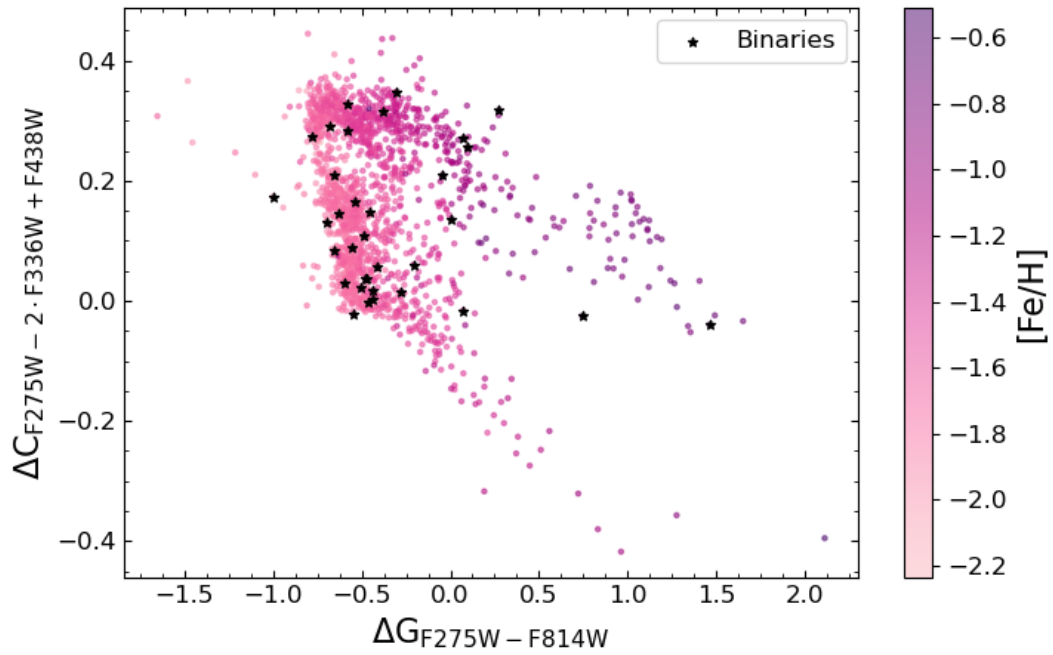


FIGURE 5.6: Chromosome map of ω Cen showing $\Delta C_{F275W-2 \cdot F336W+F438W}$ against $\Delta G_{F275W-F814W}$. We also include a colour bar showing the metallicity of each star for visualisation. The identified binary systems are marked as black stars

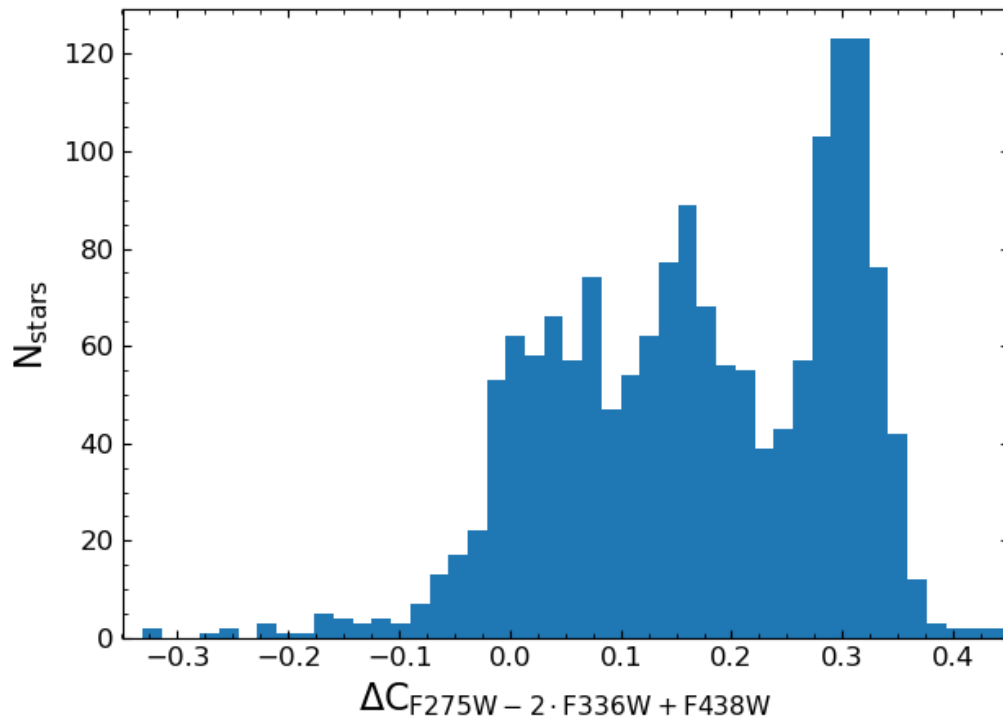


FIGURE 5.7: The distribution of $\Delta C_{F275W-2 \cdot F336W+F438W}$ across the reduced sample. We see several peaks in the data, at $\Delta C \approx 0.30, 0.15$ and 0.05 .

with the identified ‘1G’ population, our identified population at $\Delta C \approx 0.15$ encompasses a combination of their ‘2G_A’ and ‘2G_B’ populations, and our identified population at $\Delta C \approx 0.30$ contains a combination of their ‘2G_C’ and ‘2G_D’ populations. The identified populations at $\Delta C \approx 0.3$, 0.15 and 0.05 also agree with the P1, Int and P2 populations identified by Mason et al. (2024, in prep).

Following this, we apply the GMM technique to the ΔC distribution using the BIC to identify that the most effective number of models to fit is 4, with peaks at $\Delta C \approx 0.30$, 0.16, 0.03 and -0.17 , again using the classification that a star with a probability of 50% or over is labelled as within that population. We choose to apply separate GMMs to the ΔC populations and metallicity populations in order to maintain consistency. An alternative to this approach would be to apply a GMM in 2D, across both ΔC and ΔG , however this results in similar populations to those seen in Sec. 5.1.3. We also choose separate 1D GMMs rather than a 2D fit as the metallicity measurements derived from the MUSE spectra are more robust than the ΔG pseudo colour. We fit the models to the data seen in Fig. 5.8, which shows the normalised distribution, with the 4 Gaussian curves overlaid. We label the three viable populations based on each relative abundance. The $\Delta C \approx 0.03$ population is referred to as RGB-1 and likely represents the 1P population of ω Cen, while the $\Delta C \approx 0.16$ population and the $\Delta C \approx 0.30$ population, henceforth referred to as RGB-2 and RGB-3 respectively, likely represent the 2P population of stars (see Sec. 1.1.5). We note that we do not consider the unlabelled fourth curve at $\Delta C \approx -0.17$, due to a particularly small sample size. When investigating this population on the chromosome map of Fig. 5.6, we see that this population is the extension of the tail of the 1P population due to intrinsic metallicity and helium spread.

Having identified the separate populations within the cluster, we now investigate the binary fraction across ΔC variation, using a similar analysis as used for metallicity. We initially investigate the global trend of binary fraction, by analysing the stars in bins each containing 200 stars and calculating an average ΔC , sample completeness and corrected binary fraction for each bin. The results of this analysis are shown in Fig. 5.9 along with the best fitting linear gradient, where we see a negative correlation between ΔC and binary fraction with a gradient of -4.8 ± 2.9 . Although the negative gradient is consistent with the general trend that 1P stars have a higher binary fraction than 2P stars (Lucatello et al., 2015; Dalessandro et al., 2018; Kamann et al., 2020, see Sec. 1.1.5.1 for discussion), the large errors mean that this result cannot be considered statistically robust and so we conclude that there is no clear trend in binarity between ΔC populations, and therefore between 1P and 2P populations. This result is, again, likely affected by the small number of stars in the sample.

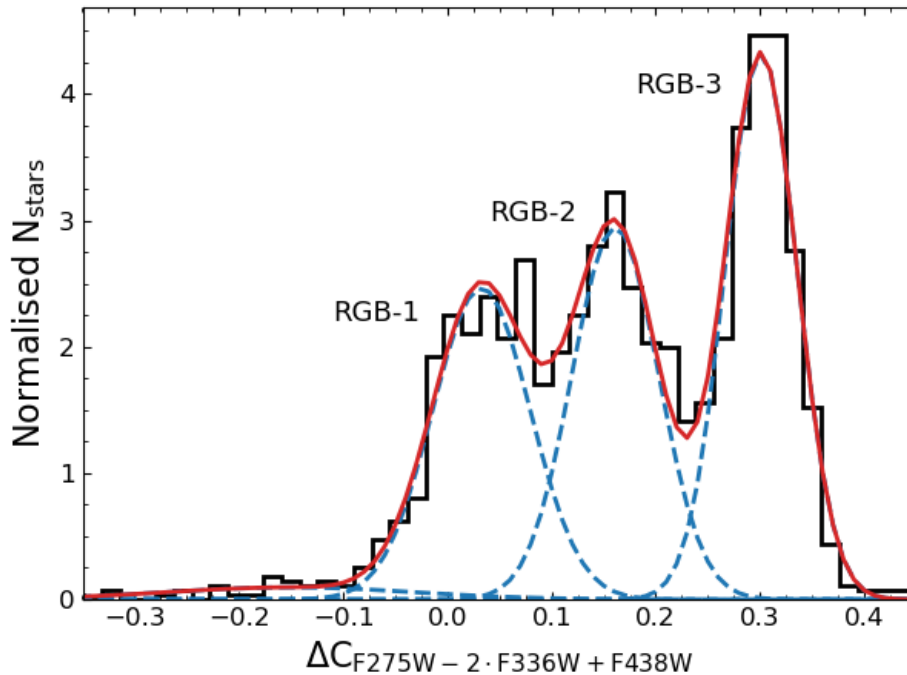


FIGURE 5.8: The GMM splitting for ΔC variation. We see 4 peaks, at $\Delta C \approx 0.3$, 0.16 and 0.03. We disregard the fourth population with a peak at $\Delta C \approx -0.15$, as this population is dominated by small numbers.

Pop (a)	ΔC_{Avg} (b)	N_{stars} (c)	N_{binaries} (d)	f_{bin} (e)
RGB-1	0.03	472	14	$3.2\% \pm 0.8\%$
RGB-2	0.16	491	9	$1.9\% \pm 0.7\%$
RGB-3	0.30	600	9	$1.6\% \pm 0.6\%$

TABLE 5.2: The binary fraction across the different ΔC populations. Column (a) shows the identifier for each of the population in ω Cen, with the average $\Delta C_{F275W-2 \cdot F336W+F438W}$ for each population shown in column (b). Columns (c) and (d) show the total number of stars and the total number of binaries for each population respectively. Column (e) shows the binary fraction for each population.

We then calculate the binary fraction for each discrete population using the GMM tag predictions. We calculate a correction factor for each population and apply this to calculate a corrected binary fraction. These results are shown in Fig. 5.10 and in Tab. 5.2, though we, again, see no statistically significant trend in binary fraction between the ΔC populations in ω Cen. Similar to the metallicity results, however, the large uncertainties are likely a result of the small sample size of each population. It is important to note that, as discussed in Sec. 1.1.5 and Sec. 1.3, due to the complexity of ω Cen and the lack of studies of Type II clusters, the distribution of binaries in more complex clusters may differ compared to trends seen in Type I clusters. This will be discussed further in Sec. 5.1.3.

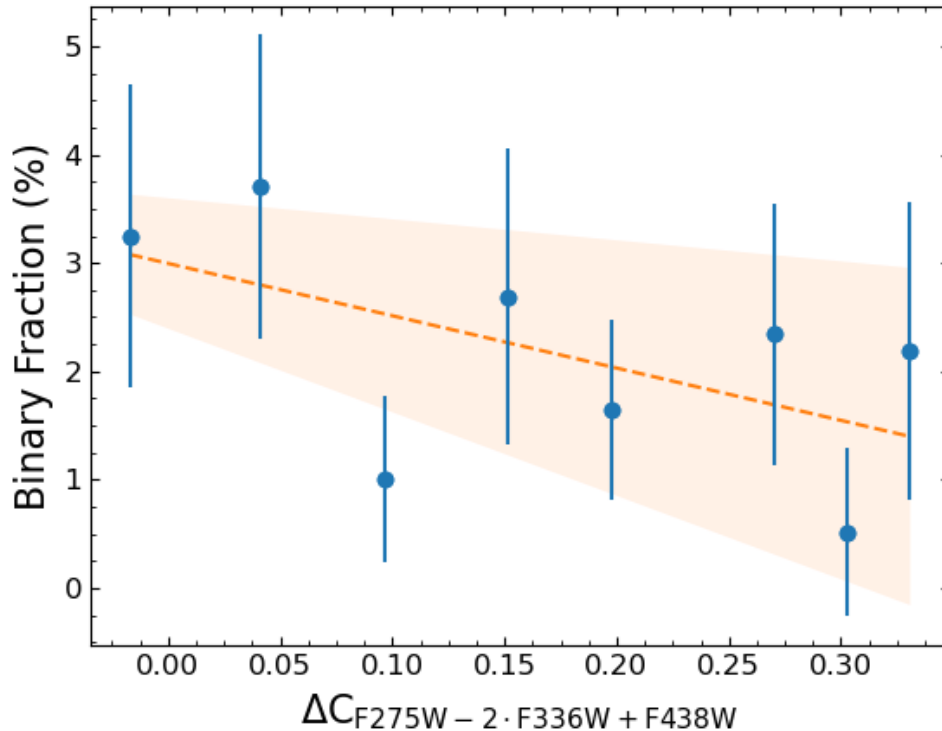


FIGURE 5.9: The binary fraction of ω Cen as a function of ΔC , with the data binned in such a way that one point represents 200 stars. We find the best-fitting gradient of the distribution to (-4.8 ± 2.9) , shown as a dashed line and the uncertainty shaded in orange, which suggests no statistically significant trend.

5.1.3 Separation into populations

Having separated the stars in ω Cen based on metallicity spread, and also into multiple populations through ΔC variation, we can now investigate the binarity across the different populations of the cluster. In order to separate the cluster into populations, we split the sample into each of the identified ΔC populations (prefixed ‘RGB1’, ‘RGB2’ and ‘RGB3’, see Sec. 5.1.2) and then into metallicity groups (suffix ‘-MP’, ‘-I’ and ‘-MR’, see Sec. 5.1.1), resulting in 9 distinct populations (see Tab. 5.3). The 9 separated populations are marked in Fig. 5.11, displayed through a chromosome map of ω Cen, similar to Fig. 5.6. It is important to note that the low ΔC , high ΔG tail seen in Fig. 5.6 is removed in Fig. 5.11, as this is separated through the ΔC GMM fitting process into the $\Delta C \approx -0.17$ population that is removed from the analysis.

Having separated the RGB sample into distinct populations, we then calculate the binary fraction for each of the multiple populations to determine if there is any trend between individual populations of ω Cen. When calculating the binary fraction of each population, we use the correction factor which was calculated for the full RGB

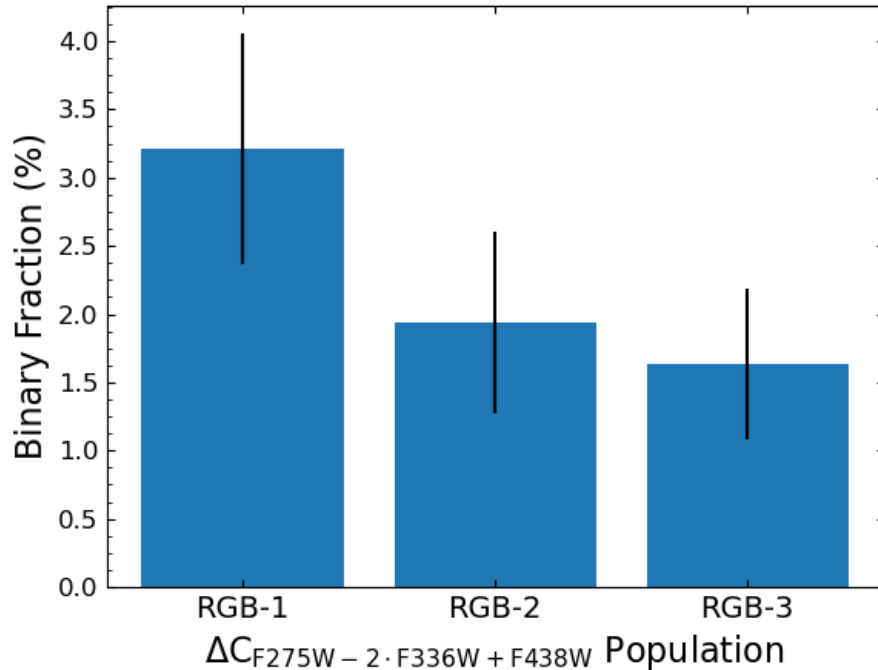


FIGURE 5.10: Binary probability for each of the three main populations. We see a higher fraction in the lowest ΔC (low light element abundance) population RGB-1, which decreases as ΔC increases, however there is no statistically significant variation in binary fraction.

population, 0.9 ± 0.1 , to avoid large uncertainties on the correction factor. We make this assumption as the correction factors used throughout this analysis are consistently within the uncertainty of the completeness of the full RGB population. We show the binary fractions of each population in Tab. 5.3, however, from the binary analysis of each population, similar to the results from Sec. 5.1.1 and Sec. 5.1.2, we see no statistically significant increase of binary fraction between any of the populations in ω Cen. Again, the lack of statistical significance is likely due to the the small sample of stars in each population (see columns (b) and (c) Tab. 5.3).

While the lack of clear trends throughout this investigation have been largely due to the small numbers of stars in each sample, there are some theoretical reasons that a more homogeneous binary fraction may be observed for 1P and 2P stars in ω Cen. Simulations such as Hong et al. (2015) suggest that, as 2P stars are typically located closer to the centre of the cluster than 1P stars, a lower binary fraction of 2P stars may in part be caused by a higher rate of disruption due to the higher density of stars in the cluster. This may conversely suggest that if populations have less of a separation in radial distribution, there may be a less pronounced difference between their respective binary fractions. To investigate this, we plot the distribution of distance from the cluster centre of each population, calculated using the location of the cluster centre from

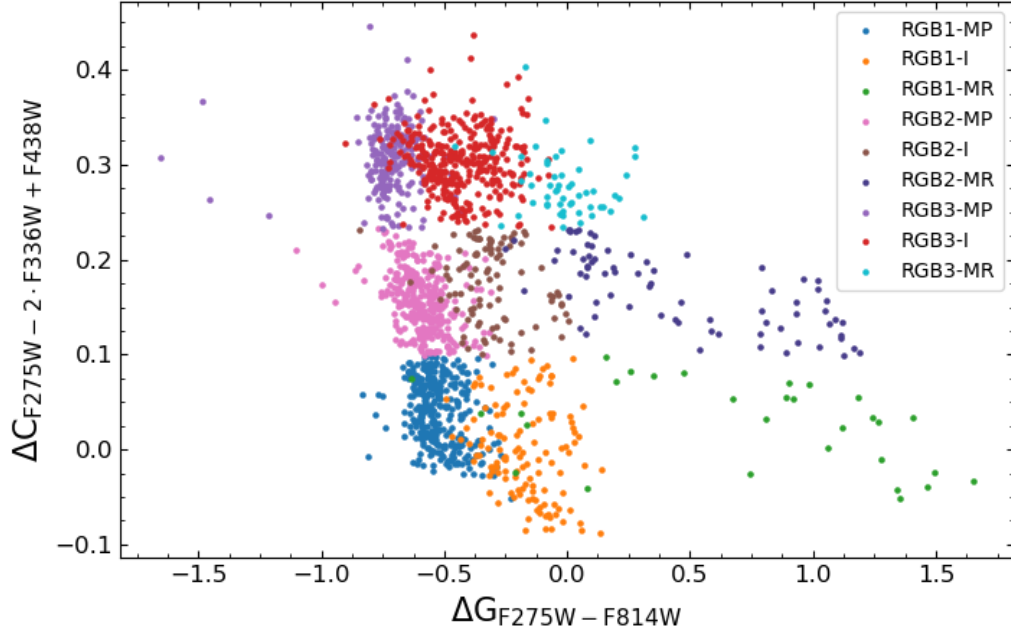


FIGURE 5.11: Chromosome map of ω Cen showing the pseudo colour $\Delta C_{F275W-2 \cdot F336W+F438W}$ against $\Delta G_{F275W-F814W}$. We mark in colour the discrete populations we identify using a GMM for both metallicity and ΔC variation. The first part of each population tag (e.g. RGB1, see Sec. 5.1.2) denotes the grouping by ΔC , while the second part of the tag (e.g. MP, see Sec. 5.1.1) denotes the grouping by metallicity. For the full list of populations, see Tab. 5.3.

Population (a)	N_{stars} (b)	N_{binaries} (c)	Binary Fraction (d)
RGB1-MP	317	9	$3.0\% \pm 1.2\%$
RGB1-I	125	3	$2.5\% \pm 1.3\%$
RGB1-MR	30	2	$7.0\% \pm 5.3\%$
RGB2-MP	319	6	$2.0\% \pm 0.8\%$
RGB2-I	97	2	$2.2\% \pm 1.6\%$
RGB2-MR	74	1	$1.4\% \pm 2.1\%$
RGB3-MP	223	4	$1.9\% \pm 1.2\%$
RGB3-I	324	2	$0.7\% \pm 0.5\%$
RGB3-MR	53	3	$6.0\% \pm 3.0\%$

TABLE 5.3: The binary fraction across the different populations of stars. Column (a) shows the identifier for each of the populations we identify in ω Cen. Columns (b) and (c) show the total number of stars and the total number of binaries for each population respectively. Column (d) shows the binary fraction for each population.

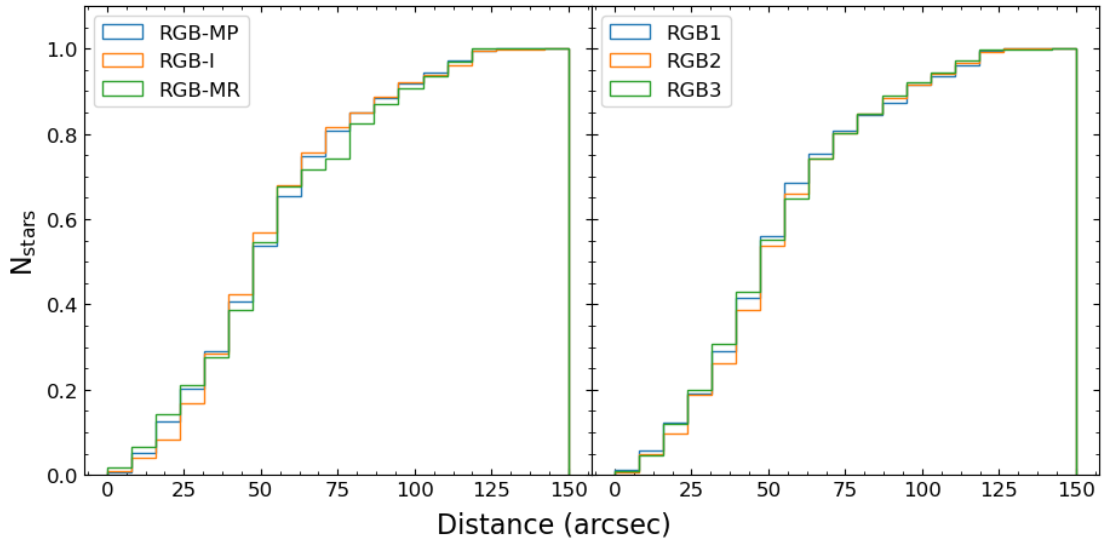


FIGURE 5.12: The normalised and cumulative radial distribution of each of the separated populations. On the left panel, we show the distribution of the metallicity separated populations, while the right panel shows the distribution for the populations separated by ΔC . We see little change in the radial distribution of populations for either parameter, with each of the population distributions within 2σ of each other.

Anderson & van der Marel (2010), the results of which are shown in Fig. 5.12. From the normalised distributions, and by performing a Kolmogorov-Smirnov (KS) test, we see little separation between the different populations in the cluster, with the median separation from the cluster centre for each metallicity and ΔC population within 2σ of each other. Given that the typical trends in multiple population radial distribution are not observed within the cluster, this may explain why we see little statistically significant variation in the binary fraction. We note, however, that the results by Hong et al. (2015) are for the initial distribution of 1P and 2P stars and that for ω Cen, it may be the case that primordial distributions have been erased by relaxation.

5.2 Summary

- A total of three metallicity populations were detected using a GMM: a metal poor population containing 860 star with a peak metallicity -1.75 ± 0.08 , a metal intermediate population containing 566 stars with a peak metallicity -1.48 ± 0.10 , and a metal rich population containing 170 stars with a peak metallicity of -1.04 ± 0.16 .
- Although the binary fraction appears to increase in the metal rich population, we find that there is no statistically significant trend in the binary fraction for the metallicity populations.

- Similarly to the investigation of metallicity, the cluster was split into three sub populations based on the pseudo colour light element abundance (particularly sensitive to Na abundance) using a GMM. We find a 1P population of 472 stars, and two 2P populations, with 491 and 600 stars respectively.
- By completing a similar analysis on this population as to the metallicity populations we find that, though the binary fraction appears to decrease as light element abundance increases, no statistically significant trend is found for the light element sub populations.
- We then combined the metallicity and light element populations and split the RGB region of ω Cen into 9 chemically distinct populations.
- We find no statistically significant trend in binary fraction was detected across any of groups, and no statistically significant trend in spatial distribution was found for either the metallicity or ΔC (as a proxy for light element abundance) sub populations. This may indicate that the cluster relaxation has erased the initial distribution of binary systems.
- It is important to note that the sample size of stars within each of the populations was consistently low and that it is the main contributor to uncertainties.

Chapter 6

Conclusions and Future Outlook

“I’d just like to say, thank you very much. Yes, I’m getting the hell out of here, yes, I am - bye bye.”

Kevin Ayers - *Stranger in Blue Suede Shoes*

6.1 Conclusions

In conclusion, using MUSE data, we have been able to constrain the number of binary systems within the half light radius of ω Cen. We have then created mock data sets to determine the completeness of our sample, and tested the sensitivity of the completeness correction on the assumed distributions of orbital parameters by varying each parameter over a wide range of values. We then combine these two elements to calculate a corrected binary fraction. Having identified the binary systems in the cluster, we then divide the RGB region of the CMD into 9 separate populations. This was done with a Gaussian mixing model (GMM), which used the spectroscopic metallicities and a photometric pseudo colour, which can be treated as a proxy for light element abundances, as input. We then compare the binary fraction for both light element abundance and metallicity, and the 9 populations as a whole in order to determine if there is any significant trend in binary fractions for the different populations of ω Cen. In summary:

- From the initial set of MUSE data, we have matched the MUSE sample with catalogues from [Clement et al. \(2001\)](#) and [Braga et al. \(2020\)](#) to remove previously reported photometric variables. In total, we remove 22 reported photometric variables, along with 912 stars that are identified as photometrically variable as part of the MUSE spectral analysis.
- We have created a mock set of data for ω Cen using randomly generated orbital parameters. The samples contained a set number of binary systems with known binary parameters in order to effectively test the completeness of the sample and calculate a corrected binary fraction of ω Cen.
- The completeness of the sample was found to be 0.7 ± 0.1 . This correction factor allows us to minimise the number of false positive detections to $< 5\%$ of the detected binary population (approximately 2σ).
- We have calculated that the global discovery fraction of ω Cen is $1.4 \pm 0.1\%$, calculated using the statistical method presented by [Giesers et al. \(2019\)](#). We limit our sample to stars with a minimum of 6 epochs, and only considering stars with a variability probability value of 0.8 in order to minimise false positives. In total, we find 275 likely binary systems from a sample of 19059 stars.
- By adjusting the discovery fraction with the completeness factor, we compute a global binary fraction of $2.1\% \pm 0.4\%$. This result agrees with the limit of 5% from [Elson et al. \(1995\)](#) and the photometric estimate of $2.70 \pm 0.08\%$ derived in [Bellini et al. \(2017\)](#).

- From individual analysis of areas of the CMD, we find an increased binary fraction of stars in the BSS region of the CMD, at $21.9\% \pm 9.5\%$. The increased discovery and binary fraction on the BSS branch supports the scenario that BSS evolution is linked to binary star evolution.
- By investigating how the binary fraction of ω Cen evolves with radius, we find no radial trend, which is consistent with limited mass segregation (Watkins et al., 2022; Baumgardt et al., 2023)
- Using a GMM to identify groups within element abundance spreads, the population of ω Cen was split into 9 chemically distinct populations, a metal rich, metal intermediate and metal poor population, and three populations based on sodium abundance.
- There was no statistically significant change in the binary fraction or in the spatial distributions for any of the metallicity and light element abundance sub populations. While this in part is due to the small numbers of binary stars present within each sub population, given the relatively large sample, it is reasonable to conclude that there is no spike in the binary fraction for any of the 9 separate populations.

6.2 Future work

6.2.1 Studies of ω Cen

A sample of identified binaries and a well constrained binary fraction is essential to further studies of ω Cen. A follow up study being undertaken (Saracino et al., in prep.) is to fit orbital parameters to radial velocity measurements of stars in ω Cen (an example of which is seen in Fig. 1.24 in Sec. 1.4.1). This work uses the Monte Carlo based sampler THE JOKER (Price-Whelan et al., 2017) and nested sampling algorithm ULTRANEST (Buchner, 2021) to fit Keplerian orbits to the velocity measurements of each system, resulting in confidently constrained orbital properties for a fraction of identified binary system (typically $\sim 10\%$ can be constrained). This method is similar to the work on NGC 3201 by Giesers et al. (2018), which resulted in a total of 3 stellar mass black hole companion candidates (Giesers et al., 2018, 2019). By applying these methods to ω Cen, it becomes possible to identify black holes in the cluster, and help provide constraints on the number and mass of black holes in the cluster, which is particularly important given the potential for the cluster to host an intermediate mass black hole (IMBH). The binary fraction, not only the global fraction and fractions for regions of the CMD, but also trends across multiple populations, is also an invaluable tool for dedicated models.

As discussed in Sec. 1.1.4, binary systems are a crucial factor of cluster evolution, and so dedicated models of ω Cen must be able to reasonably reproduce the binary fraction observed today in order to be considered an effective and realistic model of the cluster's evolution. Successfully modelling a cluster as unusual and complex as ω Cen would be immensely beneficial to the field, as this may provide evidence as to how nuclear star clusters (NSCs) form in their host galaxies, and the effects that galaxy mergers have on the population within a merging galaxy's nucleus.

Dedicated simulations could also be used to further improve the calculation of the completeness discussed in Sec. 3.2. Although all assumptions that have been made are physically justified, we appreciate that they will introduce some limitations. For example, due to the long orbital period, our generated sample would label the binary systems with invisible companions detected by [Platais et al. \(2024\)](#) as soft binaries and remove them from the sample, however the detection of these systems suggests that binaries that are classed as soft may be able to survive within ω Cen. Further testing of the velocity dispersion assumptions would yield a more robust completeness, as our results may represent a slight overestimation.

6.2.2 Applications to other clusters

This method has applications to other globular clusters. As the simulation that was created to generate mock data is not a dedicated model of ω Cen, it is possible to generate a representative suite of mock MUSE data samples for any cluster, provided that there are estimates for the parameter distributions (e.g period distribution) within the cluster. There have already been some studies that have used a similar method to detect variable stars (e.g [Giesers et al., 2019](#); [Saracino et al., 2023](#)), and upcoming studies include investigating the binary fraction of 47 Tuc ([Müller-Horn et al., in prep](#)). Given the large sample of globular clusters in the MUSE Galactic Globular Cluster survey, however, it is possible to catalogue the binary fractions of a large sample of Milky Way globular clusters. By cataloguing the binary fractions of globular clusters and investigating the binary population to determine orbital parameters, it is possible to gain further insight into the demographics of binary stars and globular clusters within the Milky Way.

6.2.3 Future observations

Using MUSE, and the data collected by MUSE, there are a number of techniques that can further the studies of globular clusters. Naturally, more observations using MUSE and a greater number of epochs for the stars in the sample would allow for a better

constrained binary fraction. Combining proper motion (PM) measurements (e.g from *Hubble*), which can be used to identify binary systems through astrometric wobble (see Sec. 1.4.1), with radial velocity measurements may also provide an exciting opportunity to determine binary orbits in 3D space (Platais et al., 2024). Given that PM studies require long term monitoring of clusters, this will likely become more feasible over the coming years.

There are a number of milestones that will be able to further the field of globular cluster analysis. The release of *Gaia* data release (DR4) provides an exciting advancement, as DR4 will provide a large sample of RV curves for stars in the Milky Way. Data from *Gaia* DR3 have already been able to detect a total of 2 black holes in binary systems with luminous stars (El-Badry et al., 2023a,b), and radial velocity data gathered in preparation for DR4 have already been used to detect another black hole (Gaia Collaboration et al., 2024).

There are also a number of planned instruments that will provide further ground based observations. BlueMUSE (Richard et al., 2019) is a integral field spectrograph, similar to MUSE that will be installed at the VLT, with a number of improvements that allow for new science cases. BlueMUSE will have a wavelength coverage of 350 - 580 nm, which means the instrument is optimised to bluer light compared to the 475 - 935 nm range of MUSE and a larger field of view (> 1 arcmin²). This will not only allow for further study of dense stellar environments, such as globular clusters, but also understanding multiple populations within globular clusters by measuring element abundances that are currently outside of the MUSE wavelength coverage. BlueMUSE will also be able to investigate massive stars within our Galaxy, as massive stars in binary or multiple systems may represent progenitors for black hole binary systems. Another ground based instrument is HARMONI (Tecza et al., 2009) which will be installed at the ELT. HARMONI is a high angular resolution optical and Near-Infrared (NIR) IFU, covering 470 - 2450 nm. The high angular resolution of HARMONI provides an exciting opportunity to study stars in dense stellar environments, such as star cluster populations of more distant galaxies.

Bibliography

- Abbott B. P., et al., 2016, *Physical Review Letters*, 116, 061102
- Abbott R., et al., 2020, *Physical Review Letters*, 125, 101102
- Adamo A., Östlin G., Zackrisson E., 2011, *Monthly Notices of the Royal Astronomical Society*, 417, 1904
- Afanasiev A. V., et al., 2018, *Monthly Notices of the Royal Astronomical Society*, 477, 4856
- Ahn C. P., et al., 2017, *The Astrophysical Journal*, 839, 72
- Ahn C. P., et al., 2018, *The Astrophysical Journal*, 858, 102
- Akiyama K., 2020, in *American Astronomical Society Meeting Abstracts #235*. p. 429.03
- Alvarez Garay D. A., Mucciarelli A., Bellazzini M., Lardo C., Ventura P., 2024, *Astronomy & Astrophysics*, 681, A54
- Anderson J., van der Marel R. P., 2010, *The Astrophysical Journal*, 710, 1032
- Anderson J., et al., 2008, *The Astronomical Journal*, 135, 2055
- Antonini F., Gieles M., 2020, *Physical Review D*, 102, 123016
- Antonini F., Capuzzo-Dolcetta R., Mastrobuono-Battisti A., Merritt D., 2012, *The Astrophysical Journal*, 750, 111
- Antonini F., Barausse E., Silk J., 2015, *The Astrophysical Journal*, 812, 72
- Antonini F., Chatterjee S., Rodriguez C. L., Morscher M., Pattabiraman B., Kalogera V., Rasio F. A., 2016, *The Astrophysical Journal*, 816, 65
- Antonini F., Gieles M., Gualandris A., 2019, *Monthly Notices of the Royal Astronomical Society*, 486, 5008
- Aros F. I., Vesperini E., 2023, *Monthly Notices of the Royal Astronomical Society*, 525, 3136

- Aros F. I., Sippel A. C., Mastrobuono-Battisti A., Bianchini P., Askar A., van de Ven G., 2021, *Monthly Notices of the Royal Astronomical Society*, 508, 4385
- Askar A., Arca Sedda M., Giersz M., 2018, *Monthly Notices of the Royal Astronomical Society*, 478, 1844
- Askar A., Davies M. B., Church R. P., 2021, *Monthly Notices of the Royal Astronomical Society*, 502, 2682
- Askar A., Baldassare V. F., Mezcuca M., 2023, arXiv e-prints, p. arXiv:2311.12118
- Atri P., et al., 2019, *Monthly Notices of the Royal Astronomical Society*, 489, 3116
- Bacon R., et al., 2010, in McLean I. S., Ramsay S. K., Takami H., eds, *Society of Photo-Optical Instrumentation Engineers (SPIE) Conference Series Vol. 7735, Ground-based and Airborne Instrumentation for Astronomy III*. p. 773508 ([arXiv:2211.16795](https://arxiv.org/abs/2211.16795)), doi:10.1117/12.856027
- Bacon R., et al., 2023, *The Messenger*, 191, 11
- Bailyn C. D., 1995, *Annual Review of Astronomy and Astrophysics*, 33, 133
- Banyard G., Sana H., Mahy L., Bodensteiner J., Villaseñor J. I., Evans C. J., 2022, *Astronomy & Astrophysics*, 658, A69
- Bastian N., Lardo C., 2018, *Annual Review of Astronomy and Astrophysics*, 56, 83
- Bastian N., Saglia R. P., Goudfrooij P., Kissler-Patig M., Maraston C., Schweizer F., Zoccali M., 2006, *Astronomy & Astrophysics*, 448, 881
- Bastian N., Lamers H. J. G. L. M., de Mink S. E., Longmore S. N., Goodwin S. P., Gieles M., 2013, *Monthly Notices of the Royal Astronomical Society*, 436, 2398
- Baumgardt H., 2017, *Monthly Notices of the Royal Astronomical Society*, 464, 2174
- Baumgardt H., Hilker M., 2018, *Monthly Notices of the Royal Astronomical Society*, 478, 1520
- Baumgardt H., Sollima S., 2017, *Monthly Notices of the Royal Astronomical Society*, 472, 744
- Baumgardt H., et al., 2019, *Monthly Notices of the Royal Astronomical Society*, 488, 5340
- Baumgardt H., Hénault-Brunet V., Dickson N., Sollima A., 2023, *Monthly Notices of the Royal Astronomical Society*, 521, 3991
- Becklin E. E., Neugebauer G., 1968, *The Astrophysical Journal*, 151, 145

- Bekki K., Freeman K. C., 2003, *Monthly Notices of the Royal Astronomical Society*, 346, L11
- Bellini A., Milone A. P., Anderson J., Marino A. F., Piotto G., van der Marel R. P., Bedin L. R., King I. R., 2017, *The Astrophysical Journal*, 844, 164
- Bender R., et al., 2005, *The Astrophysical Journal*, 631, 280
- Binney J., Tremaine S., 2008, *Galactic Dynamics: Second Edition*
- Bodensteiner J., et al., 2020, *Astronomy & Astrophysics*, 634, A51
- Bodensteiner J., et al., 2021, *Astronomy & Astrophysics*, 652, A70
- Böker T., Sarzi M., McLaughlin D. E., van der Marel R. P., Rix H.-W., Ho L. C., Shields J. C., 2004, *The Astronomical Journal*, 127, 105
- Bombaci I., 1996, *Astronomy & Astrophysics*, 305, 871
- Braga V. F., et al., 2020, *Astronomy & Astrophysics*, 644, A95
- Breen P. G., Heggie D. C., 2012, *Monthly Notices of the Royal Astronomical Society*, 420, 309
- Bressan A., Marigo P., Girardi L., Salasnich B., Dal Cero C., Rubele S., Nanni A., 2012, *Monthly Notices of the Royal Astronomical Society*, 427, 127
- Buchner J., 2021, *The Journal of Open Source Software*, 6, 3001
- Cadelano M., Dalessandro E., Vesperini E., 2024, arXiv e-prints, p. arXiv:2402.09514
- Carroll B. W., Ostlie D. A., 2017, *An Introduction to Modern Astrophysics*. Cambridge University Press
- Cen R., 2001, *The Astrophysical Journal*, 560, 592
- Chomiuk L., Strader J., Maccarone T. J., Miller-Jones J. C. A., Heinke C., Noyola E., Seth A. C., Ransom S., 2013, *The Astrophysical Journal*, 777, 69
- Clement C. M., et al., 2001, *The Astronomical Journal*, 122, 2587
- Cohen R. E., Sarajedini A., 2012, *Monthly Notices of the Royal Astronomical Society*, 419, 342
- Cordero M. J., Pilachowski C. A., Johnson C. I., McDonald I., Zijlstra A. A., Simmerer J., 2014, *The Astrophysical Journal*, 780, 94
- Cordoni G., et al., 2023, *Astronomy & Astrophysics*, 672, A29

- Cottrell P. L., Da Costa G. S., 1981, *Astrophysical Journal, Letters*, 245, L79
- D'Ercole A., Vesperini E., D'Antona F., McMillan S. L. W., Recchi S., 2008, *Monthly Notices of the Royal Astronomical Society*, 391, 825
- Dabringhausen J., Hilker M., Kroupa P., 2008, *Monthly Notices of the Royal Astronomical Society*, 386, 864
- Dalessandro E., Ferraro F. R., Massari D., Lanzoni B., Mocchi P., Beccari G., 2015, *The Astrophysical Journal*, 810, 40
- Dalessandro E., et al., 2018, *The Astrophysical Journal*, 864, 33
- Dalessandro E., et al., 2019, *Astrophysical Journal, Letters*, 884, L24
- Dantona F., Gratton R., Chieffi A., 1983, *Mem. Societa Astronomica Italiana*, 54, 173
- Decressin T., Meynet G., Charbonnel C., Prantzos N., Ekström S., 2007, *Astronomy & Astrophysics*, 464, 1029
- Denissenkov P. A., Hartwick F. D. A., 2014, *Monthly Notices of the Royal Astronomical Society*, 437, L21
- Do T., Kerzendorf W., Winsor N., Støstad M., Morris M. R., Lu J. R., Ghez A. M., 2015, *The Astrophysical Journal*, 809, 143
- Dondoglio E., Milone A. P., Lagioia E. P., Marino A. F., Tailo M., Cordini G., Jang S., Carlos M., 2021, *The Astrophysical Journal*, 906, 76
- Drinkwater M. J., Jones J. B., Gregg M. D., Phillipps S., 2000, *Publications of the Astron. Soc. of Australia*, 17, 227
- Duchêne G., Kraus A., 2013, *Annual Review of Astronomy and Astrophysics*, 51, 269
- Dunstall P. R., et al., 2015, *Astronomy & Astrophysics*, 580, A93
- Duquennoy A., Mayor M., 1991, *Astronomy & Astrophysics*, 248, 485
- Eggleton P. P., 1983, *The Astrophysical Journal*, 268, 368
- El-Badry K., Burdge K. B., 2022, *Monthly Notices of the Royal Astronomical Society*, 511, 24
- El-Badry K., et al., 2023a, *Monthly Notices of the Royal Astronomical Society*, 518, 1057
- El-Badry K., et al., 2023b, *Monthly Notices of the Royal Astronomical Society*, 521, 4323

- Elmegreen B. G., Falgarone E., 1996, *The Astrophysical Journal*, 471, 816
- Elson R. A. W., Gilmore G. F., Santiago B. X., Casertano S., 1995, *The Astronomical Journal*, 110, 682
- Fall S. M., Rees M. J., 1985, *The Astrophysical Journal*, 298, 18
- Fall S. M., Zhang Q., 2001, *The Astrophysical Journal*, 561, 751
- Feldmeier-Krause A., Zhu L., Neumayer N., van de Ven G., de Zeeuw P. T., Schödel R., 2017, *Monthly Notices of the Royal Astronomical Society*, 466, 4040
- Ferraro F. R., Lanzoni B., 2009, in *Revista Mexicana de Astronomia y Astrofisica Conference Series*. pp 62–71
- Ferraro F. R., et al., 2009, *Nature*, 462, 1028
- Ferraro F. R., et al., 2012, *Nature*, 492, 393
- Ferraro F. R., Lanzoni B., Dalessandro E., 2020, *Rendiconti Lincei. Scienze Fisiche e Naturali*, 31, 19
- Forbes D. A., 2020, *Monthly Notices of the Royal Astronomical Society*, 493, 847
- Forbes D. A., Bridges T., 2010, *Monthly Notices of the Royal Astronomical Society*, 404, 1203
- Fragione G., Rasio F. A., 2023, *The Astrophysical Journal*, 951, 129
- Fragione G., et al., 2020, *The Astrophysical Journal*, 900, 16
- Frank M. J., Hilker M., Mieske S., Baumgardt H., Grebel E. K., Infante L., 2011, *Monthly Notices of the Royal Astronomical Society*, 414, L70
- Freeman K., Bland-Hawthorn J., 2002, *Annual Review of Astronomy and Astrophysics*, 40, 487
- Fregeau J. M., Gürkan M. A., Joshi K. J., Rasio F. A., 2003, *The Astrophysical Journal*, 593, 772
- Fregeau J. M., Cheung P., Portegies Zwart S. F., Rasio F. A., 2004, *Monthly Notices of the Royal Astronomical Society*, 352, 1
- Fregeau J. M., Ivanova N., Rasio F. A., 2009, *The Astrophysical Journal*, 707, 1533
- Gaia Collaboration et al., 2016, *Astronomy & Astrophysics*, 595, A1
- Gaia Collaboration et al., 2024, arXiv e-prints, p. arXiv:2404.10486

- Geller A. M., et al., 2017a, *The Astrophysical Journal*, 840, 66
- Geller A. M., Leiner E. M., Chatterjee S., Leigh N. W. C., Mathieu R. D., Sills A., 2017b, *The Astrophysical Journal*, 842, 1
- Genzel R., Ott T., Eckart A., Schödel R., Alexander T., 2005, in Brandner W., Kasper M. E., eds, *Science with Adaptive Optics*. p. 275, doi:10.1007/10828557_48
- Ghez A. M., Klein B. L., Morris M., Becklin E. E., 1998, *The Astrophysical Journal*, 509, 678
- Gieles M., Balbinot E., Yaaqib R. I. S. M., Hénault-Brunet V., Zocchi A., Peuten M., Jonker P. G., 2018a, *Monthly Notices of the Royal Astronomical Society*, 473, 4832
- Gieles M., et al., 2018b, *Monthly Notices of the Royal Astronomical Society*, 478, 2461
- Giersz M., 1998, *Monthly Notices of the Royal Astronomical Society*, 298, 1239
- Giesers B. D., 2020, PhD thesis, Georg August University of Gottingen, Germany
- Giesers B., et al., 2018, *Monthly Notices of the Royal Astronomical Society*, 475, L15
- Giesers B., et al., 2019, *Astronomy & Astrophysics*, 632, A3
- Gnedin O. Y., Hernquist L., Ostriker J. P., 1999, *The Astrophysical Journal*, 514, 109
- Goodman J., Hut P., 1989, *Nature*, 339, 40
- Göttgens F., et al., 2019, *Astronomy & Astrophysics*, 631, A118
- Gunn J. E., Griffin R. F., 1979, *The Astronomical Journal*, 84, 752
- Häberle M., et al., 2021, *Monthly Notices of the Royal Astronomical Society*, 503, 1490
- Häberle M., et al., 2024, arXiv e-prints, p. arXiv:2405.06015
- Harris W. E., 1996, *The Astronomical Journal*, 112, 1487
- Harris J., Zaritsky D., 2009, *The Astronomical Journal*, 138, 1243
- Hartmann M., Debattista V. P., Seth A., Cappellari M., Quinn T. R., 2011, *Monthly Notices of the Royal Astronomical Society*, 418, 2697
- Heger A., Woosley S. E., 2002, *The Astrophysical Journal*, 567, 532
- Heggie D. C., 1975, *Monthly Notices of the Royal Astronomical Society*, 173, 729
- Herschel W., 1789, *Philosophical Transactions of the Royal Society of London*, 79, 151–153

- Hilker M., Infante L., Vieira G., Kissler-Patig M., Richtler T., 1999, *Astronomy and Astrophysics, Supplement*, 134, 75
- Holtzman J. A., et al., 1992, *The Astronomical Journal*, 103, 691
- Hong J., Vesperini E., Sollima A., McMillan S. L. W., D'Antona F., D'Ercole A., 2015, *Monthly Notices of the Royal Astronomical Society*, 449, 629
- Hong J., Patel S., Vesperini E., Webb J. J., Dalessandro E., 2019, *Monthly Notices of the Royal Astronomical Society*, 483, 2592
- Hopkins P. F., 2013, *Monthly Notices of the Royal Astronomical Society*, 428, 1950
- Horta D., Hughes M. E., Pfeffer J. L., Bastian N., Kruijssen J. M. D., Reina-Campos M., Crain R. A., 2021, *Monthly Notices of the Royal Astronomical Society*, 500, 4768
- Hurley J. R., Aarseth S. J., Shara M. M., 2007, *The Astrophysical Journal*, 665, 707
- Husser T. O., Wende-von Berg S., Dreizler S., Homeier D., Reiners A., Barman T., Hauschildt P. H., 2013, *Astronomy & Astrophysics*, 553, A6
- Husser T.-O., et al., 2016, *Astronomy & Astrophysics*, 588, A148
- Husser T.-O., et al., 2020, *Astronomy & Astrophysics*, 635, A114
- Hut P., McMillan S., Romani R. W., 1992, *The Astrophysical Journal*, 389, 527
- Hypki A., Giersz M., 2017, *Monthly Notices of the Royal Astronomical Society*, 466, 320
- Ivanova N., Belczynski K., Fregeau J. M., Rasio F. A., 2005, *Monthly Notices of the Royal Astronomical Society*, 358, 572
- Ivanova N., Heinke C. O., Rasio F. A., Taam R. E., Belczynski K., Fregeau J., 2006, *Monthly Notices of the Royal Astronomical Society*, 372, 1043
- Johnson C. I., Pilachowski C. A., 2010, *The Astrophysical Journal*, 722, 1373
- Johnson L. C., et al., 2015, *The Astrophysical Journal*, 802, 127
- Joshi K. J., 2000, PhD thesis, Massachusetts Institute of Technology
- Kamann S., Wisotzki L., Roth M. M., 2013, *Astronomy & Astrophysics*, 549, A71
- Kamann S., et al., 2016, *Astronomy & Astrophysics*, 588, A149
- Kamann S., et al., 2018, *Monthly Notices of the Royal Astronomical Society*, 473, 5591
- Kamann S., et al., 2020, *Astronomy & Astrophysics*, 635, A65

- Kipping D. M., 2013, *Monthly Notices of the Royal Astronomical Society*, 434, L51
- Kozai Y., 1962, *The Astronomical Journal*, 67, 591
- Kraft R. P., 1994, *Publications of the ASP*, 106, 553
- Krause M., Charbonnel C., Decressin T., Meynet G., Prantzos N., 2013, *Astronomy & Astrophysics*, 552, A121
- Kremer K., et al., 2020, *The Astrophysical Journal*, 903, 45
- Kruijssen J. M. D., 2014, *Classical and Quantum Gravity*, 31, 244006
- Kruijssen J. M. D., Pfeffer J. L., Reina-Campos M., Crain R. A., Bastian N., 2019, *Monthly Notices of the Royal Astronomical Society*, 486, 3180
- Kulkarni S. R., Hut P., McMillan S., 1993, *Nature*, 364, 421
- Lagioia E. P., Milone A. P., Marino A. F., Cordoni G., Tailo M., 2019, *The Astronomical Journal*, 158, 202
- Lamers H. J. G. L. M., Gieles M., 2006, *Astronomy & Astrophysics*, 455, L17
- Lamers H. J. G. L. M., Kruijssen J. M. D., Bastian N., Rejkuba M., Hilker M., Kissler-Patig M., 2017, *Astronomy & Astrophysics*, 606, A85
- Latour M., Hämmerich S., Dorsch M., Heber U., Husser T. O., Kamman S., Dreizler S., Brinchmann J., 2023, *Astronomy & Astrophysics*, 677, A86
- Lauer T. R., et al., 2005, *The Astronomical Journal*, 129, 2138
- Lee J.-W., 2017, *The Astrophysical Journal*, 844, 77
- Lee Y. W., Joo J. M., Sohn Y. J., Rey S. C., Lee H. C., Walker A. R., 1999, *Nature*, 402, 55
- Leigh N. W. C., Giersz M., Marks M., Webb J. J., Hypki A., Heinke C. O., Kroupa P., Sills A., 2015, *Monthly Notices of the Royal Astronomical Society*, 446, 226
- Leiner E., Mathieu R. D., Geller A. M., 2017, *The Astrophysical Journal*, 840, 67
- Leitinger E., Baumgardt H., Cabrera-Ziri I., Hilker M., Pancino E., 2023, *Monthly Notices of the Royal Astronomical Society*, 520, 1456
- Leonard P. J. T., 1989, *The Astronomical Journal*, 98, 217
- Lidov M. L., 1962, *Planetary Space Science*, 9, 719
- Loose H. H., Kruegel E., Tutukov A., 1982, *Astronomy & Astrophysics*, 105, 342

- Lovis C., Fischer D., 2010, in Seager S., ed., , Exoplanets. pp 27–53
- Lucatello S., Sollima A., Gratton R., Vesperini E., D’Orazi V., Carretta E., Bragaglia A., 2015, *Astronomy & Astrophysics*, 584, A52
- Lynn W. T., 1886, *The Observatory*. Editors of the Observatory
- Maccarone T. J., Kundu A., Zepf S. E., Rhode K. L., 2007, *Nature*, 445, 183
- Mapelli M., 2018, arXiv e-prints, p. arXiv:1809.09130
- Mapelli M., et al., 2021, *Monthly Notices of the Royal Astronomical Society*, 505, 339
- Marino A. F., et al., 2015, *Monthly Notices of the Royal Astronomical Society*, 450, 815
- Martell S. L., Smolinski J. P., Beers T. C., Grebel E. K., 2011, *Astronomy & Astrophysics*, 534, A136
- Massari D., Koppelman H. H., Helmi A., 2019a, *Astronomy & Astrophysics*, 630, L4
- Massari D., Koppelman H. H., Helmi A., 2019b, *Astronomy & Astrophysics*, 630, L4
- Mateo M., Harris H. C., Nemeč J., Olszewski E. W., 1990, *The Astronomical Journal*, 100, 469
- McCrea W. H., 1964, *Monthly Notices of the Royal Astronomical Society*, 128, 147
- McMillan S. L. W., Pryor C., Phinney E. S., 1998a, *Highlights of Astronomy*, 11A, 616
- McMillan S. L. W., Pryor C., Phinney E. S., 1998b, *Highlights of Astronomy*, 11A, 616
- Mihos J. C., Hernquist L., 1994, *Astrophysical Journal, Letters*, 437, L47
- Miller-Jones J. C. A., et al., 2015, *Monthly Notices of the Royal Astronomical Society*, 453, 3918
- Milone A. P., Marino A. F., 2022, *Universe*, 8, 359
- Milone A. P., Piotto G., Bedin L. R., Cassisi S., Anderson J., Marino A. F., Pietrinferni A., Aparicio A., 2012a, *Astronomy & Astrophysics*, 537, A77
- Milone A. P., et al., 2012b, *Astronomy & Astrophysics*, 540, A16
- Milone A. P., et al., 2012c, *The Astrophysical Journal*, 744, 58
- Milone A. P., et al., 2012d, *Astrophysical Journal, Letters*, 754, L34
- Milone A. P., et al., 2014, *Monthly Notices of the Royal Astronomical Society*, 439, 1588
- Milone A. P., et al., 2017, *Monthly Notices of the Royal Astronomical Society*, 464, 3636

- Milone A. P., et al., 2019, *Monthly Notices of the Royal Astronomical Society*, 484, 4046
- Milone A. P., et al., 2020, *Monthly Notices of the Royal Astronomical Society*, 497, 3846
- Milosavljević M., 2004, *Astrophysical Journal, Letters*, 605, L13
- Milosavljević M., Merritt D., 2001, *The Astrophysical Journal*, 563, 34
- Minniti D., et al., 2015, *Astrophysical Journal, Letters*, 810, L20
- Moe M., Di Stefano R., 2017, *Astrophysical Journal, Supplement*, 230, 15
- Moehler S., Sweigart A. V., Landsman W. B., Dreizler S., 2002, *Astronomy & Astrophysics*, 395, 37
- Mohandas A., et al., 2024, *Astronomy & Astrophysics*, 681, A42
- Morscher M., Pattabiraman B., Rodriguez C., Rasio F. A., Umbreit S., 2015, *The Astrophysical Journal*, 800, 9
- Mucciarelli A., Origlia L., Ferraro F. R., Pancino E., 2009, *Astrophysical Journal, Letters*, 695, L134
- Naoz S., 2016, *Annual Review of Astronomy and Astrophysics*, 54, 441
- Neumayer N., Seth A., Böker T., 2020, *The Astronomy and Astrophysics Review*, 28, 4
- Nguyen D. D., et al., 2018, *The Astrophysical Journal*, 858, 118
- Nitschai M. S., et al., 2023, arXiv e-prints, p. arXiv:2309.02503
- Noyola E., Gebhardt K., 2006, *The Astronomical Journal*, 132, 447
- Noyola E., Gebhardt K., Bergmann M., 2008, *The Astrophysical Journal*, 676, 1008
- Noyola E., Gebhardt K., Kissler-Patig M., Lützgendorf N., Jalali B., de Zeeuw P. T., Baumgardt H., 2010, *Astrophysical Journal, Letters*, 719, L60
- Offner S. S. R., Moe M., Kratter K. M., Sadavoy S. I., Jensen E. L. N., Tobin J. J., 2023, in Inutsuka S., Aikawa Y., Muto T., Tomida K., Tamura M., eds, *Astronomical Society of the Pacific Conference Series Vol. 534, Protostars and Planets VII*. p. 275 (arXiv:2203.10066), doi:10.48550/arXiv.2203.10066
- Ordenes-Briceño Y., et al., 2018, *The Astrophysical Journal*, 860, 4
- Padoan P., Jimenez R., Jones B., 1997, *Monthly Notices of the Royal Astronomical Society*, 285, 711

- Pancino E., Ferraro F. R., Bellazzini M., Piotto G., Zoccali M., 2000, *Astrophysical Journal, Letters*, 534, L83
- Pechetti R., et al., 2024, *Monthly Notices of the Royal Astronomical Society*, 528, 4941
- Peebles P. J. E., Dicke R. H., 1968, *The Astrophysical Journal*, 154, 891
- Pfeffer J., Baumgardt H., 2013, *Monthly Notices of the Royal Astronomical Society*, 433, 1997
- Pfeffer J., Kruijssen J. M. D., Crain R. A., Bastian N., 2018, *Monthly Notices of the Royal Astronomical Society*, 475, 4309
- Pfeffer J., Lardo C., Bastian N., Saracino S., Kamann S., 2021, *Monthly Notices of the Royal Astronomical Society*, 500, 2514
- Platais I., et al., 2024, *The Astrophysical Journal*, 963, 60
- Prantzos N., Charbonnel C., 2006, *Astronomy & Astrophysics*, 458, 135
- Price-Whelan A. M., Hogg D. W., Foreman-Mackey D., Rix H.-W., 2017, *The Astrophysical Journal*, 837, 20
- Pryor C. P., Latham D. W., Hazen M. L., 1988, *The Astronomical Journal*, 96, 123
- Quinlan G. D., Hernquist L., 1997, *New Astronomy*, 2, 533
- Ramírez I., Meléndez J., Chanamé J., 2012, *The Astrophysical Journal*, 757, 164
- Reina-Campos M., Kruijssen J. M. D., Pfeffer J., Bastian N., Crain R. A., 2018, *Monthly Notices of the Royal Astronomical Society*, 481, 2851
- Renaud F., Gieles M., 2013, *Monthly Notices of the Royal Astronomical Society*, 431, L83
- Renzini A., 2013, *Mem. Societa Astronomica Italiana*, 84, 162
- Rich R. M., Ryde N., Thorsbro B., Fritz T. K., Schultheis M., Origlia L., Jönsson H., 2017, *The Astronomical Journal*, 154, 239
- Richard J., et al., 2019, arXiv e-prints, p. arXiv:1906.01657
- Rieder S., Ishiyama T., Langelan P., Makino J., McMillan S. L. W., Portegies Zwart S., 2013, *Monthly Notices of the Royal Astronomical Society*, 436, 3695
- Ritchie B. W., Clark J. S., Negueruela I., Najarro F., 2022, *Astronomy & Astrophysics*, 660, A89

- Rodriguez C. L., Chatterjee S., Rasio F. A., 2016, *Physical Review D*, 93, 084029
- Salinas R., Jílková L., Carraro G., Catelan M., Amigo P., 2012, *Monthly Notices of the Royal Astronomical Society*, 421, 960
- Sana H., et al., 2013, *Astronomy & Astrophysics*, 550, A107
- Sánchez-Janssen R., et al., 2019, *The Astrophysical Journal*, 878, 18
- Sandage A. R., 1953, *The Astronomical Journal*, 58, 61
- Saracino S., et al., 2016, *The Astrophysical Journal*, 832, 48
- Saracino S., et al., 2022, *Monthly Notices of the Royal Astronomical Society*, 511, 2914
- Saracino S., et al., 2023, *Monthly Notices of the Royal Astronomical Society*, 526, 299
- Sarajedini A., et al., 2007, *The Astronomical Journal*, 133, 1658
- Schödel R., et al., 2002, *Nature*, 419, 694
- Searle L., Zinn R., 1978, *The Astrophysics Journal*, 225, 357
- Seth A. C., et al., 2014, *Nature*, 513, 398
- Sigurdsson S., Hernquist L., 1993, *Nature*, 364, 423
- Sollima A., Baumgardt H., 2017, *Monthly Notices of the Royal Astronomical Society*, 471, 3668
- Sollima A., Beccari G., Ferraro F. R., Fusi Pecci F., Sarajedini A., 2007, *Monthly Notices of the Royal Astronomical Society*, 380, 781
- Sollima A., Lanzoni B., Beccari G., Ferraro F. R., Fusi Pecci F., 2008, *Astronomy & Astrophysics*, 481, 701
- Sollima A., Baumgardt H., Hilker M., 2019, *Monthly Notices of the Royal Astronomical Society*, 485, 1460
- Sommariva V., Piotto G., Rejkuba M., Bedin L., Heggie D. C., Mathieu R. D., Villanova S., 2009, *Astronomy & Astrophysics*, 493, 947
- Song Y.-Y., Mateo M., Bailey J. I., Walker M. G., Roederer I. U., Olszewski E. W., Reiter M., Kremin A., 2021, *Monthly Notices of the Royal Astronomical Society*, 504, 4160
- Spitzer Lyman J., 1969, *Astrophysical Journal, Letters*, 158, L139
- Spitzer L., 1987, *Dynamical evolution of globular clusters*

- Stevenson S., Sampson M., Powell J., Vigna-Gómez A., Neijssel C. J., Szécsi D., Mandel I., 2019, *The Astrophysical Journal*, 882, 121
- Strader J., Chomiuk L., Maccarone T. J., Miller-Jones J. C. A., Seth A. C., 2012, *Nature*, 490, 71
- Stryker L. L., 1993, *Publications of the ASP*, 105, 1081
- Tauris T. M., van den Heuvel E. P. J., 2006, in , Vol. 39, Compact stellar X-ray sources. pp 623–665, doi:10.48550/arXiv.astro-ph/0303456
- Tecza M., Thatte N., Clarke F., Freeman D., 2009, in *Science with the VLT in the ELT Era*. p. 267, doi:10.1007/978-1-4020-9190-2_45
- Tremaine S. D., Ostriker J. P., Spitzer L. J., 1975, *The Astrophysical Journal*, 196, 407
- Trenti M., Padoan P., Jimenez R., 2015, *Astrophysical Journal, Letters*, 808, L35
- Valcarce A. A. R., Catelan M., 2011, *Astronomy & Astrophysics*, 533, A120
- Ventura P., D’Antona F., Mazzitelli I., Gratton R., 2001, *Astrophysical Journal, Letters*, 550, L65
- Vesperini E., McMillan S. L. W., D’Antona F., D’Ercole A., 2011, *Monthly Notices of the Royal Astronomical Society*, 416, 355
- Vesperini E., McMillan S. L. W., D’Antona F., D’Ercole A., 2013, *Monthly Notices of the Royal Astronomical Society*, 429, 1913
- Villanova S., Carraro G., Saviane I., 2009, *Astronomy & Astrophysics*, 504, 845
- Volonteri M., 2012, *Science*, 337, 544
- Watkins L. L., van der Marel R. P., Libralato M., Bellini A., Anderson J., Alfaro-Cuello M., 2022, *The Astrophysical Journal*, 936, 154
- Weatherford N. C., Chatterjee S., Kremer K., Rasio F. A., 2020, *The Astrophysical Journal*, 898, 162
- Weilbacher P. M., et al., 2020, *Astronomy & Astrophysics*, 641, A28
- Williams I. P., 1964, *Annales d’Astrophysique*, 27, 198
- Woitak J., Leinert C., Köhler R., 2001, *Astronomy & Astrophysics*, 376, 982
- Zocchi A., Gieles M., Hénault-Brunet V., 2019, *Monthly Notices of the Royal Astronomical Society*, 482, 4713

-
- de Mink S. E., Pols O. R., Langer N., Izzard R. G., 2009, *Astronomy & Astrophysics*, 507, L1
- den Brok M., et al., 2014, *Monthly Notices of the Royal Astronomical Society*, 445, 2385
- van de Ven G., van den Bosch R. C. E., Verolme E. K., de Zeeuw P. T., 2006, *Astronomy & Astrophysics*, 445, 513
- van den Heuvel E. P. J., 1967, *The Observatory*, 87, 68
- van der Marel R. P., Anderson J., 2010a, *The Astrophysical Journal*, 710, 1063
- van der Marel R. P., Anderson J., 2010b, *The Astrophysical Journal*, 710, 1063